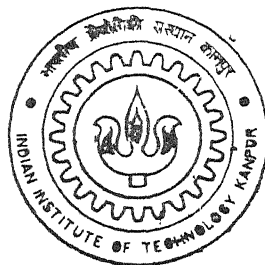


90703 0 7

# MODELING OF TRANSPORT PHENOMENA IN A LOW PRESSURE CVD REACTOR

By

Arnab Kumar De



DEPARTMENT OF MECHANICAL ENGINEERING

Indian Institute of Technology Kanpur

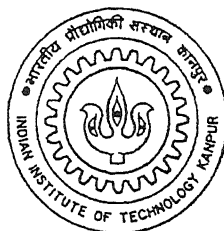
APRIL, 2002

# MODELING OF TRANSPORT PHENOMENA IN A LOW PRESSURE CVD REACTOR

A Thesis Submitted  
In Partial Fulfilment of the Requirements  
for the Degree of  
Master of Technology

by

Arnab Kumar De



to the  
DEPARTMENT OF MECHANICAL ENGINEERING  
INDIAN INSTITUTE OF TECHNOLOGY KANPUR  
INDIA

April, 2002

5 FEB 2003 | ME

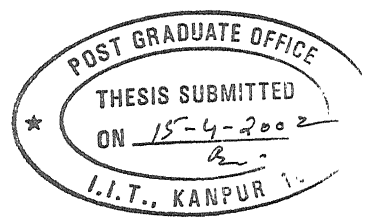
पुस्तकालय कानपुर

संस्थान कानपुर

अवधि क्र० A...141937



A141937



## CERTIFICATE

It is certified that the work contained in the thesis entitled “*Modeling of Transport Phenomena in a low pressure CVD reactor.*”, by *Mr. Arnab Kumar De*, has been carried out under our supervision and that this work has not been submitted elsewhere for a degree.

Dr. V. Eswaran  
Dept. of Mechanical Engineering  
I.I.T. Kanpur 208016

Dr. K. Muralidhar  
Dept. of Mechanical Engineering  
I.I.T Kanpur 208016

April, 2002



# Abstract

Chemical vapour deposition (CVD) reactors are used for growing thin films of special materials on suitable substrates. A particular reactor at Centre for Advanced Technology, Indore is in the development stages to manufacture dome-shaped infrared sensors for night vision applications in the defence industry. The computational study of transport phenomena in such a reactor has been accomplished in the present work. The reactor has a central jet carrying hydrogen sulphide and peripheral jets carrying zinc that react in the core to form zinc sulphide as a deposit on the solid surfaces. The reactants are transported by argon that acts as an inert carrier gas. The primary deposition surface is a transversely placed block within the reactor tube. A two-dimensional model has been developed to study flow and mass transfer phenomena within the reactor. Three geometric configurations of the reactor have been studied and two new geometries have been proposed with the aim of providing alternatives to the proposed CVD technology.

The mathematical model comprises of the system of conservation of mass, momentum and the species transport equations. The spatial temperature variation in the reaction zone is expected to be small and has been neglected. The gas phase reaction of zinc and hydrogen sulphide is taken to occur in a single step, besides being homogeneous and irreversible. The dilute solution approximation has been uniformly adopted in the present work. Higher order phenomena such as the thermo-diffusion and dufour effect have not been considered.

The momentum equations have been solved by finite volume method (FVM). The dependent variables have been arranged on a collocated grid. Momentum interpolation has been used to resolve the difficulty of decoupling velocity and pressure. For the average pressure and temperature encountered in the reactor, Reynolds numbers are in the range of 10-100. Hence, laminar incompressible con-

ditions are realized in the flow field. The mass transfer equations have been solved by the application of the operator splitting algorithm. The source term that models chemical reactions in the species transport equation has been linearized with respect to the species concentration. This permits a partial analytical solution to the governing equations and improves the computational efficiency. The deposition surfaces have been modelled to be passive. It was seen that arriving at a correct boundary conditions for a passive surface was difficult and led to errors in the deposition rate profiles. This situation has mitigated by employing a Dirichlet condition on the substrate that slightly overestimates the deposition rate.

The following results have been obtained in the present work. The species concentration field correlates closely with the flow field in the reactor. Over the range of Reynolds numbers studied, the flow pattern reveals a recirculation zone adjacent to the side walls and a stagnation zone ahead of the block. Species mixing predominantly occurs in the zone closer to the reactor axis and the products are carried away by the stream bypassing the block. Under favourable conditions, a considerable amount of deposition can occur over the block surface. The performance of the reactor designs proposed at Centre for Advanced Technology, Indore are not satisfactory in terms of deposition rate and its uniformity. The two new geometries explored in the present work not only improve the deposition rate by a factor of two ( $1.027 \mu\text{m}/\text{min}$  from  $0.542 \mu\text{m}/\text{min}$ ) but also retain the uniformity in the thickness of the layer formed. The new geometries have the potential to significantly reduce overall cost and time (from over a year to just a few months) for thin film deposition.

# Acknowledgement

I express my sincere gratitude to my supervisors Professor K. Muralidhar and Professor V. Eswaran for their valuable guidance, timely suggestions and co-operation during the present work. Their interest, confidence and vision have helped to reach a successful completion of the present work. I am also thankful to Rakesh, Abir, Kamlesh, Amit, Vivek, Arvind for providing a friendly ambiance in the laboratory. I thank Mr. A. sharma, Mr. J. Banerjee, Mr. S. Panjabi and Mr. A. Tariq for their occasional helps and suggestions. I would like to make a special mention about the excellent computational facility provided in the "Computational Modeling Laboratory".

Arnab Kumar de

# Contents

Certificate	i
Abstract	i
Acknowledgements	i
List of Figures	i
Nomenclature	i
<b>1 Introduction</b>	<b>1</b>
1.1 Literature Survey . . . . .	4
1.2 Statement of the problem . . . . .	6
1.3 Thesis Organization . . . . .	8
1.4 Objectives of the present work . . . . .	9
<b>2 Mathematical Formulation</b>	<b>10</b>
2.1 Equations Governing Flow, Heat and Mass Transfer . . . . .	10
2.1.1 Continuity equation . . . . .	10
2.1.2 Momentum Equations . . . . .	11
2.1.3 Energy Equation . . . . .	12
2.1.4 Species transport Equation . . . . .	13
2.2 Nondimensionalization of the governing equations . . . . .	20

2.3	Initial and boundary conditions . . . . .	22
2.3.1	Initial condition . . . . .	23
2.3.2	Boundary conditions . . . . .	23
2.4	Range of parameters . . . . .	25
2.5	Shear stress on the solid surfaces . . . . .	27
<b>3</b>	<b>Numerical Solution</b>	<b>28</b>
3.1	Orthogonal Grid Generation . . . . .	28
3.1.1	Elliptic Grid Generation . . . . .	29
3.1.2	Orthogonal grid generation . . . . .	30
3.1.3	Numerical solution . . . . .	31
3.2	Solution of the Mass and Momentum equations . . . . .	33
3.2.1	Governing equations in integral form . . . . .	34
3.2.2	Description of the finite volume method . . . . .	34
3.2.3	Discretization Procedure . . . . .	41
3.2.4	Time integration Scheme . . . . .	49
3.2.5	Calculation of the time step . . . . .	58
3.2.6	Initial and Boundary conditions . . . . .	60
3.3	Solution of species transport equations . . . . .	63
3.3.1	Source term linearization . . . . .	64
3.3.2	Operator Splitting algorithm . . . . .	66
3.3.3	Initial and Boundary conditions . . . . .	69
3.4	Grid Independence Test . . . . .	70
<b>4</b>	<b>Results and Discussion</b>	<b>76</b>
4.1	Flow and concentration fields . . . . .	76
4.1.1	Reactor with a flat substrate . . . . .	76
4.1.2	Reactor with a concave substrate . . . . .	90
4.2	Wall shear stress and deposition rate of zinc sulphide . . . . .	103

4.2.1	Properties of a flat substrate . . . . .	103
4.2.2	Properties of a concave substrate . . . . .	109
4.3	Evaluation of alternative geometries . . . . .	114
4.3.1	Flow and concentration fields with a convex substrate . . .	114
4.3.2	Flow and concentration fields with coaxial jets . . . . .	120
4.3.3	Wall shear stress and Deposition rate Profiles for a convex substrate . . . . .	125
4.3.4	Wall shear stress and Deposition rate Profiles for coaxial jets	126
<b>5</b>	<b>Conclusions and Scope for Future Work</b>	<b>130</b>
5.1	Conclusions . . . . .	130
5.2	Scope for future work . . . . .	131
<b>Appendices</b>		
<b>A</b>	<b>Evaluation of species properties</b>	<b>132</b>
A.1	Binary diffusion coefficients . . . . .	132
A.2	Kinematic viscosity . . . . .	133
<b>B</b>	<b>Validation of Fluid Flow and Mass transfer Codes</b>	<b>134</b>
B.1	Fluid Flow . . . . .	134
B.2	Mass Transfer . . . . .	136
<b>C</b>	<b>Derivation of Orthogonal grid generation equation</b>	<b>138</b>
C.1	Definition . . . . .	138
C.2	Elliptic generation system . . . . .	140
C.3	Orthogonal generation system . . . . .	141
<b>References</b>		<b>144</b>

# List of Figures

1.1	The CVD reactor proposed to be used in CAT, Indore . . . . .	2
1.2	Schematic representation of the sequential processes occur in CVD reactors. . . . .	3
1.3	Two views of the CVD reactor . . . . .	6
1.4	The axisymmetric two-dimensional reactor geometry employed in the present study with a flat (a) and a curved (b) deposition surface	7
1.5	The axisymmetric two-dimensional reactor geometry employed in the present study with a convex deposition surface and jets separated by a distance (a) concave deposition surface and coaxial jets (b) . . . . .	7
3.1	A typical finite volume employed in the computation. . . . .	35
3.2	A typical finite volume cell (shaded) and its neighbours in the $x-y$ and $y-z$ planes. . . . .	36
3.3	Grids used in the calculations for the reactor with plane substrate; (a) $73 \times 38$ , (b) $83 \times 48$ , (c) $103 \times 68$ . . . . .	38
3.4	Partially converged grids used in the calculations for the reactor with curved substrate; (a) $73 \times 38$ , (b) $83 \times 48$ , (c) $103 \times 68$ . . .	39
3.5	Fully converged grids for the reactor with curved substrate; (a) $73 \times 38$ , (b) $83 \times 48$ , (c) $103 \times 68$ . . . . .	40

3.6	Lengths required for the calculation of diffusion fluxes and related nomenclature. . . . .	48
3.7	One of the corner cells (shaded) and associated velocities. . . . .	61
3.8	Velocities associated with the free-slip boundary condition in the azimuthal direction. . . . .	62
3.9	Nondimensional shear stress distribution on the reactor wall for the geometry with flat substrate. . . . .	70
3.10	Nondimensional shear stress distribution on the reactor wall for a curved substrate. . . . .	71
3.11	Nondimensional shear stress distribution on the substrate surface for a flat substrate. . . . .	71
3.12	Nondimensional shear stress distribution on the reactor wall for a curved substrate. . . . .	72
3.13	Radial variation of deposition rate on the solid surface for a flat substrate. . . . .	73
3.14	Velocity vectors for the reactor with a flat substrate, (a) $73 \times 38$ , (b) $83 \times 48$ , (c) $103 \times 68$ ; Configuration $Re = 100$ , $V_r = 5$ , $r_b = 0.8$ , $Z_b = 1$ , $\alpha = 30^\circ$ . . . . .	74
3.15	steady state contours of consumption rate of Zn (a) $73 \times 38$ , (c) $83 \times 48$ , (e) $103 \times 68$ ; steady state contours of ZnS mass fractions (b) $73 \times 38$ , (d) $83 \times 48$ , (f) $103 \times 68$ ; configuration: $Re=100$ , $V_r = 5$ , $r_b = 0.8$ , $\alpha = 30^\circ$ , $Z_b = 1$ . . . . .	75
4.1	Velocity vectors (a), steady state contours of consumption rate of Zn (b), steady state contours of production rate of ZnS (c), contours of mass fraction of Zn (d), contours of mass fraction of ZnS (e), Baseline configuration: $Re=100$ , $V_r = 2$ , $r_b = 0.8$ , $\alpha = 0$ , $Z_b = 1$ . . . . .	80



4.2	Velocity vectors (a), steady state contours of consumption rate of Zn (b), steady state contours of production rate of ZnS (c), contours of mass fraction of Zn (d), contours of mass fraction of ZnS (e), $Re=100$ , $V_r = 2$ , $r_b = 0.8$ , $\alpha = 30^\circ$ inwards, $Z_b = 1$ . . . .	81
4.3	Velocity vectors (a), steady state contours of consumption rate of Zn (b), steady state contours of production rate of ZnS (c), contours of mass fraction of Zn (d), contours of mass fraction of ZnS (e), $Re=100$ , $V_r = 2$ , $r_b = 0.8$ , $\alpha = 0$ , $Z_b = 0.6$ . . . . .	82
4.4	Velocity vectors (a), steady state contours of consumption rate of Zn (b), steady state contours of production rate of ZnS (c), contours of mass fraction of Zn (d), contours of mass fraction of ZnS (e), $Re=100$ , $V_r = 2$ , $r_b = 0.8$ , $\alpha = 30^\circ$ inwards, $Z_b = 0.6$ . . .	83
4.5	Velocity vectors (a), steady state contours of consumption rate of Zn (b), steady state contours of production rate of ZnS (c), contours of mass fraction of Zn (d), contours of mass fraction of ZnS (e), $Re=100$ , $V_r = 2$ , $r_b = 0.9$ , $\alpha = 0$ , $Z_b = 1$ . . . . .	84
4.6	Velocity vectors (a), steady state contours of consumption rate of Zn (b), steady state contours of production rate of ZnS (c), contours of mass fraction of Zn (d), contours of mass fraction of ZnS (e), $Re=100$ , $V_r = 2$ , $r_b = 0.9$ , $\alpha = 30^\circ$ inwards, $Z_b = 1$ . . . .	85
4.7	Velocity vectors (a), steady state contours of consumption rate of Zn (b), steady state contours of production rate of ZnS (c), contours of mass fraction of Zn (d), contours of mass fraction of ZnS (e), $Re=100$ , $V_r = 5$ , $r_b = 0.8$ , $\alpha = 0$ , $Z_b = 1$ . . . . .	86
4.8	Velocity vectors (a), steady state contours of consumption rate of Zn (b), steady state contours of production rate of ZnS (c), contours of mass fraction of Zn (d), contours of mass fraction of ZnS (e), $Re=100$ , $V_r = 5$ , $r_b = 0.8$ , $\alpha = 30^\circ$ inwards, $Z_b = 1$ . . . .	87

4.9	Velocity vectors (a), steady state contours of consumption rate of Zn (b), steady state contours of production rate of ZnS (c), contours of mass fraction of Zn (d), contours of mass fraction of ZnS (e), $Re=10$ , $V_r = 2$ , $r_b = 0.8$ , $\alpha = 0$ , $Z_b = 1$ . . . . .	88
4.10	Velocity vectors (a), steady state contours of consumption rate of Zn (b), steady state contours of production rate of ZnS (c), contours of mass fraction of Zn (d), contours of mass fraction of ZnS (e), $Re=10$ , $V_r = 2$ , $r_b = 0.8$ , $\alpha = 30^\circ$ inwards, $Z_b = 1$ . . . .	89
4.11	Velocity vectors (a), steady state contours of consumption rate of Zn (b), steady state contours of production rate of ZnS (c), contours of mass fraction of Zn (d), contours of mass fraction of ZnS (e), Baseline configuration: $Re=100$ , $V_r = 2$ , $r_b = 0.8$ , $\alpha = 0$ , $Z_b = 1$ . . . . .	93
4.12	Velocity vectors (a), steady state contours of consumption rate of Zn (b), steady state contours of production rate of ZnS (c), contours of mass fraction of Zn (d), contours of mass fraction of ZnS (e), $Re=100$ , $V_r = 2$ , $r_b = 0.8$ , $\alpha = 30^\circ$ inwards, $Z_b = 1$ . . . .	94
4.13	Velocity vectors (a), steady state contours of consumption rate of Zn (b), steady state contours of production rate of ZnS (c), contours of mass fraction of Zn (d), contours of mass fraction of ZnS (e), $Re=100$ , $V_r = 2$ , $r_b = 0.8$ , $\alpha = 0$ , $Z_b = 0.6$ . . . . .	95
4.14	Velocity vectors (a), steady state contours of consumption rate of Zn (b), steady state contours of production rate of ZnS (c), contours of mass fraction of Zn (d), contours of mass fraction of ZnS (e), $Re=100$ , $V_r = 2$ , $r_b = 0.8$ , $\alpha = 30^\circ$ inwards, $Z_b = 0.6$ . . . .	96
4.15	Velocity vectors (a), steady state contours of consumption rate of Zn (b), steady state contours of production rate of ZnS (c), contours of mass fraction of Zn (d), contours of mass fraction of ZnS (e), $Re=100$ , $V_r = 2$ , $r_b = 0.9$ , $\alpha = 0$ , $Z_b = 1$ . . . . .	97

4.16	Velocity vectors (a), steady state contours of consumption rate of Zn (b), steady state contours of production rate of ZnS (c), contours of mass fraction of Zn (d), contours of mass fraction of ZnS (e), $Re=100$ , $V_r = 2$ , $r_b = 0.9$ , $\alpha = 30^\circ$ inwards, $Z_b = 1$ . . . .	98
4.17	Velocity vectors (a), steady state contours of consumption rate of Zn (b), steady state contours of production rate of ZnS (c), contours of mass fraction of Zn (d), contours of mass fraction of ZnS (e), $Re=100$ , $V_r = 5$ , $r_b = 0.8$ , $\alpha = 0$ , $Z_b = 1$ . . . . .	99
4.18	Velocity vectors (a), steady state contours of consumption rate of Zn (b), steady state contours of production rate of ZnS (c), contours of mass fraction of Zn (d), contours of mass fraction of ZnS (e), $Re=100$ , $V_r = 5$ , $r_b = 0.8$ , $\alpha = 30^\circ$ inwards, $Z_b = 1$ . . . .	100
4.19	Velocity vectors (a), steady state contours of consumption rate of Zn (b), steady state contours of production rate of ZnS (c), contours of mass fraction of Zn (d), contours of mass fraction of ZnS (e), $Re=10$ , $V_r = 2$ , $r_b = 0.8$ , $\alpha = 0$ , $Z_b = 1$ . . . . .	101
4.20	Velocity vectors (a), steady state contours of consumption rate of Zn (b), steady state contours of production rate of ZnS (c), contours of mass fraction of Zn (d), contours of mass fraction of ZnS (e), $Re=10$ , $V_r = 2$ , $r_b = 0.8$ , $\alpha = 30^\circ$ inwards, $Z_b = 1$ . . . .	102
4.21	Axial variation of the skin friction coefficient on the wall of the reactor tube for the flat substrate geometry; $\alpha = 0$ (a), $\alpha = 30^\circ$ (b).	106
4.22	Effect of Reynolds number on the skin friction coefficient and the deposition rate on the substrate surface, $r_b = 0.8$ , $V_r = 2$ , $Z_b = 1$ . .	107
4.23	Effect of the position of the substrate on the skin friction coefficient and the deposition rate on the substrate surface, $Re=100$ , $r_b = 0.8$ , $V_r = 2$ . . . . .	107
4.24	Effect of the diameter of the substrate on the skin friction coefficient and the deposition rate on the substrate surface, $Re=100$ , $V_r = 2$ , $Z_b = 1$ . . . . .	108

4.25	Effect of the central-to-peripheral jet velocity ratio on the skin friction coefficient and the deposition rate on the substrate surface, $Re=100$ , $r_b = 0.8$ , $Z_b = 1$ . . . . .	108
4.26	Axial variation of skin friction coefficient on the reactor wall for the concave substrate geometry; $\alpha = 0$ (a), $\alpha = 30^\circ$ (b). . . . .	111
4.27	Effect of Reynolds number on the skin friction coefficient and the deposition rate on the substrate surface, $r_b = 0.8$ , $V_r = 2$ , $Z_b = 1$ . .	112
4.28	Effect of the position of the substrate on the skin friction coefficient and the deposition rate on the substrate surface, $Re=100$ , $r_b = 0.8$ , $V_r = 2$ . . . . .	112
4.29	Effect of the diameter of the substrate on the skin friction coefficient and the deposition rate on the substrate surface, $Re=100$ , $V_r = 2$ , $Z_b = 1$ . . . . .	113
4.30	Effect of the central-to-peripheral jet velocity ratio on the skin friction coefficient and the deposition rate on the substrate surface, $Re=100$ , $r_b = 0.8$ , $Z_b = 1$ . . . . .	113
4.31	Velocity vectors (a), steady state contours of consumption rate of Zn (b), steady state contours of production rate of ZnS (c), contours of mass fraction of Zn (d), contours of mass fraction of ZnS (e), Baseline configuration: $Re=100$ , $V_r = 2$ , $r_b = 0.8$ , $\alpha = 30^\circ$ inwards, $Z_b = 1$ . . . . .	117
4.32	Velocity vectors (a), steady state contours of consumption rate of Zn (b), steady state contours of production rate of ZnS (c), contours of mass fraction of Zn (d), contours of mass fraction of ZnS (e), $Re=100$ , $V_r = 2$ , $r_b = 0.8$ , $\alpha = 30^\circ$ inwards, $Z_b = 0.6$ . . .	118
4.33	Velocity vectors (a), steady state contours of consumption rate of Zn (b), steady state contours of production rate of ZnS (c), contours of mass fraction of Zn (d), contours of mass fraction of ZnS (e), $Re=100$ , $V_r = 1$ , $r_b = 0.8$ , $\alpha = 30^\circ$ inwards, $Z_b = 1$ . . . .	119

4.34	Velocity vectors (a), steady state contours of consumption rate of Zn (b), steady state contours of production rate of ZnS (c), contours of mass fraction of Zn (d), contours of mass fraction of ZnS (e), Baseline configuration: $Re=100$ , $V_r = 2$ , $r_b = 0.8$ , $\alpha = 0$ , $Z_b = 1$ . . . . .	122
4.35	Velocity vectors (a), steady state contours of consumption rate of Zn (b), steady state contours of production rate of ZnS (c), contours of mass fraction of Zn (d), contours of mass fraction of ZnS (e), $Re=100$ , $V_r = 2$ , $r_b = 0.8$ , $\alpha = 0$ , $Z_b = 0.6$ . . . . .	123
4.36	Velocity vectors (a), steady state contours of consumption rate of Zn (b), steady state contours of production rate of ZnS (c), contours of mass fraction of Zn (d), contours of mass fraction of ZnS (e), $Re=100$ , $V_r = 1$ , $r_b = 0.8$ , $\alpha = 0$ , $Z_b = 1$ . . . . .	124
4.37	Axial variation of skin friction coefficient on the reactor tube wall for the convex substrate geometry; $\alpha = 30^\circ$ . . . . .	128
4.38	Axial variation of skin friction coefficient on the reactor tube wall for the coaxial jets configuration; $\alpha = 0$ . . . . .	128
4.39	Skin friction coefficient and the deposition rate on the substrate surface for the convex substrate geometry with $Re=100$ , $\alpha = 30^\circ$ and $r_b = 0.8$ ; (a) $V_r = 1$ , $Z_b = 1$ ; (b) $V_r = 2$ , $Z_b = 0.6$ ; (c) $V_r = 2$ , $Z_b = 1$ . . . . .	129
4.40	Skin friction coefficient and the deposition rate on the substrate surface for the coaxial jets configuration with $Re=100$ , $\alpha = 0$ and $r_b = 0.8$ ; (a) $V_r = 1$ , $Z_b = 1$ ; (b) $V_r = 2$ , $Z_b = 0.6$ ; (c) $V_r = 2$ , $Z_b = 1$ . . . . .	129
B.1	(a) Inlet velocity profile with only half section of the pipe in shown, (b), (c) and (d) comparison of the computed axial velocity profile (full curve) with Sider and Churchill (1971) (shaded circle) at three axial locations . . . . .	135

B.2	Transient variation of species; hydrogen sulphide (a) point 1, (c) point 2, (e) point 3; zinc sulphide (b) point 1, (d) point 2, (f) point 3. . . . .	137
-----	---	-----

# Nomenclature

$C_f$	Skin friction coefficient
$D_{i,o}$	Binary diffusion coefficient of species $i$ in argon at the inlet temperature $\text{m}^2/\text{s}$
$D_{i,j}$	Diffusion coefficient of species $i$ in $j$ $\text{m}^2/\text{s}$
$D_i$	Binary diffusion coefficient of species $i$ in argon $\text{m}^2/\text{s}$
$d$	Diameter of the reactor
$M_i$	Molecular weight of $i$ th species
$M_c$	Molecular weight of argon
$P_{em}$	Peclet number associated with mass transfer
$Re$	Reynolds number
$r_b$	Dimensionless radius of the substrate
$k_f$	Forward rate of constant $\text{m}^3/\text{mol-s}$
$k_r$	Backward rate of constant $\text{m}^3/\text{mol-s}$
$s$	Thickness of deposited zinc sulphide, mm
$U_c$	Velocity of the central jet, $\text{m/s}$
$V_r$	Central-to-peripheral jet velocity ratio
$x_i$	Mole fraction of $i$ th species
$x, y, z$	Coordinates in the physical domain
$Z_b$	Dimensionless distance of the block from the inflow plane

## Greek Symbols

$\xi, \eta$	Coordinates in the transformed domain
$\mu$	dynamic viscosity of argon, Pa-s
$\nu_i$	Stoichiometric coefficient for $i$ th species in the chemical reaction
$\omega_i$	Mass fraction of $i$ th species
$\omega_{A,o}$	Mass fraction of hydrogen sulphide at the inlet
$\alpha$	Injection angle of the peripheral jet
$\mathcal{R}_j^f$	Forward rate of reaction of $j$ th species mol m <sup>3</sup> s
$\mathcal{R}_j^r$	Backward rate of reaction of $j$ th species mol m <sup>3</sup> s
$\rho_c$	Density of argon, kg/m <sup>3</sup>
$\rho_{ZnS}$	Density of zinc sulphide kg/m <sup>3</sup>
$\tau_w$	Wall shear stress, N/m <sup>2</sup>

## Subscript

$o$  At the inlet

## Superscripts

$g$  Gas phase

$s$  Surface properties



# Chapter 1

## Introduction

Thin films have been the topic of a large number of investigations during the last two decades. Thin films are technologically important, particularly in the fields of semiconductor electronics and computer hardware. Thin films can be prepared by using a variety of methods, among which chemical vapour deposition is the most evolved and has received widespread acceptance. Chemical Vapour Deposition (CVD) refers to the technique of growing an epitaxial layer on a substrate by reactions in chemical species in the vapour phase across an activation energy barrier.

Applications of the CVD technique can be seen in different engineering systems, most importantly in microelectronics fabrication. It is used to produce highly uniform thin layers ( $0.01 - 10 \mu\text{m}$ ) of semiconductors such as epitaxial silicon and gallium arsenide, dielectrics such as silicon dioxide and silicon nitride. Other applications include the protective coatings of  $\text{Al}_2\text{O}_3$ ,  $\text{TiC}$ ,  $\text{SiC}$  and  $\text{B}_4\text{C}$ ; anticorrosive coatings such as  $\text{BiN}$ ,  $\text{MoSi}_2$ ,  $\text{SiC}$  and  $\text{B}_4\text{C}$ ; fibers such as  $\text{B}$ ,  $\text{B}_4\text{C}$  and  $\text{SiC}$  for composite materials and high-purity monolithic compounds such as  $\text{ZnSe}$ ,  $\text{ZnS}$ ,  $\text{CdS}$  and  $\text{CdTe}$  as infrared sensors.

The basic components of a CVD reactor are shown in Figure 1.1. It mainly contains nozzles in the inlet plane for the injection of reactants, a curved substrate, a zinc dump box where the exhaust is collected. The processes inside a CVD reactor follow a sequence. These are outlined with the help of Figure 1.2. The incoming reactants are carried to the reaction zone by the basic transport mechanisms occurring inside the CVD reactor. Here they undergo a series of chemical reactions that generate product species. The newly formed species



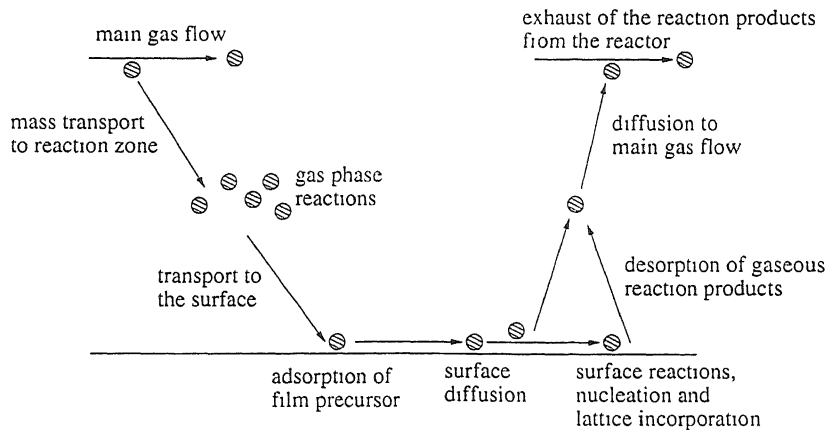


Figure 1.2: Schematic representation of the sequential processes occur in CVD reactors.

along with the remaining reactants are then transported to the susceptor. The physical species present at this location are adsorbed to the surface and are later mobilized by surface diffusion. The reactant species can also react with the susceptor and intermediates can be formed. The intermediates are either adsorbed or react to form a more stable product. In addition, nucleation and lattice incorporation lead to a thin layer of product species on the susceptor. The gaseous products desorb at the solid surface and diffuse away from the susceptor to the main gas flow. Lastly the gaseous products are exhausted with the main gas flow from the reactor.

CVD reactors may operate at atmospheric pressures (APCVD), or at low pressures (LPCVD). The operating pressure for the first type generally varies between one-tenth of an atmosphere to an atmosphere ( $0.1 - 1$  atm). In the latter, pressures are typically in the range of ( $10^{-2} - 10^{-4}$ ) atm. CVD reactors are also classified by the source from where they derive the energy for the reactions to proceed. The thermally activated reactor has gained importance over the years due to two factors. First, it provides versatility and secondly a high throughput. In this category plasma-enhanced CVD (PECVD), photo-CVD(PCVD) and electron-beam assisted CVD are the most important. Clearly the steps mentioned in Figure 1.2 are temperature dependent. At lower temperatures, surface

reactions are not fast and they constitute the rate limiting step. At higher temperatures surface reactions are quite fast compared to the mass diffusion from and to the surface. Thus at the higher temperature it is diffusion between the solid and gaseous phases that limits the transport mechanism.

Over the years various CVD geometries have evolved, horizontal reactor, pan-cake reactor and barrel reactor being the most explored. An excellent compilation of industrial reactor geometries have been given by Mahajan (1996). With the continuing trend towards larger-diameter wafers, higher quality and a decrease in minimum feature size in microelectronics manufacturing, CVD techniques will call for better understanding of the underlying transport phenomena and its relationship with the deposition characteristics. It will be a challenge to achieve  $\pm 2\%$  uniformity in layer thickness of  $0.18\text{ }\mu\text{m}$ . From Figure 1.2, it is clear that the underlying transport phenomena during chemical vapour deposition is quite important and has a strong influence in the deposition layer thickness, its uniformity and purity.

## 1.1 Literature Survey

A number of investigations comprising numerical simulations and experiments have been carried out over the last decade. Most of these investigate the role of transport phenomena in the overall growth characteristics in a CVD reactor. Growth of epitaxial silicon layer has been focused on by most authors. Emphasis has been given to the modeling aspects of the transport mechanisms inside the reactor. Selected papers on numerical modeling of CVD reactors are reviewed in the present section.

Moffat and Jensen (1988) studied the effect of three dimensional flow phenomena on critical parameters such as the deposition rate on the substrate surface. Species distribution in the reactor and the onset of natural convection in a horizontal reactor have also been studied. A system of three dimensional equations was solved numerically in an axisymmetric domain with the reactive mass transfer problem being decoupled from momentum and energy, by the assumption of a dilute solution. Applicability of a similarity solution and its limitations have been pointed out. Homogeneous chemical kinetics with surface reactions have been considered. The mechanical pressure in the reactor has been split in

the form

$$P(x, y, z) = \bar{P}(x) + p'(x, y, z)$$

where  $\bar{P}$  denotes the bulk pressure used in the axial momentum equation, driving the strong axial convective flow. The perturbation  $p'$  denotes the variation about the mean pressure and drives the transverse flow. It has been emphasized that temperature boundary conditions on the side wall influence the distribution of the species. Two types of boundary conditions have been used: (1) adiabatic, which is applicable for an air cooled system and (2) side wall temperature equal to that of the top wall, relevant in water cooled systems. In the base line study, 1 atm has been taken as the mean reactor pressure.

Klejin *et al.* (1989) solved the flow, energy and the species transport equations in two dimensional form in an axisymmetric geometry. The authors strongly recommended that the coupled system of equations should be adopted to analyze the complex transport phenomena inside a CVD reactor. Thermo-diffusion effect and multicomponent diffusion were taken into account. One interesting aspect revealed was that a deviation from the impinging jet arrangement to stagnation flow improves the growth uniformity. It was pointed out that to keep the recirculation flow caused by natural convection suppressed higher flow rates and lower total pressure are favorable. Even at 10 torr pressure, recirculation patterns appear owing to free convection.

Takoudis *et al.* (1991) developed a mathematical model for epitaxial silicon growth in a pancake reactor. The equations governing momentum, energy and species transport were numerically solved. Free jet flow was assumed due to the jet-to-reactor diameter ratio being smaller than 5. Both homogeneous gas phase reaction and the complex surface chemistries were modeled. It was pointed out that if molecular weights of the reactants and product species are quite different, thermo-diffusion effect would be important. This term contains the product of the species concentration. In the dilute solution limit it becomes low. The authors showed that with increase in flow rates and decrease in the susceptor Damkohler number, the deposition layer uniformity improve.

Duverneuil and Couderc (1992) presented a two dimensional model for silicon LPCVD. A sub-atmospheric pressure of 0.1 torr was employed for the reactor. Governing equations have been solved by the stream function- vorticity method taking a representative inter-wafer region as the physical domain. It was

hypothesized that a large number of phenomena linked to the flow, transport processes, chemical reaction reach dynamic equilibrium. They reproduce an identical scenario from one inter-wafer spacing to the next. Boundary conditions of the periodicity type were explored and analyzed in view of the ease of computations. Two-step gas phase reaction of silane pyrolysis and silylene insertion were taken as the chemical reaction model. By comparing the results of the study with a full two dimensional gas phase reaction model it was shown that in the latter, growth rate is overestimated due to the absence of rapid surface reactions.

## 1.2 Statement of the problem

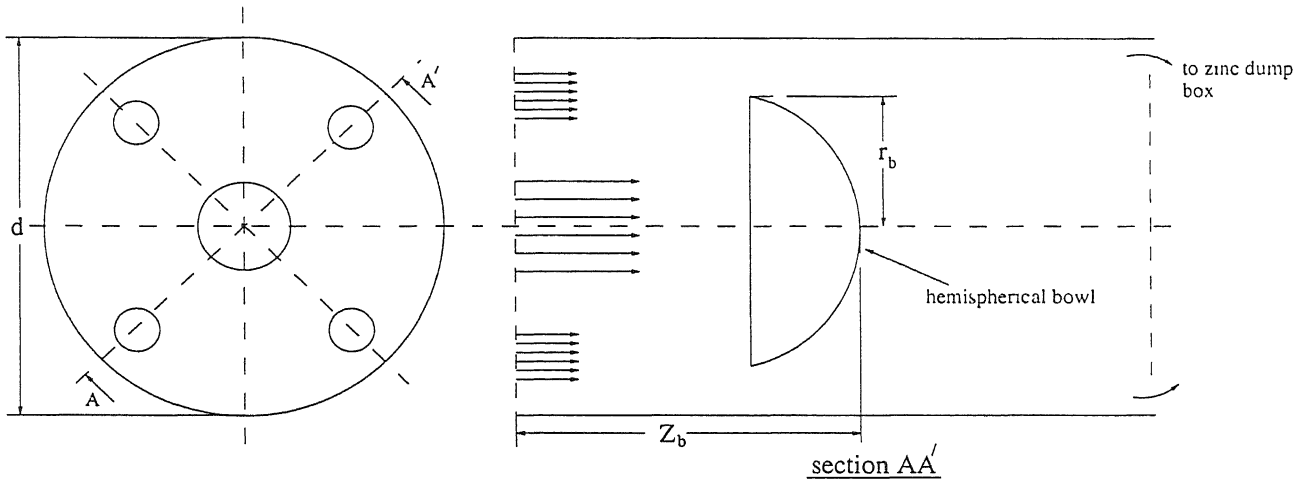


Figure 1.3: Two views of the CVD reactor

In the present study the reactor that has been analyzed does not match the CVD geometries reported in the literature. It has the characteristics of both the stagnation flow and the impinging-jet LPCVD Mahajan (1996) reactor. A vertical cross section and the side view of the reactor are shown in Figure 1.3. The basic geometry consists of a central jet and four peripheral jets positioned at an angle of  $90^\circ$  with respect to each other. Argon (A), the carrier gas mixed with hydrogen sulphide ( $H_2S$ ) is injected through the central jet while argon carrying zinc vapour (Zn) is introduced through the peripheral jets. For the simulation a two dimensional plane consisting of the central jet and two peripheral jets such

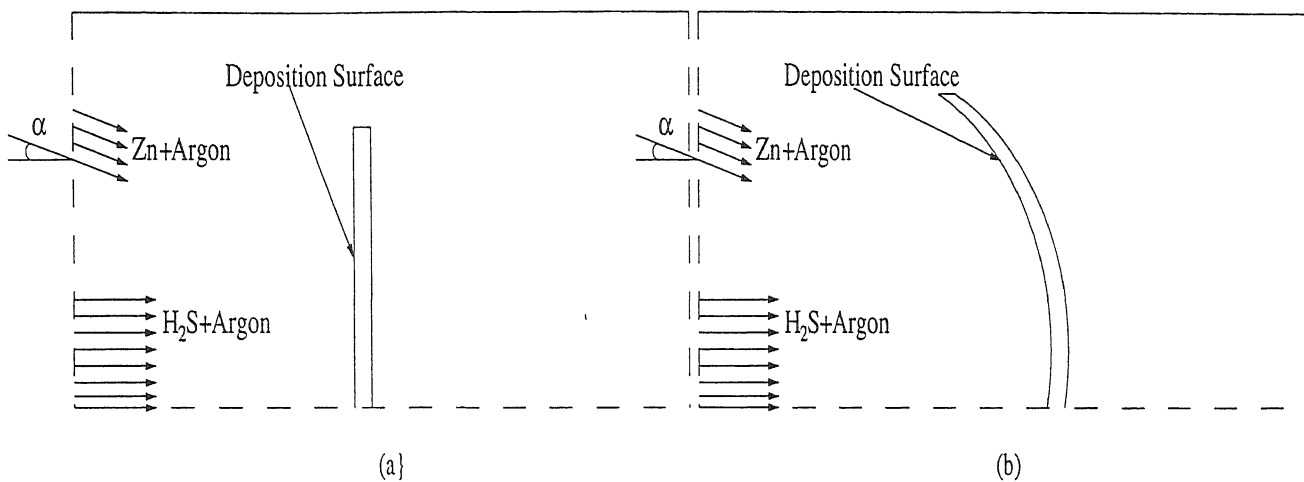


Figure 1.4: The axisymmetric two-dimensional reactor geometry employed in the present study with a flat (a) and a curved (b) deposition surface

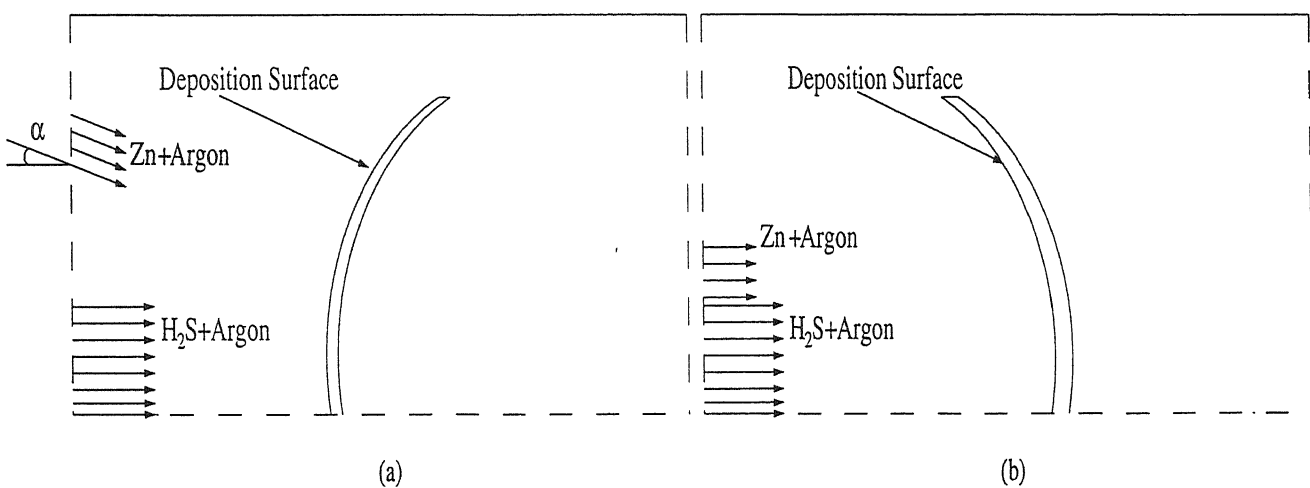


Figure 1.5: The axisymmetric two-dimensional reactor geometry employed in the present study with a convex deposition surface and jets separated by a distance (a) concave deposition surface and coaxial jets (b)

as plane AA' of Figure 1.3 is considered. Due to the inherent symmetry of the reactor, an axisymmetric configuration has been considered in the present study. Two deposition surfaces have been considered as in Figure 1.4. Figure 1.4(a) shows the deposition surface to be flat and Figure 1.4(b) shows the deposition surface to be a hemispherical bowl. The substrate surface is concave for the geometry shown in Figure 1.4(b). A variant of this geometry where the surface is convex in shape (1.5a) has also been addressed briefly. With the surface as concave but the jets being coaxial (1.5b) has also been studied.

The CVD reactor described above has been proposed to be built at CAT, Indore. The operating parameters for the proposed reactor are as follows:

1. Mass flow rate of argon through the central jet = 500-600 cc/min
2. Mass flow rate of argon through the peripheral jet = 37.5-50 cc/min
3. Vaporization rate of zinc through the peripheral jet = 7-10 gm/hr  
(mass fraction of zinc at the inlet is approximately 0.08 which is the ratio of mass flow rate of zinc through the peripheral jet and the net mass flow rate of argon)
4. Mass flow rate of hydrogen sulphide = 90-100 cc/min  
(mass fraction of hydrogen sulphide at the inlet is approximately 0.1 which is the ratio of mass flow rate of hydrogen sulphide through the central jet and the net mass flow rate of argon)
5. Mean reactor pressure = 30 mbar
6. Substrate temperature = 900 K (maximum temperature 1023 K)
7. Temperature at the central zone of the reactor = 923 K
8. Temperature of the outer most insulation at the reactor wall = 323 K

## 1.3 Thesis Organization

In Chapter 2 the set of governing equations, boundary conditions with all the approximations are written and discussed. Several modeling aspects relevant in the present study are discussed there which help to formulate these equations. Numerical techniques used to solve the governing equations and applicable boundary conditions are discussed in Chapter 3. Solution algorithm for momentum and mass transfer have been outlined. Results of grid independence test have been presented in Chapter 3. Results for the flat and curved substrate geometries have



been presented in Chapter 4 followed by results of the two alternative geometries in the same Chapter. In appendix A calculations for the species properties have been shown briefly. Validation of the fluid flow and the mass transfer codes have been shown in appendix B. The derivation of orthogonal mapping equations used in grid generation have been outlined in appendix C.

## 1.4 Objectives of the present work

The main objective of the present work has been to develop a mathematical model to study the various aspects of transport mechanism inside the proposed CVD reactor. The other objectives are listed as below:

1. To build a clear understanding of the implications of the various modeling approximations on the overall deposition process.
2. To report the computational artifacts related with the mathematical modeling. Specifically the modeling differences between an chemically active and a passive substrate.
3. Achieve a steady state solutions for the flow and concentration fields arising during the growth process. Analyze these solutions in the view of deposition characteristics.

# Chapter 2

## Mathematical Formulation

The chemical vapour deposition process is intricately controlled by fluid flow and transport phenomena in the reactor. The equations that govern the velocity, temperature and species concentration fields enforce the physical principles of conservation of mass, Newton's second law of motion and conservation of energy. These must be supplemented by equations that model chemical reactions among the species present in the carrier gas. The assumptions that lead to the reduced set of equations applicable for the proposed CVD reactor have been discussed. Several modeling aspects required in this connection have been discussed in detail. The mathematical formulation presented below draws heavily from the earlier works of Moffat and Jensen (1988), Klejin *et al.* (1989), Takoudis *et al.* (1991), Duverneuil and Couderc (2000).

### 2.1 Equations Governing Flow, Heat and Mass Transfer

#### 2.1.1 Continuity equation

The continuity equation expresses the conservation of mass in the fluid flow domain. It is written below in coordinate free form :

$$\frac{\partial \rho}{\partial t} + \nabla \cdot (\rho \mathbf{u}) = 0 \quad (2.1)$$

Expanding and writing it in a cartesian coordinate system, we get

$$\frac{\partial \rho}{\partial t} + \frac{\partial(\rho u)}{\partial x} + \frac{\partial(\rho v)}{\partial y} + \frac{\partial(\rho w)}{\partial z} = 0 \quad (2.2)$$

In the present study, the fluid flow inside the CVD reactor is limited to low velocities. Moreover, the carrier gas which carries the reactant gases to the reaction zone and the product gas to the deposition zone is in great excess, compared to the other species, leading to a dilute solution. Thus density variation inside the reactor can be neglected and the fluid flow can be considered to occur in the laminar, incompressible regime. Hence equation (2.1) reduces to

$$\nabla \cdot \mathbf{u} = 0$$

which when expanded takes the form

$$\frac{\partial u}{\partial x} + \frac{\partial v}{\partial y} + \frac{\partial w}{\partial z} = 0$$

### 2.1.2 Momentum Equations

Navier-Stokes equations govern the transport of momentum in the fluid flow domain. For incompressible, laminar flow, they can be written in compact form as

$$\rho \left( \frac{\partial \mathbf{u}}{\partial t} + \mathbf{u} \cdot \nabla \mathbf{u} \right) = -\nabla p + \mu \nabla^2 \mathbf{u} \quad (2.3)$$

Here the density and the viscosity of the carrier gas have been taken to be constant and body force to be negligible. It is convenient to combine the left side of equation (2.3) with the incompressible condition  $\nabla \cdot \mathbf{u} = 0$  to yield the so called conservative form:

$$\rho \left( \frac{\partial \mathbf{u}}{\partial t} + \mathbf{u} \cdot \nabla \mathbf{u} \right) = \rho \left( \frac{\partial \mathbf{u}}{\partial t} + \nabla \cdot (\mathbf{u} \mathbf{u}) \right)$$

The three momentum equations in cartesian coordinates are written in conservative form as follows :

**x-momentum eqn.**

$$\rho\left(\frac{\partial u}{\partial t} + \frac{\partial(u^2)}{\partial x} + \frac{\partial(uv)}{\partial y} + \frac{\partial(uw)}{\partial z}\right) = -\frac{\partial p}{\partial x} + \mu\left(\frac{\partial^2 u}{\partial x^2} + \frac{\partial^2 u}{\partial y^2} + \frac{\partial^2 u}{\partial z^2}\right) \quad (2.4)$$

**y-momentum eqn.**

$$\rho\left(\frac{\partial v}{\partial t} + \frac{\partial(vu)}{\partial x} + \frac{\partial(v^2)}{\partial y} + \frac{\partial(vw)}{\partial z}\right) = -\frac{\partial p}{\partial y} + \mu\left(\frac{\partial^2 v}{\partial x^2} + \frac{\partial^2 v}{\partial y^2} + \frac{\partial^2 v}{\partial z^2}\right) \quad (2.5)$$

**z-momentum eqn.**

$$\rho\left(\frac{\partial w}{\partial t} + \frac{\partial(wu)}{\partial x} + \frac{\partial(wv)}{\partial y} + \frac{\partial(w^2)}{\partial z}\right) = -\frac{\partial p}{\partial z} + \mu\left(\frac{\partial^2 w}{\partial x^2} + \frac{\partial^2 w}{\partial y^2} + \frac{\partial^2 w}{\partial z^2}\right) \quad (2.6)$$

### 2.1.3 Energy Equation

The equation that governs the transport of energy in a fluid system can be obtained from the conservation of energy. In cartesian coordinates, it can be written as

$$\frac{\partial T}{\partial t} + \frac{\partial(uT)}{\partial x} + \frac{\partial(vT)}{\partial y} + \frac{\partial(wT)}{\partial z} = \alpha\left(\frac{\partial^2 T}{\partial x^2} + \frac{\partial^2 T}{\partial y^2} + \frac{\partial^2 T}{\partial z^2}\right) \quad (2.7)$$

The following assumptions have been made in deriving the energy equation in the form given by equation (2.7)

1. Thermal diffusivity does not vary considerably with the temperature in the sense that an average value can be used in the analysis. This is acceptable because the CVD reactor operates under nearly isothermal conditions.
2. There is no heat sources in the flow domain. Though the reaction taking place inside the reactor is exothermic, the heat release has been taken to be minor.
3. Carrier gas is in considerable excess compared to the reacting species leading to a dilute solution. Thus concentration gradients do not lead to heat fluxes in the field. In other word, the *dufour* effect, also called the diffusion-thermo effect

has been neglected in the present study. It has been shown that this effect is only of second order importance in practical CVD systems Bird *et al.* (1960) and Hirschfelder *et al.* (1964).

4. As velocities involved in the transport processes are not high and consequently viscous dissipation effect can be neglected. It is well established that the dissipative effect due to the internal shear is important only in cases where the velocities are super-sonic or nearly so.

### 2.1.4 Species transport Equation

In thermally activated CVD reactors, we frequently encounter species transport processes coupled with chemical reactions. The governing equations for species transport is written here for the  $i$ th species using diffusive mass fluxes relative to mass-averaged velocity of the gas mixture. The mass-averaged velocity can be obtained by solving the Navier-Stokes equation and the resulting equation is similar in form to the energy equation and to each component of the Navier-Stokes equations. Let  $\omega_i$  be the mass fraction of  $i$ th species. The transport equation for each of the  $i$  species can be written as Mahajan (1996)

$$\frac{\partial(\rho\omega_i)}{\partial t} + \nabla \cdot (\rho \mathbf{u} \omega_i) = \nabla \cdot \mathbf{J}_i + \sum_{j=1}^{n_g} \nu_{ij}^g M_i \mathcal{R}_j^g \quad (2.8)$$

where the total diffusive mass flux  $\mathbf{J}_i$  of species  $i$  is composed of  $\mathbf{J}_i^c$ , the flux due to ordinary diffusion caused by a concentration gradient, the pressure diffusion  $\mathbf{J}_i^p$ , the forced diffusion  $\mathbf{J}_i^f$  and the thermal diffusion  $\mathbf{J}_i^T$ . Hence

$$\mathbf{J}_i = \mathbf{J}_i^c + \mathbf{J}_i^p + \mathbf{J}_i^f + \mathbf{J}_i^T \quad (2.9)$$

The ordinary diffusive flux in a multicomponent mixture is given by the Stefan-Maxwell equations Bird *et al.* (1960). In terms of mass fractions and species fluxes, they are written for a system containing  $n$  components as

$$\nabla \omega_i + \omega_i \nabla (\ln \bar{M}) = \frac{\bar{M}}{\rho} \sum_{j=1, j \neq i}^n \frac{1}{D_{ij} M_j} (\omega_i \mathbf{J}_j^c - \omega_j \mathbf{J}_i^c) \quad (2.10)$$

where  $\overline{M}$  is the average molecular weight of the mixture given by

$$\overline{M} = \sum_{i=1}^n M_i x_i \quad (2.11)$$

Here  $x_i$  denotes mole fraction of the  $i$ th species. Equation (2.10) is coupled to the steady state mass balance constraint

$$\sum_{i=1}^n \mathbf{J}_i^c = 0 \quad (2.12)$$

The above equations 2.10 - 2.12 form a closed set of equations for the mass fraction  $\omega_i$ . The  $n$  diffusive fluxes  $\mathbf{J}_i^c$  can then be obtained as

$$\mathbf{J}_i^c = -\rho D_{ei} \nabla \omega_i - \rho \omega_i D_{ei} \nabla (\ln \overline{M}) + \overline{M} \omega_i D_{ei} \sum_{j=1, j \neq i}^n \frac{\mathbf{J}_j^c}{M_j D_{ij}} \quad (2.13)$$

where  $D_{ei}$  the effective diffusion coefficient for species  $i$  is given by

$$D_{ei} = \left( \sum_{j=1, j \neq i}^n \frac{\overline{M} \omega_j}{M_j D_{ij}} \right)^{-1} \quad (2.14)$$

Equations (2.10) and (2.12) can be solved iteratively in conjunction with equations (2.13) and (2.14), to obtain the ordinary diffusive flux for all the species.

The thermo-diffusion term  $\mathbf{J}_i^T$ , which accounts for the diffusion of a species due to temperature gradient, is given by

$$\mathbf{J}_i^T = -D_i^T \nabla (\ln T) \quad (2.15)$$

where  $D_i^T$  is the thermo-diffusion coefficient for the species  $i$ . An approximate expression for the thermo-diffusion coefficient is given by Bird *et al.* (1960), Hirschfelder *et al.* (1964)

$$D_i^T = \sum_{j=1, j \neq i}^n \frac{c^2}{\rho} M_i M_j D_{ij} k_{ij}^T \quad (2.16)$$

The quantity  $k_{ij}^T$  is the thermo-diffusion ratio which varies from one mixture to the next. In a majority of applications, the lighter species drifts towards the zone of high temperatures and the heavier species drifts towards the zone of low temperature. This phenomena is called the Soret effect. It can be seen from equations (2.15) and (2.16) that this term is coupled with the species concentration. For a dilute solution the individual species concentration levels are quite low and this term is only of secondary importance. This limiting condition has been enforced in the present work. Details of the thermo-diffusion effect have been discussed by Hirschfelder *et al.* (1964).

The last term  $\sum \nu_{ij}^g M_i \mathcal{R}_j^g$  in the species transport equation (2.8) expresses the creation or consumption of species due to a combination of gas phase chemical reactions. The rate expressions for the chemical reactions involved depend on reaction kinetics and stoichiometry.

The present work is restricted to modeling elementary, homogeneous reactions in CVD reactors. Elementary reactions proceed in a single step and their rate expressions directly employ the stoichiometric coefficients. It is difficult to obtain the rate expression for nonelementary reactions because of the appearance of intermediate molecules. Nonelementary reactions account for the fact that a single reaction is in reality the overall effect of a sequence of several elementary reactions. In the present work, the intermediates are assumed to be so little in amount that they escape detection. The second useful scheme for classifying chemical reactions is to identify them as homogeneous or heterogeneous. A homogeneous reaction model involves only one phase of the species, usually the gas phase. For a heterogeneous reaction the species are required to be present in at least two or more phases. These two types of reactions have significant implications in mathematical modeling. A homogeneous model accounts for production/destruction rates of species throughout the domain while a heterogeneous reaction is restricted to a small portion of the flow domain. For CVD systems that produce silicon substrates this zone is the susceptor boundary. Much of the research prior on CVD systems has employed a heterogeneous reaction model with a focus on surface reactions.

In the present study, a CVD reactor in which elementary (single-step), homogeneous reaction takes place in the gas phase has been modeled. The substrate surface mounted normal to the main flow direction is chemically inert. The deposition is neither due to surface reactions nor is surface diffusion important.

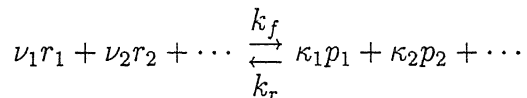
Moreover the reaction studied is instantaneous, in the sense of large reaction constants, and irreversible. Thus all reactions are confined to the gas phase. The issue of deposition has been resolved by examining the physical nature of the reaction and its products. The product species is expected to be composed of micron level particles and so the surface forces exerted on these particles overwhelm their weight. Thus the product species is assumed to be transported by the carrier gas to the substrate where it is deposited at a rate fixed by the fluid-to-solid diffusion fluxes. Thus the particles formed away from the deposition surface can be considered to be in gas phase driven by the base flow field towards the deposition surface. On the deposition surface the product species can be considered as a solid while the reaction takes place in the gas phase. In this respect, considering the reaction to be homogeneous is justified. As the product species deposited on the substrate does not return to the flow, the reverse reaction has not been accounted for.

In view of the above approximations, the stoichiometry involved in the present work is quite simple and a single step elementary reaction has been chosen to express the rate kinetics. The rate expression of a chemical reaction acts as a mass source of species in the transport equation, but depends on the fields of concentration and temperature. The temperature dependence is due to the fact that reaction rate constants obey the Arrhenius' law Levenspiel (1999) given by

$$k = k_0 \exp\left(-\frac{E_a}{RT}\right)$$

where  $k_0$  is the pre-exponential factor,  $E_a$  is the activation energy and  $R$  is the universal gas constant. In the present study an arbitrary large value compatible with double precision arithmetic has been assigned to the rate constant as the reaction is assumed to be instantaneous in nature.

Consider a reversible reaction of the type



where  $r$  and  $p$  denote reactants and products, respectively. The net rate of creation of species  $j$  is given by

$$\mathcal{R}_j = \mathcal{R}_j^f - \mathcal{R}_j^r$$

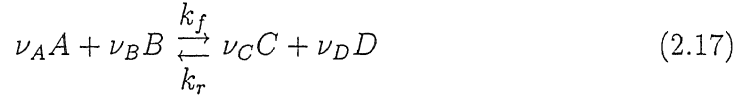


where  $\mathcal{R}_j^f$  and  $\mathcal{R}_j^r$  are the forward and backward reaction rates, respectively, given by

$$\begin{aligned}\mathcal{R}_j^f &= k_f \prod_i c_{r_i} \\ &= k_f \prod_i (\rho \omega_{r_i})\end{aligned}$$

$$\begin{aligned}\mathcal{R}_j^r &= k_r \prod_i c_{p_i} \\ &= k_r \prod_i (\rho \omega_{p_i})\end{aligned}$$

Thus for a reaction containing four species



the reaction rates for species  $C$  is given by

$$\mathcal{R}_C = \mathcal{R}_C^f - \mathcal{R}_C^r \quad (2.18)$$

where the forward and backward reaction rates are given by

$$\mathcal{R}_C^f = k_f (\rho \omega_A) (\rho \omega_B) \quad (2.19)$$

$$\mathcal{R}_C^r = k_r (\rho \omega_C) (\rho \omega_D) \quad (2.20)$$

For an elementary (single-step) reaction, the rates of reactants and products are related by the stoichiometric coefficients in the following relationship Levenspiel (1999)

$$\frac{\mathcal{R}_A}{\nu_A} = \frac{\mathcal{R}_B}{\nu_B} = -\frac{\mathcal{R}_C}{\nu_C} = -\frac{\mathcal{R}_D}{\nu_D} \quad (2.21)$$

Several additional simplifications appropriate for the CVD reactor being modeled are listed below

1. In atmospheric and sub-atmospheric CVD reactors, the carrier gas is in considerable excess compared to the reactant species in order to avoid homogeneous nucleation of particulates. Thus the dilute solution approximation can be enforced to develop the transport equation.
2. In view of the dilute solution approximation, the presence of other species on a certain transported species can be neglected. Thus ordinary diffusion is governed by the Fick's law of binary diffusion. In case of a multicomponent diffusion system equations (2.10) and (2.12) are solved to get the ordinary diffusive fluxes of each species. These are then inserted in the transport equation to solve for the species concentration field.
3. In a low pressure CVD reactor, the pressure gradient encountered is not significant enough to separate the chemical species. Hence the pressure diffusion term can be neglected.
4. The forced diffusion term is identically zero if gravity is the only external force Mahajan (1996).
5. The thermo-diffusion effect may be considerable in regions of sharp temperature gradients and in multicomponent mixtures where the molecular weights of the species are not close to one another. For the CVD reactor under discussion, temperature changes about the mean value of  $700^{\circ}\text{C}$  are within  $\pm 1^{\circ}\text{C}$ . Hence the thermo-diffusion effect can be neglected in the formulation.
6. In view of the near constancy of temperature in the reactor, temperature dependence of the binary diffusion coefficients and density of the carrier gas have been neglected.

With the help of above mentioned approximations, the diffusive mass flux for the  $i$ th species is given by

$$\mathbf{J}_i = \mathbf{J}_i^c = -D_{ij}\nabla(\rho\omega_i) \quad (2.22)$$

with  $j$  corresponds to the carrier gas and  $\mathbf{J}_i^c$  is the ordinary diffusion flux of species  $i$  into the carrier gas. Hence the simplified form of the species transport equation takes the form

$$\frac{\partial(\rho\omega_i)}{\partial t} + \nabla \cdot (\rho \mathbf{u} \omega_i) = \nabla \cdot (-D_{ij} \nabla(\rho\omega_i)) + \sum_{j=1}^{n_g} \nu_{ij} M_i \mathcal{R}_j^g \quad (2.23)$$

By inserting the rate expressions, namely equations (2.19) and (2.20), into the governing equation we can form the complete set of equations that govern the species concentration field. For a reaction of the form given by equation (2.17), the governing equations have been written explicitly for all the species as follows

species A

$$\begin{aligned} \frac{\partial(\rho\omega_A)}{\partial t} + \frac{\partial(\rho u \omega_A)}{\partial x} + \frac{\partial(\rho v \omega_A)}{\partial y} + \frac{\partial(\rho w \omega_A)}{\partial z} = \rho D_A \left( \frac{\partial^2 \omega_A}{\partial x^2} + \frac{\partial^2 \omega_A}{\partial y^2} + \frac{\partial^2 \omega_A}{\partial z^2} \right) \\ + \nu_A M_A [k_r(\rho\omega_C)(\rho\omega_D) - k_f(\rho\omega_A)(\rho\omega_B)] \end{aligned} \quad (2.24)$$

species B

$$\begin{aligned} \frac{\partial(\rho\omega_B)}{\partial t} + \frac{\partial(\rho u \omega_B)}{\partial x} + \frac{\partial(\rho v \omega_B)}{\partial y} + \frac{\partial(\rho w \omega_B)}{\partial z} = \rho D_B \left( \frac{\partial^2 \omega_B}{\partial x^2} + \frac{\partial^2 \omega_B}{\partial y^2} + \frac{\partial^2 \omega_B}{\partial z^2} \right) \\ + \nu_B M_B [k_r(\rho\omega_C)(\rho\omega_D) - k_f(\rho\omega_A)(\rho\omega_B)] \end{aligned} \quad (2.25)$$

species C

$$\begin{aligned} \frac{\partial(\rho\omega_C)}{\partial t} + \frac{\partial(\rho u \omega_C)}{\partial x} + \frac{\partial(\rho v \omega_C)}{\partial y} + \frac{\partial(\rho w \omega_C)}{\partial z} = \rho D_C \left( \frac{\partial^2 \omega_C}{\partial x^2} + \frac{\partial^2 \omega_C}{\partial y^2} + \frac{\partial^2 \omega_C}{\partial z^2} \right) \\ + \nu_C M_C [k_f(\rho\omega_A)(\rho\omega_B) - k_r(\rho\omega_C)(\rho\omega_D)] \end{aligned} \quad (2.26)$$

species D

$$\begin{aligned} \frac{\partial(\rho\omega_D)}{\partial t} + \frac{\partial(\rho u \omega_D)}{\partial x} + \frac{\partial(\rho v \omega_D)}{\partial y} + \frac{\partial(\rho w \omega_D)}{\partial z} = \rho D_D \left( \frac{\partial^2 \omega_D}{\partial x^2} + \frac{\partial^2 \omega_D}{\partial y^2} + \frac{\partial^2 \omega_D}{\partial z^2} \right) \\ + \nu_D M_D [k_f(\rho\omega_A)(\rho\omega_B) - k_r(\rho\omega_C)(\rho\omega_D)] \end{aligned} \quad (2.27)$$

where  $\nu_i$  corresponds to the stoichiometric coefficient of the  $i$ th species in the chemical reaction given by equation (2.17).

## 2.2 Nondimensionalization of the governing equations

Nondimensionalization of the governing equations facilitates parametric study over a smaller set of flow properties and geometric variables to get an insight into the transport phenomena inside the CVD reactor. The scales for the dependent and independent variables for normalization are written below :

$$u^* = \frac{u}{U_c}, \quad v^* = \frac{v}{U_c}, \quad w^* = \frac{w}{U_c}, \quad \rho^* = \frac{\rho}{\rho_{ca}}, \quad p^* = \frac{p}{\rho U_c^2}, \quad t^* = \frac{t U_c}{d}, \quad x^* = \frac{x}{d}$$

$$y^* = \frac{y}{d}, \quad z^* = \frac{z}{d}, \quad T^* = \frac{T - T_b}{T_a - T_b}, \quad \omega_i^* = \frac{\omega_i}{\omega_{A,o}}, \quad \mathfrak{R}_j^* = \frac{\mathfrak{R}_j}{\rho \omega_{A,o}^2}, \quad D_i^* = \frac{D_i}{D_{i,o}}$$

Here  $T_a$  and  $T_b$  are two convenient reference temperatures in the reactor. Substituting the normalized quantities in the governing equations we get the set of nondimensionalized equations. These are presented below after dropping the superscript (\*).

### continuity equation

$$\frac{\partial \rho}{\partial t} + \frac{\partial(\rho u)}{\partial x} + \frac{\partial(\rho v)}{\partial y} + \frac{\partial(\rho w)}{\partial z} = 0 \quad (2.28)$$

### x momentum equation

$$\frac{\partial(\rho u)}{\partial t} + \frac{\partial(u^2)}{\partial x} + \frac{\partial(uv)}{\partial y} + \frac{\partial(uw)}{\partial z} = -\frac{\partial p}{\partial x} + \frac{1}{\text{Re}} \left( \frac{\partial^2 u}{\partial x^2} + \frac{\partial^2 u}{\partial y^2} + \frac{\partial^2 u}{\partial z^2} \right) \quad (2.29)$$

### y momentum equation

$$\frac{\partial(\rho v)}{\partial t} + \frac{\partial(vu)}{\partial x} + \frac{\partial(v^2)}{\partial y} + \frac{\partial(vw)}{\partial z} = -\frac{\partial p}{\partial y} + \frac{1}{\text{Re}} \left( \frac{\partial^2 v}{\partial x^2} + \frac{\partial^2 v}{\partial y^2} + \frac{\partial^2 v}{\partial z^2} \right) \quad (2.30)$$

### z momentum equation

$$\frac{\partial(\rho w)}{\partial t} + \frac{\partial(wu)}{\partial x} + \frac{\partial(wv)}{\partial y} + \frac{\partial(w^2)}{\partial z} = -\frac{\partial p}{\partial z} + \frac{1}{\text{Re}} \left( \frac{\partial^2 w}{\partial x^2} + \frac{\partial^2 w}{\partial y^2} + \frac{\partial^2 w}{\partial z^2} \right) \quad (2.31)$$

where  $\text{Re} = \frac{\rho_{ca} U_c d}{\mu}$ , the Reynolds number is based on the central jet velocity, reactor diameter and the viscosity of the carrier gas at the average reactor temperature.

### Energy equation

$$\frac{\partial T}{\partial t} + \frac{\partial(uT)}{\partial y} + \frac{\partial(vT)}{\partial y} + \frac{\partial(wT)}{\partial z} = \frac{1}{\text{Pe}_H} \left( \frac{\partial^2 T}{\partial x^2} + \frac{\partial^2 T}{\partial y^2} + \frac{\partial^2 T}{\partial z^2} \right) \quad (2.32)$$

where  $\text{Pe}_H = \frac{U_c d}{\alpha_{ca}}$ , the Peclet number for heat transfer is based on the central jet velocity, diameter of the reactor and the thermal diffusivity of the carrier gas at the average reactor temperature.

### Species transport equations

species A

$$\begin{aligned} \frac{\partial(\rho\omega_A)}{\partial t} + \frac{\partial(\rho u\omega_A)}{\partial x} + \frac{\partial(\rho v\omega_A)}{\partial y} + \frac{\partial(\rho w\omega_A)}{\partial z} &= \frac{1}{\text{Pe}_m} \frac{D_{A,o}}{D_{A,o}} \left[ \frac{\partial}{\partial x} \left( \rho D_A \frac{\partial \omega_A}{\partial x} \right) \right. \\ &\quad \left. + \frac{\partial}{\partial y} \left( \rho D_A \frac{\partial \omega_A}{\partial y} \right) + \frac{\partial}{\partial z} \left( \rho D_A \frac{\partial \omega_A}{\partial z} \right) \right] \\ &\quad + \nu_A \frac{d}{U_c} \omega_{A,o} \frac{\rho_c}{M_c} \frac{M_A}{M_c} (k_r \omega_C \omega_D - k_f \omega_A \omega_B) \end{aligned} \quad (2.33)$$

species B

$$\begin{aligned} \frac{\partial(\rho\omega_B)}{\partial t} + \frac{\partial(\rho u\omega_B)}{\partial x} + \frac{\partial(\rho v\omega_B)}{\partial y} + \frac{\partial(\rho w\omega_B)}{\partial z} &= \frac{1}{\text{Pe}_m} \frac{D_{B,o}}{D_{A,o}} \left[ \frac{\partial}{\partial x} \left( \rho D_B \frac{\partial \omega_B}{\partial x} \right) \right. \\ &\quad \left. + \frac{\partial}{\partial y} \left( \rho D_B \frac{\partial \omega_B}{\partial y} \right) + \frac{\partial}{\partial z} \left( \rho D_B \frac{\partial \omega_B}{\partial z} \right) \right] \\ &\quad + \nu_B \frac{d}{U_c} \omega_{A,o} \frac{\rho_c}{M_c} \frac{M_B}{M_c} (k_r \omega_C \omega_D - k_f \omega_A \omega_B) \end{aligned} \quad (2.34)$$

species C

$$\begin{aligned}
\frac{\partial(\rho\omega_C)}{\partial t} + \frac{\partial(\rho u\omega_C)}{\partial x} + \frac{\partial(\rho v\omega_C)}{\partial y} + \frac{\partial(\rho w\omega_C)}{\partial z} &= \frac{1}{\text{Pe}_m} \frac{D_{C,o}}{D_{A,o}} \left[ \frac{\partial}{\partial x} \left( \rho D_C \frac{\partial \omega_C}{\partial x} \right) \right. \\
&\quad \left. + \frac{\partial}{\partial y} \left( \rho D_C \frac{\partial \omega_C}{\partial y} \right) + \frac{\partial}{\partial z} \left( \rho D_C \frac{\partial \omega_C}{\partial z} \right) \right] \\
&\quad + \nu_C \frac{d}{U_c} \omega_{A,o} \frac{\rho_c}{M_c} \frac{M_C}{M_c} (k_f \omega_A \omega_B - k_r \omega_C \omega_D)
\end{aligned} \tag{2.35}$$

species D

$$\begin{aligned}
\frac{\partial(\rho\omega_D)}{\partial t} + \frac{\partial(\rho u\omega_D)}{\partial x} + \frac{\partial(\rho v\omega_D)}{\partial y} + \frac{\partial(\rho w\omega_D)}{\partial z} &= \frac{1}{\text{Pe}_m} \frac{D_{D,o}}{D_{A,o}} \left[ \frac{\partial}{\partial x} \left( \rho D_D \frac{\partial \omega_D}{\partial x} \right) \right. \\
&\quad \left. + \frac{\partial}{\partial y} \left( \rho D_D \frac{\partial \omega_D}{\partial y} \right) + \frac{\partial}{\partial z} \left( \rho D_D \frac{\partial \omega_D}{\partial z} \right) \right] \\
&\quad + \nu_D \frac{d}{U_c} \omega_{A,o} \frac{\rho_c}{M_c} \frac{M_D}{M_c} (k_f \omega_A \omega_B - k_r \omega_C \omega_D)
\end{aligned} \tag{2.36}$$

where  $\text{Pe}_m = \frac{U_c d}{D_{A,o}}$  is the Peclet number associated with the mass transfer based on central jet velocity, diameter of the reactor and the binary diffusion coefficient of species A into the carrier gas at the average reactor temperature.

In the present study, the system of equations including the continuity equation, momentum equations and the species transport equations are taken to be segregated in the sense that the flow field is independent of the concentration and temperature fields. This is justified because the reactants and products are in a dilute solution. Moreover, with the coupled system approach, the computational effort is enormous. Any effect pertaining to the momentum transport and the species transport related to the changes in the temperature field have not been studied. Hence the energy equation has been excluded from the governing equations. The focus of the present work is on the steady state concentration fields of species A - D and the deposition rate on the substrate placed in front of the incoming jets.

## 2.3 Initial and boundary conditions

The governing equations of section 2.2 require both initial and boundary conditions for a complete solution. These are summarized below.

### 2.3.1 Initial condition

The initial condition is quite important from a computational point-of-view. However when a steady state solution is sought, any initial field can be assigned to the dependent variables. In addition, converged fields at a lower Peclet number or a coarser grid can also be employed. These aspects are discussed in chapter 3.

### 2.3.2 Boundary conditions

Boundary conditions at various surfaces of the reactor are discussed here

#### Solid surfaces

At solid surfaces, no-slip conditions are applicable for the three components of velocities, written as

$$u = 0, \quad v = 0, \quad w = 0 \quad (2.37)$$

For the energy equation either constant wall temperature or constant wall heat flux are prescribed at a solid surface, namely

$$T = \text{specified} \quad \text{or} \quad \mathbf{q} = -k\nabla T = \text{specified} \quad (2.38)$$

For the species transport equations, the net mass flux of  $i$ th species must equal the rate of production of species  $i$  through  $n_s$  surface reactions at the surface. Hence

$$(\rho\omega_i\mathbf{u} + \mathbf{J}_i) \cdot \mathbf{n} = - \sum_{j=1}^{n_s} \nu_{ij}^s M_i \mathcal{R}_j^s \quad (2.39)$$

With the absence of any surface reactions and the no-slip velocity boundary conditions the above condition reduces to the following form with only ordinary diffusion in place :

$$\mathbf{J}_i \cdot \mathbf{n} = \mathbf{J}_i^c \cdot \mathbf{n} = 0 \quad (2.40)$$

where  $\mathbf{n}$  is the normal unit vector on the surface. In the present study, all the solid surfaces are passive and impermeable. Hence the above boundary condition (2.40) is appropriate for the species transport equations. This condition has special significance for the deposition surface and is discussed in detail in chapter 3.

### Inlet plane

At the inlet, velocities are prescribed as

$$u, v, w = \text{specified} \quad (2.41)$$

for the energy equation temperature is specified at the inlet :

$$T = \text{given} \quad (2.42)$$

For the species transport equation prescribed species concentration and no net diffusion flux at the walls are appropriate. The species concentration can be calculated as the ratio of known mass flow rates of the various species and the carrier gas. Hence, it follows that

$$\omega_i = \text{specified at jet locations and } \mathbf{J}_i^c \cdot \mathbf{n} = 0 \text{ on solid surfaces} \quad (2.43)$$

### Exit plane

At the exit plane sufficiently away from the reaction and deposition zone, zero derivatives of the dependent variables in the stream-wise direction has been enforced :

$$\nabla \phi \cdot \mathbf{n} = 0 \quad (2.44)$$

where  $\mathbf{n}$  is the unit vector along the stream-wise direction at the exit plane. Here  $\phi$  denotes all the dependent variables such as velocities  $u, v$  and  $w$ , temperature  $T$  and concentration  $\omega_i$ .



## At the Axis

For the reactors with axisymmetric geometry no radial variation of the dependent variables at the axis is permitted. Hence

$$(\nabla\phi).\mathbf{n} = 0 \quad (2.45)$$

where  $\phi$  denotes all the dependent variables namely velocities, temperature and concentration and  $\mathbf{n}$  denotes the unit normal vector on the axis.

## 2.4 Range of parameters

To get a clear idea about the transport mechanism inside the reactor and the effect of geometry, a parametric study has been conducted. While carrying out the study one parameter has been changed at a time, keeping all other variables fixed. The effect of this parameter on the transport phenomena and the deposition rate on the substrate inside the reactor have been studied. The dimensionless parameters relevant to the present work are written below :

### Reynolds number

In fluid mechanics Reynolds number signifies the ratio of the inertia force and the viscous force acting in tandem, given by

$$\text{Re} = \frac{\rho U_{ref} L_c}{\mu}$$

where  $U_{ref}$  is the reference velocity of the problem considered,  $L_c$  is the characteristic length associated with the fluid flow,  $\rho$  and  $\mu$  are the density and viscosity of the fluid. At various Reynolds numbers we get an idea about the viscous effects on the flow and the size of the recirculation region in relation to the position of the substrate. It also gives us an idea of the effect of mass flow rate on the deposition profile because Reynolds number is directly linked with the mass flow rate

of the carrier gas. In the present study the range of Reynolds number considered is 10 - 100.

### **Blockage ratio**

Blockage ratio defined as the flow passage blocked due to the presence of the solid obstacle relative to the reactor tube radius. It clearly gives us an idea how the substrate size, compared to the reactor dimension, affects the flow pattern and, in turn, the uniformity of the deposited material.

### **Block position**

In the actual reactor the substrate should be placed such that the reactants react in front of it and the product species get deposited on the desired surface. If it is too close to the injector nozzle plane, this can lead to reactions behind the substrate surface. Too large a distance from the nozzle leads to an excessive loss of the product material before it is deposited on the substrate.

### **Velocity ratio of the central and peripheral jets**

For the mixing of the reactant species at a favorable position in relation to the position of the substrate the jet velocity ratio should be properly selected for a certain geometric configuration. This ratio also dictates the availability of the reactant species to each other in the region before the deposition surface.

### **Jet angle**

The angle at which fluid is injected from the central and the peripheral jet is quite important in the sense that it significantly influences the extent of mixing. It is expected that if the peripheral jet is injected towards the central jet mixing of the streams occurs near the inlet plane. But if the jets are placed parallel to each

other than the mixing and in turn the reaction zone is shifted to a downstream location.

## 2.5 Shear stress on the solid surfaces

Wall shear stresses in internal flows indicate a scaled magnitude of the velocity gradient at the solid surface. It is likely that the uniform deposition of the product species will be strongly correlated with a uniformity in shear stress at the substrate surface. This is because changes in the velocity gradient will also affect the rate of deposition. Moreover at high levels of the shear stress, the species particles do not get the required residence time to deposit uniformly leading to a nonuniform layer of the deposited material. Thus shear stresses at both the tube walls and the substrate surface are important for accurately predicting the flow patterns and the deposition characteristics.

# Chapter 3

## Numerical Solution

In this chapter numerical techniques utilized to solve the complete set of equations for flow and mass transfer are discussed in detail. The first section is devoted to orthogonal grid generation that is important for computation in complex geometries. The finite volume method for solving the Navier-Stokes equations is described subsequently in detail.

### 3.1 Orthogonal Grid Generation

The success of numerical simulation of a system of partial differential equations is strongly dependent on the quality of the grid. For numerical simulation of flow in complex geometries, body conforming curvilinear grid lines are necessary. This is essential to accurately satisfy the boundary conditions. The exactness with which the boundary conditions are satisfied significantly influences the numerical solution. There are well-established techniques available in the literature Chikhliwala and Yortsos (1985), Duraiswami and prosperetti (1992), Nair and Sengupta (1998) and Beale(1999) to generate body conforming coordinate system. Examples are conformal mapping, transfinite interpolations and methods based on elliptic PDEs. In the present work we have used an elliptic partial differential equation for grid generation.

### 3.1.1 Elliptic Grid Generation

The generation of boundary-conforming coordinate system is accomplished by determination of the curvilinear coordinates in the interior of a physical domain from specified values (and/or slope of the coordinate lines at the boundary) on the boundary of the domain; one coordinate remains constant along each curvilinear line while the other varies monotonically on that line.

The problem can be seen (in 2-D) as finding the locations of “field points” in the solution domain, which correspond to regularly spaced grid points in a rectangular transformed  $(\xi, \eta)$  geometry. The generation of field values of a function from boundary values can be done in various ways. One approach is to use interpolation between the boundaries. Alternatively, the field values can be thought of as solution of a boundary-value problem. The essence of this technique is to solve a set of elliptic partial differential equation with complete boundary correspondence. Essentially, when coordinates on all the boundaries are completely specified such as  $0 \leq \xi \leq 1$ ,  $\eta = 0, 1$  and  $0 \leq \eta \leq 1$ ,  $\xi = 0, 1$ , a well-posed Dirichlet problem is obtained. Some of the important characteristics of the elliptic system with Dirichlet boundary conditions are listed below

1. The system of elliptic PDEs obeys the extremum principle Muralidhar and Sundararajan (1995), stated as follows :

Let the governing equation be of the form

$$\nabla^2 \xi = P \text{ over } \Omega \quad (3.1)$$

where  $\nabla^2$  is the Laplacian operator and  $P$  is a prescribed function of  $x$  and  $y$ .

- (a) If  $P > 0$ , the maximum values of  $\xi$  occur on the boundary  $\partial\Omega$  ;
- (b) If  $P < 0$ , the minimum values of  $\xi$  occur on the boundary  $\partial\Omega$  ; and

(c) If  $P = 0$ , both the maximum and minimum values of  $\xi$  occur on the boundary  $\partial\Omega$ .

Property (c) is desirable as it ensures the generated grids represent one-to-one mapping. If the linear operator chosen for grid generation violates the extremum principle, curvilinear lines may fold back into the physical domain. This is clearly not acceptable because the extrema that lie inside the domain will lead to an overlap of the curvilinear coordinate lines.

2. Elliptic operator has an inherent smoothness property that prevails over the solution derived for the whole domain. Specifically boundary discontinuities do not propagate into the domain.

### 3.1.2 Orthogonal grid generation

The elliptic generation system generates boundary conforming coordinate lines but does not ensure orthogonality of the grid lines throughout the solution domain. At the boundaries the grid line slope can be however specified as orthogonal. Orthogonality is an important property of the curvilinear coordinate system required from the computational point of view. By maintaining orthogonality of the grid lines the following advantages can be achieved Ryskin and Leal (1983), Thompson *et al.* (1985), Eca(1996):

1. Grid distortion can be minimized which in turn reduces the possibility of incurring greater truncation error in the finite difference expressions.
2. The same order of accuracy for all the terms in the governing partial differential equations can be maintained to the level set by the discretization techniques associated with the finite volume formulation.
3. With the orthogonality constraint the grid generation equation has fewer terms and thus reduces the amount of computations required.

The derivation of the orthogonal grid generation equations are outlined in appendix C. The two dimensional form of the partial differential equation used in the present work is written as :

$$\frac{\partial}{\partial \xi} \left( f \frac{\partial x}{\partial \xi} \right) + \frac{\partial}{\partial \eta} \left( \frac{1}{f} \frac{\partial x}{\partial \eta} \right) = 0 \quad (3.2)$$

$$\frac{\partial}{\partial \xi} \left( f \frac{\partial y}{\partial \xi} \right) + \frac{\partial}{\partial \eta} \left( \frac{1}{f} \frac{\partial y}{\partial \eta} \right) = 0 \quad (3.3)$$

where  $f$  is the distortion function given by

$$f = \frac{\sqrt{x_\eta^2 + y_\eta^2}}{\sqrt{x_\xi^2 + y_\xi^2}} \quad (3.4)$$

The solution  $x(\xi, \eta)$  and  $y(\xi, \eta)$  of these PDEs provide the mapping between the physical  $(x, y)$  domain and the transformed  $(\xi, \eta)$  rectangular domain. The two PDEs are supplemented by boundary conditions that assign  $(\xi, \eta)$  values to the boundary points  $(x_b, y_b)$ .

### 3.1.3 Numerical solution

Equations (3.2) and (3.3) are strongly nonlinear and can be solved by an iterative technique in the rectangular transformed domain. In the present study the generation equations are solved by the finite difference technique with all the derivatives being discretized by second order difference formulas. The most important issue in the solution of these equations is the determination of the distortion function  $f(\xi, \eta)$  in the solution domain. There are three possibilities for calculating the distortion function and they are listed below Eca(1996):

1. Evaluate  $f$  from its definition expression (3.4) at all the points in the domain.
2. Determine  $f$  from its definition expression over the boundaries where the physical coordinates are completely given. Next evaluate  $f$  in the solution domain

by a suitable algebraic interpolation scheme or by solving a Laplace equation for  $f$  given by

$$\nabla^2 f = 0$$

3. Choose  $f$  as a suitable algebraic function. This approach calls for experience and skill as it crucially depends on the geometry and the mapping layout.

In the present study we have adopted the second alternative as this approach involves lesser amount of calculations. As equations (3.2) and (3.3) are nonlinear, they are linearized by evaluating the distortion function  $f$  by values of coordinates from the previous iteration. The orthogonality constraint on the curvilinear coordinates are imposed by making the off-diagonal elements of the metric tensors to vanish which yields the form of orthogonal boundary condition as

$$x_\xi x_\eta + y_\xi y_\eta = 0 \quad (3.5)$$

Clearly this boundary condition is of nonlinear type. It is satisfied iteratively inside the global iteration cycle that solves the generation equation. It is to be noted that for a vertical boundary,  $x$  coordinates are kept fixed and  $y$  coordinates are calculated by the relation (3.5). For a horizontal boundary, the procedure is reversed.

The solution algorithm for orthogonal grid generation can now be summarized as follows:

1. Develop an initial approximation for the grid. In the present work, algebraic interpolation has been used. It has been observed that a reasonably good initial guess leads to a fewer number of global iteration cycles.
2. Determine the distortion function at the boundaries and evaluate the function for the whole domain by using transfinite interpolation.



3. Solve equations (3.2) and (3.3) with a fixed  $f(\xi, \eta)$  by an iterative technique. Satisfy all the boundary conditions.
4. Return to step 2 if convergence criterion is not satisfied.

It has been seen that if at all the boundaries, the coordinates are specified, the solution converges rapidly, while the orthogonality criterion at the boundaries impedes the rate of convergence. Secondly, it is a well-established fact that near a convex boundary grid lines get attracted towards each other and near a concave boundary they get repelled by each other. Due to attraction-repulsion between the grid lines, the non-uniformity of the grid lines increases significantly. This is detrimental to the efficient numerical computations of the governing equations. In the present study we solve the set of governing equations in the physical domain itself, and the magnitude of the metric tensors of the generated grid do not affect the flow field solution. Thus the grid generation equations have not been solved to machine accuracy. Instead, coarser convergence limits at which the grid had an acceptable distribution were employed, so as to get relatively undistorted grids.

## 3.2 Solution of the Mass and Momentum equations

In the present study the momentum equations are solved by finite volume method in the physical domain itself. This is justified because in the transformed domain the governing equations become quite elaborate and a heavy computational effort is required. We have worked with cartesian components of velocities and the variables have been arranged over a non-staggered mesh. Solution in non-staggered grids can lead to pressure-velocity decoupling, in turn resulting in a pressure field completely independent of the velocity Patankar (1980). To avoid the velocity-pressure decoupling associated with calculations in non-staggered grids, momentum interpolation proposed by earlier authors Rhie and Chow (1983), Majumdar (1988), Miller and Schmidt (1988) and Choi *et al.* (1993) has been used. The discretization of the various terms and the solution strategy is discussed in the following sections.

### 3.2.1 Governing equations in integral form

All the transport equations we encounter can be cast as the generic advection-diffusion equation with a passive scalar being transported in the fluid domain. This scalar is an intensive property, for example momentum per unit mass, enthalpy and concentration. The Navier Stokes equation in the laminar, incompressible flow regime for an arbitrary control volume in the physical domain can be written in the integrated form of a generic advection-diffusion equation as follows :

$$\frac{\partial}{\partial t} \int_{CV} \rho dV + \int_{CS} \rho \mathbf{u} \cdot d\mathbf{S} = 0 \quad (3.6)$$

$$\frac{\partial}{\partial t} \int_{CV} \rho \phi dV + \int_{CS} (\rho \mathbf{u} \phi - \Gamma_\phi \nabla \phi) \cdot d\mathbf{S} = \int_{CV} S_\phi dV \quad (3.7)$$

where  $\rho$  represents fluid density,  $\phi$  stands for any intensive property being transported and  $S_\phi$  is the volumetric source term. Further,  $\mathbf{u}$  is the velocity vector and  $\Gamma_\phi$  is the diffusion coefficient of the scalar  $\phi$ . For the incompressible flow the above equations take the form

$$\int_s \rho \mathbf{u} \cdot d\mathbf{S} = 0 \quad (3.8)$$

$$\frac{\partial}{\partial t} \int_v \phi dV + \int_s (\mathbf{u} \phi - \frac{\Gamma_\phi}{\rho} \nabla \phi) \cdot d\mathbf{S} = \frac{1}{\rho} \int_v S_\phi dV \quad (3.9)$$

In present calculations for the three momentum equations  $u, v, w$  take the place of  $\phi$ .

### 3.2.2 Description of the finite volume method

Equations (3.8) and (3.9) are evaluated over small volumes called *finite volumes* to generate the discretized form of the governing equations. The solution domain is divided into a number of contiguous hexahedral finite volumes. The volumes are defined by the coordinates of their eight vertices. In complex geometries the finite volumes are formed by joining the eight vertices by straight lines.

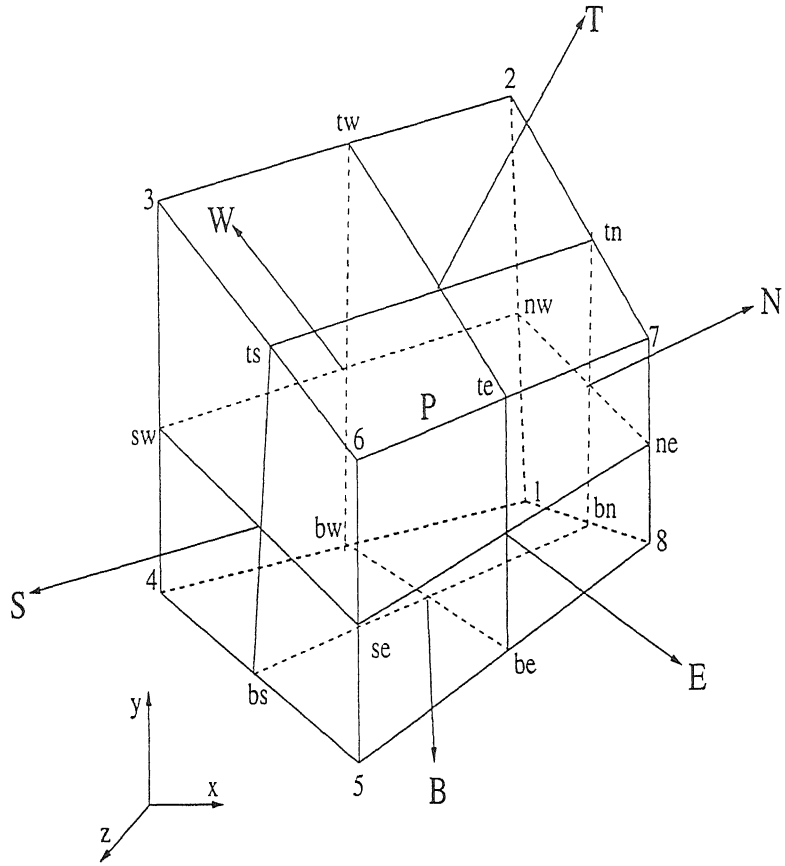


Figure 3.1: A typical finite volume employed in the computation.

A typical finite volume is shown in Figure (3.1). The coordinates of the vertices of the control volumes are generated by grid generation technique of section 3.1. The six neighbouring control volumes of  $P$  are denoted by  $E, W, N, S, T, B$  for the east, west, north, south, top and bottom control volumes respectively. The cell face centres are denoted by  $e, w, n, s, t, b$  in the same order. Edge centres are denoted by  $te, tn, tw, ts, be, bn, bw, bs, ne, nw, sw, se$ . In Figure (3.2a) and Figure (3.2b) edge centres and the face centres used in the computation are depicted in two different planes. For computations we need values of the surface area of all the cell faces and the individual volumes of the cells. They are calculated as follows:

### Surface area

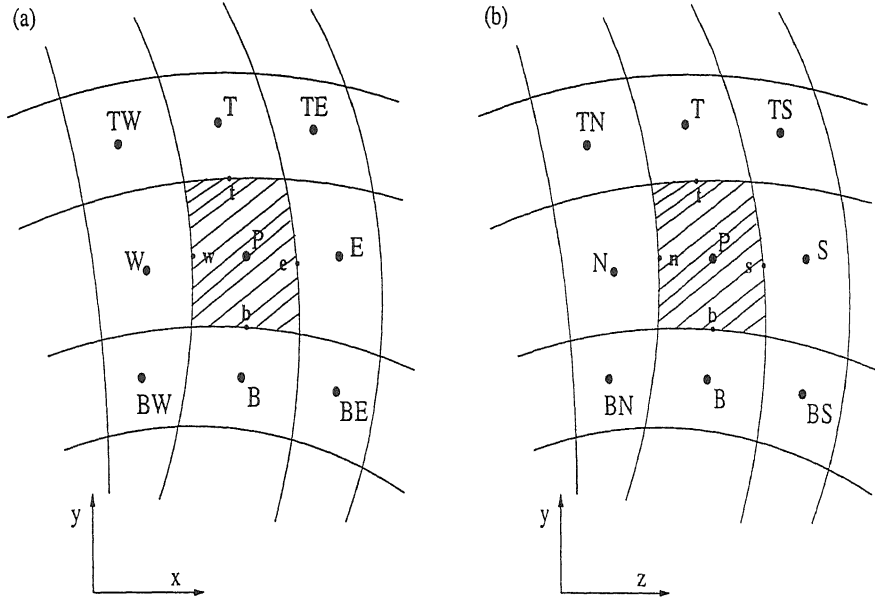


Figure 3.2: A typical finite volume cell (shaded) and its neighbours in the  $x - y$  and  $y - z$  planes.

The finite volume vertices are numbered from 1 to 8 as in the Figure (3.1). The outward normal of a face is calculated by taking the cross product of the diagonal vectors of that face. Diagonal vectors are given by the position vectors of the two opposite vertices in a cell face. If  $\mathbf{r}_i$  and  $\mathbf{r}_j$  are the position vectors of two opposite vertices of a cell face then the diagonal vector is given by

$$\mathbf{r}_{ij} = \mathbf{r}_i - \mathbf{r}_j \quad (3.10)$$

Thus we can calculate the outward surface normal for all the faces of a control volume as follows:

$$\text{West face} \quad \mathbf{S}_w = \frac{1}{2}(\mathbf{r}_{42} \times \mathbf{r}_{31})$$

$$\text{South face} \quad \mathbf{S}_s = \frac{1}{2}(\mathbf{r}_{46} \times \mathbf{r}_{53})$$

$$\text{East face} \quad \mathbf{S}_e = \frac{1}{2}(\mathbf{r}_{57} \times \mathbf{r}_{86})$$

$$\text{North face } \mathbf{S}_n = \frac{1}{2}(\mathbf{r}_{17} \times \mathbf{r}_{28})$$

$$\text{Top face } \mathbf{S}_t = \frac{1}{2}(\mathbf{r}_{62} \times \mathbf{r}_{73})$$

$$\text{Bottom face } \mathbf{S}_b = \frac{1}{2}(\mathbf{r}_{51} \times \mathbf{r}_{48})$$

Volume:

The volume of a cell is calculated from the coordinates of the cell vertices assuming that these vertices are joined by straight lines to form the six faces. It is given by

$$V = \frac{1}{3} \mathbf{r}_{71} \cdot (\mathbf{S}_w + \mathbf{S}_s + \mathbf{S}_b)$$

The grids used for the calculation of the governing equations are shown in Figures (3.3)-(3.5). Three levels of grids are shown. For the reactor geometry with the curved substrate described in Chapter 1, partially converged as well as fully converged results are shown. From Figures (3.4) and (3.5) the issues of orthogonality and attraction-repulsion of the grid lines can be demonstrated as follows. When the elliptic equations for generating orthogonal grids (equations 3.2 and 3.3) in section 3.1 are solved to machine accuracy, grid lines become orthogonal to one another but the attraction near a convex boundary and repulsion near a concave boundary lead to severe non-uniformity of the grids as shown in Figure 3.5. Hence in the present study these equations are solved upto partial convergence and the results are shown in Figure 3.4. This is acceptable in the sense that non-uniformity is not encountered and grid lines are near-orthogonal.

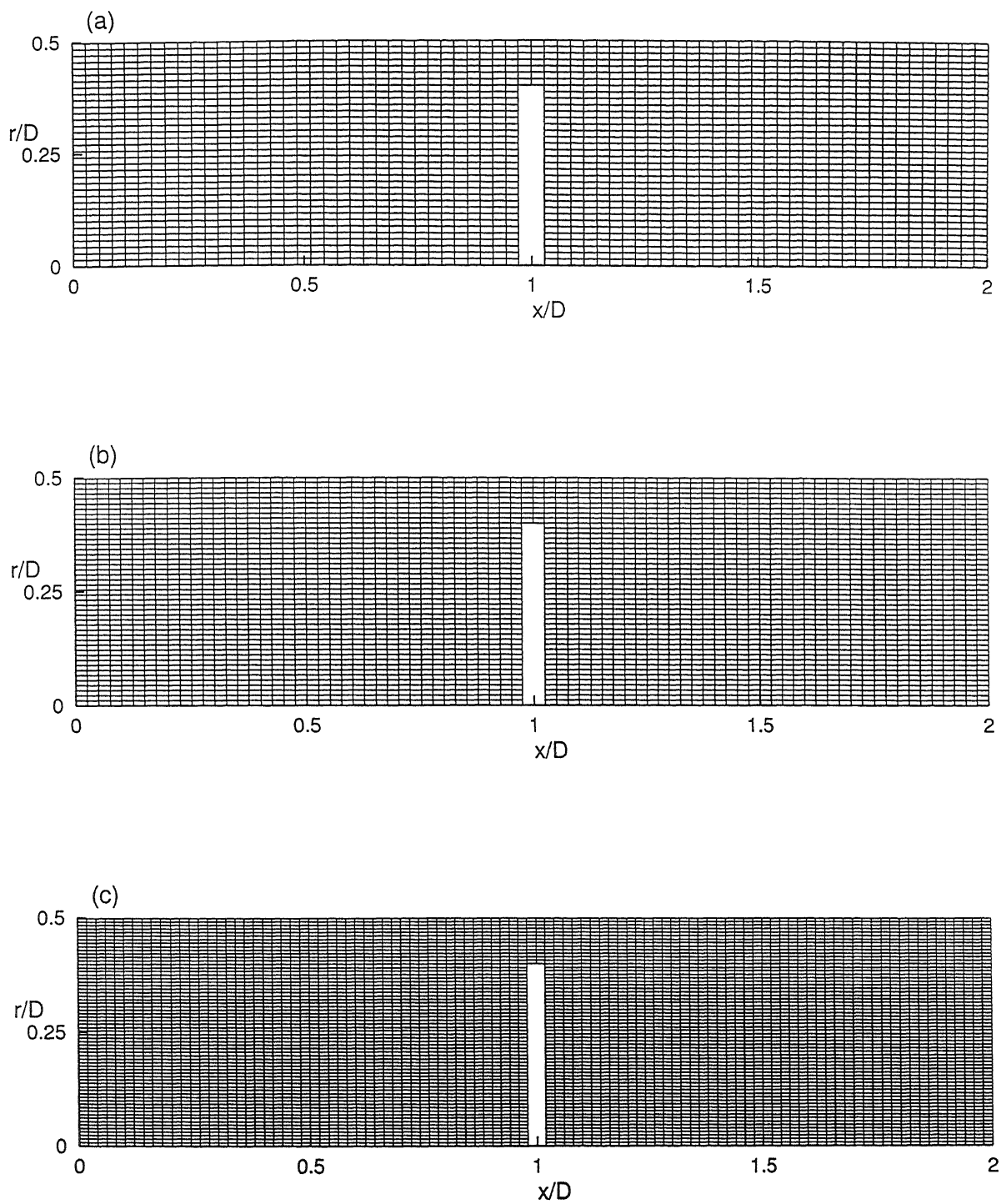


Figure 3.3: Grids used in the calculations for the reactor with plane substrate; (a)  $73 \times 38$ , (b)  $83 \times 48$ , (c)  $103 \times 68$

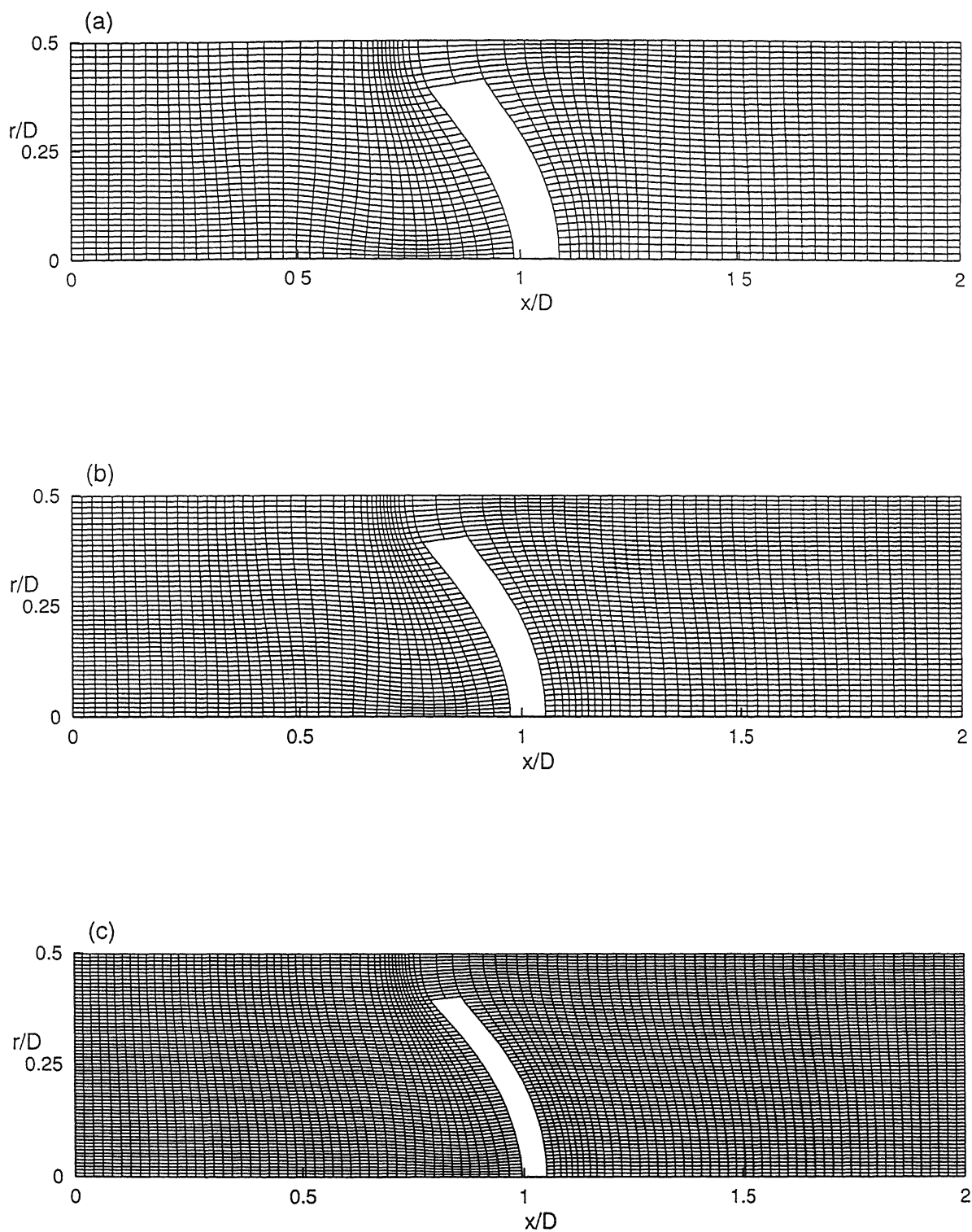


Figure 3.4: Partially converged grids used in the calculations for the reactor with curved substrate; (a)  $73 \times 38$ , (b)  $83 \times 48$ , (c)  $103 \times 68$

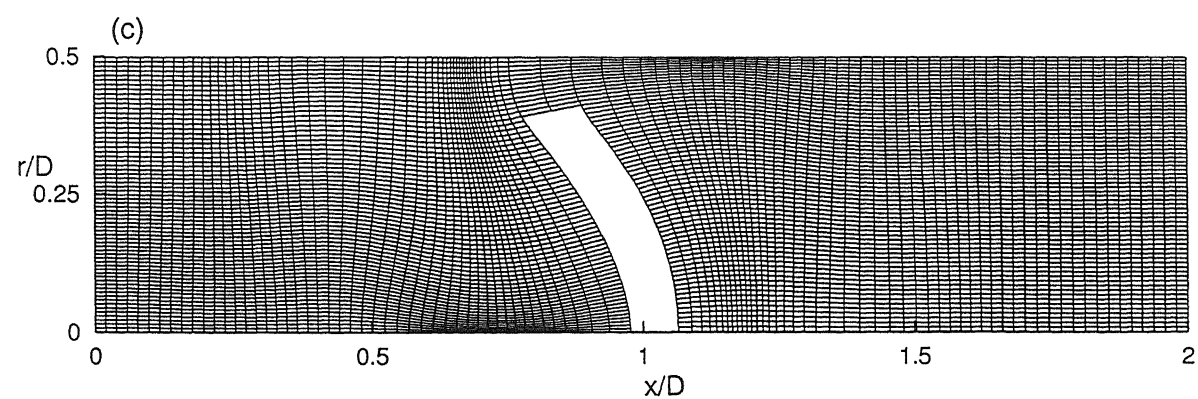
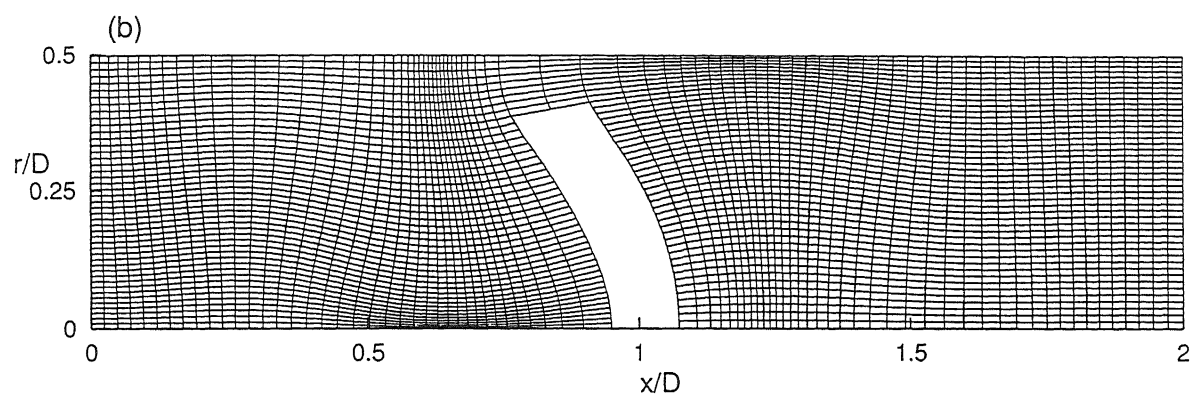
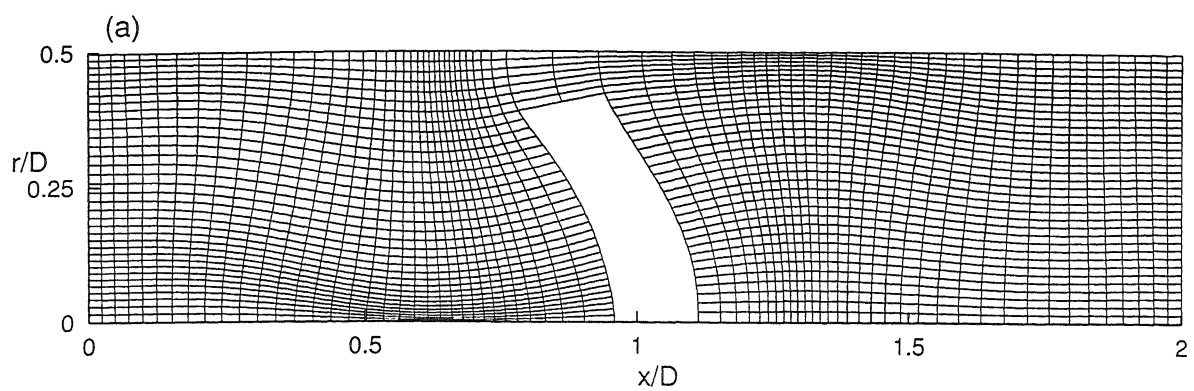


Figure 3.5: Fully converged grids for the reactor with curved substrate; (a)  $73 \times 38$ , (b)  $83 \times 48$ , (c)  $103 \times 68$



### 3.2.3 Discretization Procedure

Here we present the discretization of various integrals that appear in the continuity and momentum equations (3.8, 3.9). The treatment adopted here follows closely the report of Satya Prakash *et al.* (1996).

#### Continuity Equation

The integral form of the continuity equation is given by

$$\int_s \rho \mathbf{u} \cdot d\mathbf{S} \approx \sum_j \rho(\mathbf{u} \cdot \mathbf{S})_j = \sum_j \rho(\mathbf{u}_j \cdot \mathbf{S}_j) = \sum_j F_j \quad (3.11)$$

where  $F_j$  is the mass flux through the face  $j$ , defined by

$$F_j = \rho \mathbf{u}_j \cdot \mathbf{S}_j \quad (3.12)$$

Thus the discretized continuity equation states that total mass flux through all the cell faces vanishes for a finite volume. In turn the net fluid mass in a control volume remains unchanged, a statement of the principle of conservation of mass. The discretized version of the continuity equation is given by

$$\sum_j F_j = F_w + F_s + F_e + F_n + F_t + F_b = 0 \quad (3.13)$$

#### Momentum Equations

The momentum equation when written in the generic advection-diffusion form, consists of four terms; unsteady, convective, diffusive and the source integral related to the pressure gradient. Individually, the discretization of the four terms are performed as follows:

##### Unsteady term

The unsteady term in the governing equation is discretized with the help of the basic assumption that all the dependent variables for which we seek solution are defined at the cell centroid. Thus it follows

$$\frac{\partial}{\partial t} \int_v \rho \phi dV \approx \frac{(\rho \phi V)_P^{n+1} - (\rho \phi V)_P^n}{\Delta t} \approx \rho V_P \frac{\phi_P^{n+1} - \phi_P^n}{\Delta t} \quad (3.14)$$

where  $V_P$  is the volume of a typical control volume and  $\Delta t$  the time increment employed for the time marching. The time discretization of equation (3.14) has an error of first order in time.

### Convective term

The convective integral in the governing equation is approximated as following

$$\int_s \rho \mathbf{u} \phi \cdot d\mathbf{S} \approx \sum_j (\rho \mathbf{u} \cdot \mathbf{S})_j \phi_j = \sum_j F_j \phi_j \quad (3.15)$$

where  $\phi_j$  is the value of the dependent variable at the cell face and  $F_j$  is the mass flux through the face  $j$ . The value of  $\phi$  at the cell face centre is assumed to prevail over the face in question. Thus the discretized equation takes the form

$$\int_s \rho \mathbf{u} \phi \cdot d\mathbf{S} \approx F_w \phi_w + F_s \phi_s + F_e \phi_e + F_n \phi_n + F_t \phi_t + F_b \phi_b \quad (3.16)$$

It is evident from the above expression that for the discretization of the convective flux we need the mass flux at the cell faces. This step requires velocities at the cell faces. It can be shown that if the mass flux at any cell face is calculated using velocities obtained by linear interpolation from the two neighbouring cells adjacent to the face, an arbitrary velocity field with a checker-board distribution may result, a completely nonphysical situation Patankar (1980). The reason for the error is the following: When velocities at a cell face are calculated by linear interpolation between two adjacent cell centre values, the continuity equation becomes the difference between two alternate cell centre velocities and not between adjacent ones. This leads to decoupling of the velocity at the cell for which the continuity equation is discretized and any zig-zag velocity distribution satisfies

the continuity equation. To avoid such velocity wiggles, the momentum interpolation idea has been proposed in the literature. This technique uses pressure weighted interpolation of velocities at the cell faces and uses these velocities to calculate the mass flux at the cell face.

If  $J$  and  $J + 1$  are two neighbouring cells adjacent to a face  $j$ , then the mass flux at the face  $j$  is calculated by velocities obtained by straightforward linear interpolation as

$$F_j = \rho \mathbf{U}_j \cdot \mathbf{S}_j \quad (3.17)$$

where  $\mathbf{U}_j$  is the velocity linearly interpolated from the two adjacent cells to the face  $j$ , written as

$$\mathbf{U}_j = \frac{\mathbf{u}_J V_{J+1} + \mathbf{u}_{J+1} V_J}{V_J + V_{J+1}} \quad (3.18)$$

The momentum interpolation adds a pressure gradient term with the linearly interpolated part of equation (3.17), namely

$$F_j = \rho \mathbf{U}_j \cdot \mathbf{S}_j - \Delta t \nabla p \cdot \mathbf{S}_j \quad (3.19)$$

This technique serves two purposes as a whole. First it excludes the possibility of any velocity wiggles because velocities at a cell face depends on the pressure at the adjoint cell centres which in turn depend on the flux at the cell faces for which continuity equation is discretized. So any abrupt changes in the velocity field can be sensed by the continuity equation and an arbitrary velocity field cannot be permitted as the solution. Secondly the pressure gradient term which takes values from the two adjacent cells ( $J$  and  $J + 1$ ) behaves like a natural force driving the mass flow at the cell face  $j$ , a key point for the success of the staggered grid arrangement.

As the velocities are defined at the cell centroid we have to use an interpolation scheme to obtain velocities at the cell face centre. In the present work this has been accomplished by taking contribution of both second order central difference and first order upwind difference scheme. The central difference scheme can lead to numerical instability and the upwind method introduces numerical diffusion, when they are individually used. Thus using the right combination of these two schemes is expected to improve the robustness of the algorithm. For

strongly nonlinear and convection dominated flows the upwind method maintains the transportive property of the flow, and the central difference scheme being of second order reduces error in the solution. Here we demonstrate the complete form of the two schemes and their joint application in a finite volume code. The central difference method applied to calculate the face centre value of the dependent variable leads to

$$\phi_j = \frac{V_J}{V_J + V_{J+1}}\phi_{J+1} + \frac{V_{J+1}}{V_J + V_{J+1}}\phi_J \quad (3.20)$$

where  $j$  and  $J$  represent the face centre and cell centre values. Here  $J$  and  $J + 1$  are two neighbouring cells adjacent to the face  $j$ . It is to be noted that for uniform grids the above formula is second order accurate but for non-uniform grids this volume weighted formula gives only first order accuracy. The upwind scheme rightly manifests the transportive property of the fluid flow equations in the local flow direction. It introduces numerical diffusion in the solution and hence leads to smearing of a sharp front. This scheme is written as follows:

$$F_j\phi_j = |F_j, 0|\phi_J + |-F_j, 0|\phi_{J+1} \quad (3.21)$$

With this scheme, the dependent variable at the face centre takes the value of the upstream cell if the mass flux is positive and takes the value of downstream cell if the mass flux is negative. The two schemes on combination take the form

$$F_j\phi_j = (|F_j, 0|\phi_J + |-F_j, 0|\phi_{J+1}) + \gamma[F_j(\frac{V_J}{V_J + V_{J+1}}\phi_{J+1} + \frac{V_{J+1}}{V_J + V_{J+1}}\phi_J) - (|F_j, 0|\phi_J + |-F_j, 0|\phi_{J+1})] \quad (3.22)$$

where the factor  $\gamma$  signifies the contribution of each scheme. It varies between 0 and 1; the limit of 0 implies a purely upwind and 1 implies the purely central difference scheme. There is no universal rule to choose this factor in a particular calculation. It depends on the nature of the problem, numerical technique being used and the range of parameters taken into account. In the present study we have used  $\gamma = 0.5$ .

Using equation (3.22) the convective flux at all the cell faces are calculated

as follows

$$F_w \phi_w = (|F_w, 0| \phi_W - | - F_w, 0| \phi_P) + \gamma[F_w(\frac{V_W}{V_W + V_P} \phi_P + \frac{V_P}{V_W + V_P} \phi_W) - (|F_w, 0| \phi_W - | - F_w, 0| \phi_P)]$$

$$F_s \phi_s = (|F_s, 0| \phi_P - | - F_s, 0| \phi_S) + \gamma[F_s(\frac{V_S}{V_S + V_P} \phi_P + \frac{V_P}{V_S + V_P} \phi_S) - (|F_s, 0| \phi_P - | - F_s, 0| \phi_S)]$$

$$F_e \phi_e = (|F_e, 0| \phi_P - | - F_e, 0| \phi_E) + \gamma[F_e(\frac{V_E}{V_E + V_P} \phi_P + \frac{V_P}{V_E + V_P} \phi_E) - (|F_e, 0| \phi_P - | - F_e, 0| \phi_E)]$$

$$F_n \phi_n = (|F_n, 0| \phi_N - | - F_n, 0| \phi_P) + \gamma[F_n(\frac{V_N}{V_N + V_P} \phi_P + \frac{V_P}{V_N + V_P} \phi_N) - (|F_n, 0| \phi_N - | - F_n, 0| \phi_P)]$$

$$F_t \phi_t = (|F_t, 0| \phi_P - | - F_t, 0| \phi_T) + \gamma[F_t(\frac{V_T}{V_T + V_P} \phi_P + \frac{V_P}{V_T + V_P} \phi_T) - (|F_t, 0| \phi_P - | - F_t, 0| \phi_T)]$$

$$F_b \phi_b = (|F_b, 0| \phi_B - | - F_b, 0| \phi_P) + \gamma[F_b(\frac{V_B}{V_B + V_P} \phi_P + \frac{V_P}{V_B + V_P} \phi_B) - (|F_b, 0| \phi_B - | - F_b, 0| \phi_P)]$$

## Diffusion term

The diffusion flux of the variable  $\phi$  in the governing equation can be approximated as

$$\int_s \Gamma_\phi \nabla \phi \cdot d\mathbf{S} \approx \sum_j (\Gamma_\phi \nabla \phi \cdot \mathbf{S})_j = \sum_j F_j^d \quad (3.23)$$

where the superscript  $d$  denotes diffusive flux. Discretization of this term in complex geometries with curvilinear grids is carried out as follows. The diffusion mechanism is considered in the normal and tangential directions with respect to the curvilinear coordinate lines. These are termed normal and cross diffusion. For any face the outward drawn normal vector can be written as the linear combination of three linearly independent unit vectors which are themselves not necessarily orthogonal. Thus

$$\mathbf{S}_j = \alpha_1 \mathbf{n}_1 + \alpha_2 \mathbf{n}_2 + \alpha_3 \mathbf{n}_3 \quad (3.24)$$

where  $\mathbf{n}_1, \mathbf{n}_2, \mathbf{n}_3$  are three linearly independent unit vectors given in terms of their cartesian components as

$$\begin{aligned} \mathbf{n}_1 &= (n_{11} \ n_{12} \ n_{13}) \\ \mathbf{n}_2 &= (n_{21} \ n_{22} \ n_{23}) \\ \mathbf{n}_3 &= (n_{31} \ n_{32} \ n_{33}) \end{aligned}$$

Thus the vector product of equation (3.23) can be written as

$$\begin{aligned} \nabla \phi \cdot \mathbf{S} &= \nabla \phi \cdot (\alpha_1 \mathbf{n}_1 + \alpha_2 \mathbf{n}_2 + \alpha_3 \mathbf{n}_3) \\ &= \alpha_1 \nabla \phi \cdot \mathbf{n}_1 + \alpha_2 \nabla \phi \cdot \mathbf{n}_2 + \alpha_3 \nabla \phi \cdot \mathbf{n}_3 \end{aligned} \quad (3.25)$$

Now if  $\Delta \phi_1, \Delta \phi_2, \Delta \phi_3$  are the differences in  $\phi$  along the three line segments  $\Delta \mathbf{x}_1, \Delta \mathbf{x}_2, \Delta \mathbf{x}_3$  then

$$\Delta \phi_1 = \nabla \phi \cdot \Delta \mathbf{x}_1, \quad \Delta \phi_2 = \nabla \phi \cdot \Delta \mathbf{x}_2, \quad \Delta \phi_3 = \nabla \phi \cdot \Delta \mathbf{x}_3$$

If  $\Delta \mathbf{x}_1, \Delta \mathbf{x}_2, \Delta \mathbf{x}_3$  are in the directions of  $\mathbf{n}_1, \mathbf{n}_2, \mathbf{n}_3$  and  $\Delta x_1, \Delta x_2, \Delta x_3$  are the magnitude of the line segments respectively then

$$\Delta \phi_1 = \nabla \phi \cdot \mathbf{n}_1 \Delta x_1, \quad \Delta \phi_2 = \nabla \phi \cdot \mathbf{n}_2 \Delta x_2, \quad \Delta \phi_3 = \nabla \phi \cdot \mathbf{n}_3 \Delta x_3$$

Thus it follows that

$$\nabla \phi \cdot \mathbf{n}_1 = \frac{\Delta \phi_1}{\Delta x_1}, \quad \nabla \phi \cdot \mathbf{n}_2 = \frac{\Delta \phi_2}{\Delta x_2}, \quad \nabla \phi \cdot \mathbf{n}_3 = \frac{\Delta \phi_3}{\Delta x_3} \quad (3.26)$$

The diffusion flux at the face  $j$  can be written using equations (3.25) and (3.26) as

$$F_j^d = \Gamma_\phi \nabla \phi \cdot \mathbf{S}_j = \Gamma_\phi \left( \alpha_1 \frac{\Delta \phi_1}{\Delta x_1} + \alpha_2 \frac{\Delta \phi_2}{\Delta x_2} + \alpha_3 \frac{\Delta \phi_3}{\Delta x_3} \right) \quad (3.27)$$

Equation (3.24) can be written in matrix form as

$$\begin{bmatrix} n_{11} & n_{21} & n_{31} \\ n_{12} & n_{22} & n_{32} \\ n_{13} & n_{23} & n_{33} \end{bmatrix} \begin{Bmatrix} \alpha_1 \\ \alpha_2 \\ \alpha_3 \end{Bmatrix} = \begin{Bmatrix} S_{1j} \\ S_{2j} \\ S_{3j} \end{Bmatrix}$$

where  $S_{1j}, S_{2j}, S_{3j}$  are the three cartesian components of the outward normal surface vector  $\mathbf{S}_j$ . The coefficient matrix in the above equation can be inverted to get the values of  $\alpha_1, \alpha_2, \alpha_3$ . We have used Cramer's rule to invert the matrix. Hence

$$\alpha_1 = \frac{D_1}{D}, \alpha_2 = \frac{D_2}{D}, \alpha_3 = \frac{D_3}{D} \quad (3.28)$$

where  $D$  is the determinant of the coefficient matrix of the matrix equation. The matrices  $D_1, D_2$  and  $D_3$  are formed by replacing the respective columns of the coefficient matrix by the right hand side vector of the matrix equation.

For a system of linear equations

$$A\mathbf{x} = \mathbf{b}$$

with  $n$  unknowns, if the rank of the coefficient matrix is equal to  $n$  written by

$$\text{rank } A = n$$

then the coefficient matrix  $A$  is non-singular and the linear system has a unique solution Kreyszig (1993). The row vectors of the coefficient matrix of equation (3.24) are linearly independent. Thus the maximum number of linearly independent row vectors are three, resulting in the rank of the matrix to be three. Hence this matrix is non-singular and gives a unique solution for the  $\alpha$ 's.

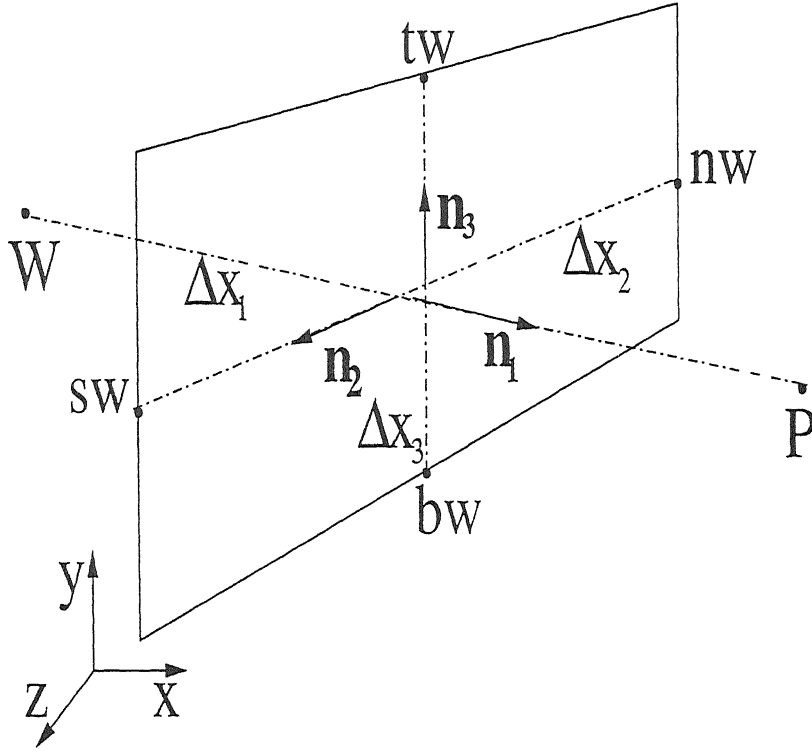


Figure 3.6: Lengths required for the calculation of diffusion fluxes and related nomenclature.

In the discretization of the diffusive flux, the normal and the cross diffusion components have to be accounted for. It can be shown that for orthogonal cartesian grids the cross diffusion term vanishes but for non-uniform curvilinear grids, cross-diffusion in the three directions are possible. In Figure (3.6) the diffusion fluxes and the related terminology are clearly shown.

For the calculation of the cross diffusion fluxes, values of the dependent variables at the edge centres are required. These values have been calculated by the volume weighted interpolation technique using cell centre values of four neighbouring cells surrounding an edge. Values at the four edge centres on the west face are written below:

$$\phi_{tw} = \frac{V_{TW}\phi_P + V_W\phi_T + V_P\phi_{TW} + V_T\phi_W}{V_{TW} + V_W + V_P + V_T}, \phi_{sw} = \frac{V_{SW}\phi_P + V_W\phi_S + V_P\phi_{SW} + V_S\phi_W}{V_{SW} + V_W + V_P + V_S}$$



$$\phi_{bw} = \frac{V_{BW}\phi_P + V_B\phi_W + V_P\phi_{BW} + V_W\phi_B}{V_{BW} + V_B + V_P + V_W}, \phi_{nw} = \frac{V_{NW}\phi_P + V_N\phi_W + V_P\phi_{NW} + V_W\phi_N}{V_{NW} + V_N + V_P + V_W}$$

Calculations for the edge centre values at other faces are similar and straightforward.

### Pressure Gradient term

In the momentum equation, the evaluation of the pressure gradient term is identical to the diffusion term. Its discretized form is written below for the  $i$ th momentum equation after integrating over a typical finite volume.

$$\begin{aligned} \int_v \nabla p \cdot \mathbf{n}_i dV &= \int_v \nabla p \cdot \mathbf{n}_i dV + \int_v p \nabla \cdot \mathbf{n}_i dV \\ &= \int_v \nabla \cdot (p \mathbf{n}_i) dV \\ &= \int_s p \mathbf{n}_i \cdot d\mathbf{S} \\ &= \sum_j p_j \mathbf{n}_i \cdot \mathbf{S}_j \\ &= \sum_j p_j S_{ij} \end{aligned}$$

Thus the discretized form of the pressure flux is given by

$$\int_v \nabla p \cdot \mathbf{n}_i dV = \sum_j p_j S_{ij} \quad (3.29)$$

This term is similar to the diffusion flux of equation (3.23), and can be approximated in an identical manner.

### 3.2.4 Time integration Scheme

The momentum equation is mathematically of mixed character. It can be visualized as elliptic in space and parabolic in time. The momentum equation

has been time integrated semi-explicitly with each term treated explicitly except for the pressure term which is implicitly treated. The time integration scheme mainly consists of two steps. In the first step which is the predictor, velocities are computed based on pressure field at the current time level. In the second, the corrector step, velocities and pressure are corrected iteratively to satisfy the divergence-free condition for the velocity field. The pressure-velocity coupling in the corrector step reduces to a Poisson equation for the pressure correction. This equation has been solved iteratively until the continuity equation is satisfied to the machine accuracy. It should be noted that an explicit formulation does not involve any matrix inversion for the velocity calculations compared to semi implicit type of formulations such as SIMPLE and SIMPLER Patankar (1980). Thus explicit calculations are not computationally intensive. However the explicit formulation suffers from the time step restriction due to its conditionally stable behaviour. On the other hand, very small time step increment can resolve the minute details of the transients. Weak coupling between discrete points in the domain is however inferior compared to an implicit formulation. Although the present study has not been directed towards obtaining the transient details, the points mentioned above justify the choice of the explicit algorithm. The predictor and the corrector steps with the equations to be solved are written below.

## Predictor

In the predictor step, the velocities (marked by \*) are predicted using values from current ( $n$ th) time step:

$$\rho V_P \frac{\mathbf{u}_P^* - \mathbf{u}_P^n}{\Delta t} + \sum_j (F_j^c + F_j^d)^n = - \sum_j p_j^n S_{ij} \quad (3.30)$$

Equation (3.30) leads to the predicted velocities as

$$\mathbf{u}_P^* = \mathbf{u}_P^n - \frac{\Delta t}{\rho V_P} [\sum_j (F_j^c + F_j^d)^n + \sum_j p_j^n S_{ij}] \quad (3.31)$$

## Corrector

By advancing semi-explicitly in time the momentum equation becomes

$$\mathbf{u}_P^{n+1} = \mathbf{u}_P^n - \frac{\Delta t}{\rho V_P} \left[ \sum_j (F_j^c + F_j^d)^n + \sum_j p_j^{n+1} S_{ij} \right] \quad (3.32)$$

By subtracting equation (3.31) from equation (3.32) we get

$$\mathbf{u}'_P = -\frac{\Delta t}{\rho V_P} \sum_j p'_j S_{ij} \quad (3.33)$$

where  $\mathbf{u}'_P$  and  $p'$  are the velocity and pressure corrections to the predicted velocities and guessed pressure. They are defined as

$$\mathbf{u}'_P = \mathbf{u}_P^{n+1} - \mathbf{u}_P^* \quad (3.34)$$

$$p' = p^{n+1} - p^n \quad (3.35)$$

If equation (3.33) is cast into the integral form then a relation between velocity and pressure corrections can be obtained as follows:

$$\begin{aligned} \int_{CV} \mathbf{u}' dV &= -\frac{\Delta t}{\rho} \sum_j p'_j \mathbf{n}_i \cdot \mathbf{S}_j \\ &= -\frac{\Delta t}{\rho} \int_v \nabla \cdot (p' \mathbf{n}_i) dV \\ &= -\frac{\Delta t}{\rho} \left[ \int_v \mathbf{n}_i \cdot \nabla p' dV + \int_v p' \nabla \cdot \mathbf{n}_i dV \right] \\ &= -\frac{\Delta t}{\rho} \int_v \nabla p' dV \end{aligned}$$

with the integration being performed over an arbitrary finite volume. The integrands of each side can be pulled out of the integral to get

$$\mathbf{u}' = -\frac{\Delta t}{\rho} \nabla p' \quad (3.36)$$

In the corrector step we enforce continuity implicitly, written symbolically as

$$\sum_j F_j^{n+1} = 0 \quad (3.37)$$

Writing this term as sum of predicted fluxes based on predicted velocities of the first step and the amount of flux to be corrected to get a divergence free flow field, we get

$$\sum_j F_j^* + \sum_j F'_j = 0 \quad (3.38)$$

This gives

$$\sum_j F_j^* = - \sum_j F'_j \quad (3.39)$$

Thus equations (3.36) and (3.37) constitute the corrector step. These two equations are to be simultaneously solved. It has been accomplished by an iterative technique. The two equations are reduced to a Poisson equation in pressure correction, solved to get a divergence free velocity field.

### Pressure Correction equation

It can be shown the two equations to be solved in the corrector step (equations 3.36 and 3.37) lead to a Poisson equation in pressure correction. The two terms of equation (3.38) when written in integral form lead to

$$\begin{aligned} \sum F_j^* &= \int_s \rho \mathbf{u}^* \cdot d\mathbf{S} \\ &= \rho \int_v \nabla \cdot \mathbf{u}^* dV \end{aligned}$$

and

$$\begin{aligned} - \sum_j F'_j &= - \int_{CS} \rho \mathbf{u}' \cdot d\mathbf{S} \\ &= - \rho \int_{CV} \nabla \cdot \mathbf{u}' dV \\ &= \Delta t \int_{CV} \nabla \cdot (\nabla p') dV \\ &= \Delta t \int_{CV} \nabla^2 p' dV \end{aligned}$$

Thus the integral form of the equation (3.39) is

$$\Delta t \int_v \nabla^2 p' dV = \rho \int_v \nabla \cdot \mathbf{u}^* dV$$

As the integration has been carried out over an arbitrary finite volume, the integrand of each side can be pulled out of the integral to get

$$\nabla^2 p' = \frac{\rho}{\Delta t} \nabla \cdot \mathbf{u}^* \quad (3.40)$$

Hence solving equations (3.36) and (3.37) is equivalent to solving equation (3.40), the Poisson equation in pressure correction. The two equations to be solved simultaneously in the corrector step can also be reduced to a form which is more amenable to the Gauss-Seidel iterative method. This is called the residual form of the pressure correction equation and is developed as follows.

The mass flux correction can be written in terms of pressure correction by using equation (3.36) as

$$\begin{aligned} F'_j &= \rho \mathbf{u}'_j \cdot \mathbf{S}_j \\ &= -\Delta t \nabla p' \cdot \mathbf{S}_j \end{aligned}$$

It follows that

$$\sum_j F'_j = - \sum_j \Delta t \nabla p' \cdot \mathbf{S}_j \quad (3.41)$$

The pressure correction term in the above equation can be discretized in the same way as the diffusion term:

$$\Delta t \sum_j \nabla p' \cdot \mathbf{S}_j = \Delta t \left[ \sum_j (\nabla p' \cdot \mathbf{S}_j)_{nd} + \sum_j (\nabla p' \cdot \mathbf{S}_j)_{cd} \right] \quad (3.42)$$

where the subscript *nd* and *cd* corresponds to normal and cross diffusion terms, explained in the context of the diffusion flux. It is to be noted that the cross diffusion term contains values of pressure correction from both the current as well as the previous iteration levels. The normal diffusion term is discretized in

the same way as the normal diffusion flux. Using equation (3.27) we write

$$\Delta t \sum_j (\nabla p' \cdot \mathbf{S}_j)_{nd} = \Delta t \left[ \frac{\alpha_1}{\Delta x_1} |_w (p'_P - p'_W) + \frac{\alpha_2}{\Delta x_2} |_s (p'_S - p'_P) + \frac{\alpha_1}{\Delta x_1} |_e (p'_E - p'_P) \right. \\ \left. + \frac{\alpha_2}{\Delta x_2} |_n (p'_P - p'_N) + \frac{\alpha_3}{\Delta x_3} |_t (p'_T - p'_P) + \frac{\alpha_3}{\Delta x_3} |_b (p'_P - p'_B) \right]$$

Thus equation (3.42) can be written as

$$\Delta t \sum_j \nabla p' \cdot \mathbf{S}_j = \Delta t \sum_{nb} \frac{\alpha}{\Delta x} |_{nb} p'_{nb} + a_P p'_P + \Delta t T_{cd} \quad (3.43)$$

where  $nb$  denotes all the neighbours of the cell with centroid at  $P$ . The coefficient  $a_P$  is given by

$$a_P = \Delta t \left( \frac{\alpha_1}{\Delta x_1} |_w - \frac{\alpha_2}{\Delta x_2} |_s - \frac{\alpha_1}{\Delta x_1} |_e + \frac{\alpha_2}{\Delta x_2} |_n - \frac{\alpha_3}{\Delta x_3} |_t + \frac{\alpha_3}{\Delta x_3} |_b \right) \quad (3.44)$$

### Residual form of the pressure correction equation

In iterative techniques often it is useful and advantageous to solve the difference equation in residual form Tannehill *et al.* (1997). This is demonstrated below.

Any difference equation for a variable  $\phi_{i,j}$  can be written as the sum of the difference equation of a provisional quantity  $\bar{\phi}_{i,j}$  and an incremental quantity  $\delta\phi_{i,j}$ .

$$L \phi_{i,j} = L \bar{\phi}_{i,j} + L \delta\phi_{i,j} = 0 \quad (3.45)$$

The provisional solution  $\bar{\phi}_{i,j}$  represents a value that might occur at some point in an iterative process. The correction  $\delta\phi_{i,j}$  is the quantity to be added to the provisional to get the full solution. The definition of the correction term may bear a slightly different meaning, depending upon the algorithm and the nature of the problem. These two quantities give the exact numerical solution when combined. The residual  $R$  is defined as the number obtained when the difference equation, written in a form producing zero on the right hand side, is evaluated on the basis of the provisional solution. This is given by

$$R = L \bar{\phi}_{i,j} \quad (3.46)$$

In the corrector step the mass flux at any face  $j$  at the  $(n+1)$ th time step summed over all the faces of a finite volume is written in an operator form as

$$\sum_j F_j^{n+1} = L F_j^{n+1} = 0 \quad (3.47)$$

Using equation (3.45) we get

$$L F_j^{n+1} = L \bar{F}_j + L \delta F_j \quad (3.48)$$

The term,  $\bar{F}_j$ , denotes the provisional flux, namely the quantity at a certain iteration level. The symbol  $\delta F_j$  is the correction term to be added with the provisional solution to reach the exact numerical solution. The provisional quantity can be written in terms of the predicted value at the start of the iteration (which does not change during the iterations) and the quantity that has modified the predicted flux to the provisional one during the iterations already occurred. Hence

$$\begin{aligned} L F_j^{n+1} &= L \bar{F}_j + L \delta F_j \\ &= L F_j^* + L (F'_j)_q + L \delta F_j \end{aligned} \quad (3.49)$$

with  $q$  representing the current iteration level. According to the definition of the residual given by equation (3.46) above, equation (3.49) gives the value of the residual as

$$R = -L F_j^* - L (F'_j)_q \quad (3.50)$$

Thus by equations (3.47), (3.49) and (3.50)

$$\begin{aligned} L \delta F_j &= -L F_j^* - L (F'_j)_q \\ &= R \end{aligned} \quad (3.51)$$

It is to be noted from equation (3.48) that as the provisional solution reaches the exact numerical solution  $R$ , the residual vanishes.

The incremental flux  $\delta F_j$  is the difference between the values at the next iteration level and the current iteration level. Using equation (3.43) this term

can be deduced in terms of pressure corrections at the cell of interest and the neighbouring cells. If pressure corrections at all the neighbouring points are neglected then the incremental flux is given in terms of the pressure correction values at point  $P$  at the current and next iteration levels as follows:

$$L \delta F_j = a_P[(p'_P)_{q+1} - (p'_P)_q] \quad (3.52)$$

It follows from equations (3.51) and (3.52) that

$$\begin{aligned} a_P[(p'_P)_{q+1} - (p'_P)_q] &= -L F_j^* - L (F'_j)_q \\ &= R \end{aligned} \quad (3.53)$$

Equation (3.53) written with the application of a relaxation factor takes the form

$$(p'_P)_{q+1} = (p'_P)_q + \gamma \frac{R}{a_P} \quad (3.54)$$

Equation (3.53) is the residual form of the equations (3.36) and (3.37) to be solved in the corrector step. It can be used to update the pressure correction during the iterations for getting a divergence-free velocity field within a time step

During the derivation of the residual form, pressure correction at all the neighbouring cells have been neglected. However this is just an iterative strategies to obtain corrections and the field solution will enforce continuity of the entire discretized equation (3.39) without neglecting any terms as the full equation is used to compute  $R$ . This is in principle similar to the exclusion of all the neighbouring velocity corrections in the SIMPLE algorithm Patankar (1980). This is justified because with the inclusion of pressure corrections at all the neighbouring cells pressure correction updating expression becomes unmanageable. As a neighbouring cell will bring the influence of its neighbours and its neighbours will bring the influence of their neighbours and so on. The relaxation factor mentioned above is applied to accelerate the rate of convergence of the pressure correction equation. This factor may bear a significant meaning depending upon the nature of the system of linear equations arising from the pressure Poisson equation.

The solution algorithm for the momentum equations is now summarized:



Initial conditions for velocities are given and pressure is guessed for all the points in the domain to start the calculation.

Obtain velocities and the mass flux in the predictor step using the initial condition or values from the previous time step as:

start: 1 For each cell ( $P$ )

$$\mathbf{u}_P^* = \mathbf{u}_P^n - \frac{\Delta t}{\rho V_P} \left[ \sum_j (F_j^c + F_j^d)^n + \sum_j p_j^n S_{ij} \right]$$

close: 1

start: 2 For each face ( $j$ ) of a cell ( $P$ )

$$F_j = \rho \mathbf{U}_j \cdot \mathbf{S}_j - \Delta t \nabla p \cdot \mathbf{S}_j$$

( $\mathbf{U}_j$  is the linearly interpolated velocity at the cell face given by equation 3.18)

close: 2

Boundary conditions for the velocities and pressure are applied.

Initial guessed values for pressure correction are utilized to start the iteration in the corrector step.

start: 3 Start iterations ( $k$ ):

Calculate corrective mass flux  $F_j'$  for all the cell faces, the residual  $R$  at each cell and pressure correction values are updated as

start: 4 For a face ( $j$ ) of a cell ( $P$ )

$$F_j' = -\Delta t \nabla p' \cdot \mathbf{S}_j$$

close: 4

start: 5 For a cell ( $P$ )

$$R = - \sum_j F_j^* - \sum_j F_j'$$

close: 5

start: 6 For a cell ( $P$ )

$$p' \leftarrow p' + \gamma \frac{R}{a_P}$$

close: 6

check for convergence as:

If

$$\sqrt{\frac{\sum R^2}{\text{no. of cells}}} < e$$

(where  $e$  is the prescribed convergence criterion, say  $10^{-6}$  %)

STOP

Else: Continue

close: 3 ( $k$ )

Update velocity and pressure

start: 7 For a cell ( $P$ )

$$\mathbf{u} \leftarrow \mathbf{u} + \mathbf{u}'$$

$$p \leftarrow p + p'$$

close: 7

Repeat the same calculations for each time step till steady state is reached

### 3.2.5 Calculation of the time step

It can be shown by the von Neumann stability analysis that for a three dimensional advection-diffusion equation with an explicit FTCS (Forward in Time and Central in Space) scheme, the numerical error does not get amplified in successive time steps if the following two conditions are satisfied :

#### A. CFL criterion

It states that fluid flow information should not propagate by a distance greater than one cell in a given time step. This is the convective limitation which the numerical algorithm should obey to be stable. It is written as

$$\Delta t \left( \frac{u}{\Delta x} + \frac{v}{\Delta y} + \frac{w}{\Delta z} \right) \leq 1 \quad (3.55)$$

Here  $u, v$  and  $w$  are the three components of velocity along the three cartesian directions  $x, y, z$  respectively. If we write this criterion in terms of nondimensional variables it remains unchanged with the nondimensional quantities replacing the dimensional quantities.

## B. Grid Fourier number criterion

Fourier numbers based on individual grid size should not exceed a certain value for the numerical scheme to be stable. This criterion is written as:

$$\nu \Delta t \left( \frac{1}{\Delta x^2} + \frac{1}{\Delta y^2} + \frac{1}{\Delta z^2} \right) \leq \frac{1}{3}$$

with the variables as stated above. If this criterion is written in terms of the nondimensional variables it takes the form

$$\frac{\Delta t}{\text{Re}} \left( \frac{1}{\Delta x^2} + \frac{1}{\Delta y^2} + \frac{1}{\Delta z^2} \right) \leq \frac{1}{3} \quad (3.56)$$

More generally, the kinematic viscosity  $\nu$  is replaced by the diffusivity (thermal or mass) and  $\text{Re}$  by  $\text{Pe}$ , the Peclet number. The above two criteria leads to a single expression as

$$\Delta t \leq \frac{2}{\left( \frac{u}{\Delta x} + \frac{v}{\Delta y} + \frac{w}{\Delta z} \right) + \frac{3}{\text{Re}} \left( \frac{1}{\Delta x^2} + \frac{1}{\Delta y^2} + \frac{1}{\Delta z^2} \right)} \quad (3.57)$$

For calculations over non-uniform grids where cell lengths in the three directions vary through out the domain, dimensions depicted in the above criteria have to be calculated by including all the cells. In the present study we have calculated the minimum of the six diffusion lengths for the six faces along a cartesian direction and then obtained the minimum for that cell. The minimum of the diffusion lengths for a cell is then calculated by comparing the lengths of all the faces. Finally the minimum of the diffusion lengths for the whole domain is calculated. Similar calculations are carried out for the other two cartesian directions. These three lengths have been taken as the dimensions that dictate the propagation of information in the flow domain. The following expression for calculating the

time step has been used after obtaining the appropriate lengths that govern wave propagation.

$$\Delta t = \omega \frac{1}{\left(\frac{u}{\Delta x} + \frac{v}{\Delta y} + \frac{w}{\Delta z}\right) + \frac{3}{\text{Re}}\left(\frac{1}{\Delta x^2} + \frac{1}{\Delta y^2} + \frac{1}{\Delta z^2}\right)} \quad (3.58)$$

Here  $\omega$  ( $< 1$ ), is a factor that makes the time step more conservative than what is demanded by the stability limit. It has been observed that the above expression works well for all Reynolds numbers for stability factors of the order of  $\omega = 0.9$ .

### 3.2.6 Initial and Boundary conditions

As our aim is to obtain a steady state, we can start with an arbitrary initial condition. However to obtain a meaningful transient variation, initial condition should be carefully selected in accordance with the physical situation.

As all the dependent variables are defined at the cell centres and the boundaries lie on the cell faces, a fictitious layer of cells adjacent to each boundary segment have been employed in order to apply the boundary conditions. By interpolating values between a fictitious cell and a real cell adjacent to a boundary the values at the corresponding boundary can be calculated. It is important to note that if the fictitious layer of cells are perfect images of the real cells adjacent to the physical boundary, the boundary conditions are exactly satisfied. Due to the curvilinear non-uniform grids in the present study volume-weighted interpolation has been used to set all the boundary conditions. Boundary conditions applicable to all the boundaries have been discussed in Chapter 2, and will not be repeated here. Only the boundaries where special treatment is required are discussed below.

#### Corner cell treatment

The two corner cells of the solid obstacle are different from the rest of the boundaries in the sense that they have more than one face exposed to the fluid flow. In the present work we have set no mass penetration conditions at these faces. This condition is outlined for one cell as in Figure 3.7

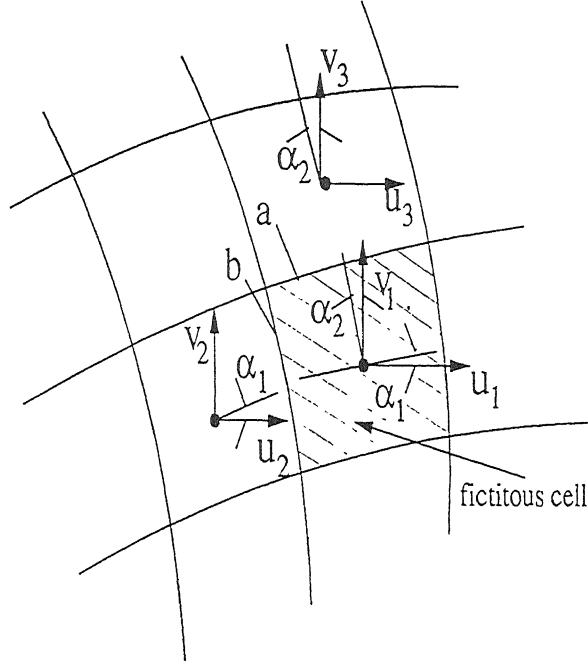


Figure 3.7: One of the corner cells (shaded) and associated velocities.

The normal velocity at the face  $b$  is calculated by using volume weighted interpolation of velocities between the cells 1 and 2. Setting this velocity equals to zero leads to

$$u_1 \cos \alpha_1 + v_1 \sin \alpha_1 = -\frac{V_1}{V_2}(u_2 \cos \alpha_1 + v_2 \sin \alpha_1)$$

In the same way normal velocity at the face  $a$  can be calculated and when this is set to zero we get the following relation

$$-u_1 \sin \alpha_2 + v_1 \cos \alpha_2 = -\frac{V_1}{V_3}(-u_3 \sin \alpha_2 + v_3 \cos \alpha_2)$$

Solving the above two equations for  $u_1$  and  $v_1$  we get the expressions for the velocities at the corner fictitious cells as

$$u_1 = \frac{-\frac{V_1}{V_3}(u_3 \sin \alpha_1 \sin \alpha_2 - v_3 \sin \alpha_1 \cos \alpha_2) - \frac{V_1}{V_2}(u_2 \cos \alpha_1 \cos \alpha_2 + v_2 \sin \alpha_1 \cos \alpha_2)}{\cos(\alpha_1 - \alpha_2)} \quad (3.59)$$

$$v_1 = \frac{\frac{V_1}{V_3}(u_3 \cos \alpha_1 \sin \alpha_2 - v_3 \cos \alpha_1 \cos \alpha_2) - \frac{V_1}{V_2}(u_2 \cos \alpha_1 \sin \alpha_2 + v_2 \sin \alpha_1 \sin \alpha_2)}{\cos(\alpha_1 - \alpha_2)} \quad (3.60)$$

### Periodicity boundary conditions

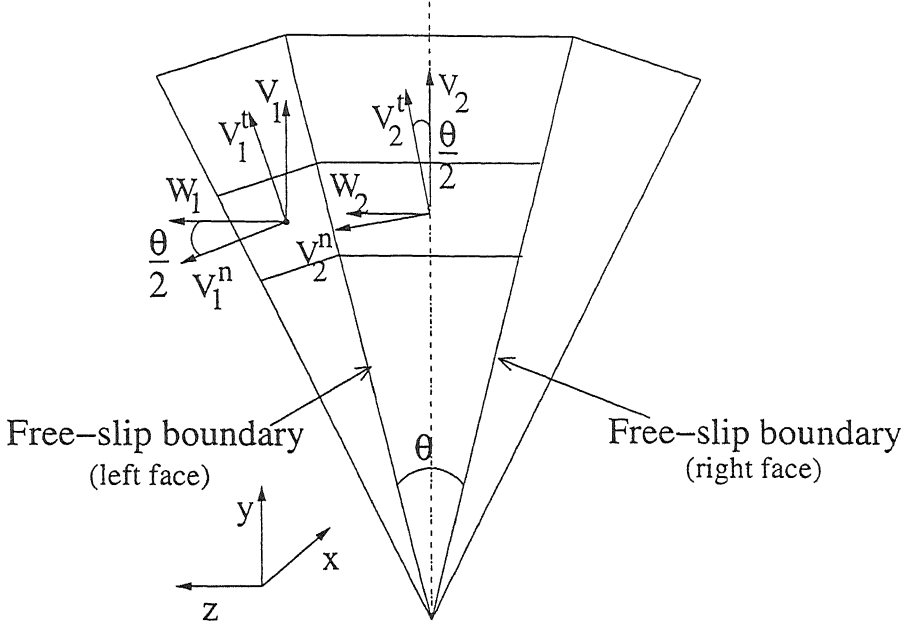


Figure 3.8: Velocities associated with the free-slip boundary condition in the azimuthal direction.

As the computational algorithm of the present work has been generated for the solution of a three dimensional advection-diffusion equation, special treatment is required to make it applicable for a two dimensional geometry. In the present study the free-slip boundary condition has been applied in the third azimuthal direction. This condition states that the normal velocity and normal gradient of all other variables including the tangential velocities should vanish. Implementation of this condition is demonstrated with the help of Figure 3.8 for the left face.

Normal and tangential velocities are calculated for both the real and fictitious cells using the discretized azimuthal angle  $\theta$  per cell as

$$V_1^n = -V_1 \sin \frac{\theta}{2} + W_1 \cos \frac{\theta}{2}$$

$$V_2^n = -V_2 \sin \frac{\theta}{2} + W_2 \cos \frac{\theta}{2}$$

$$V_1^t = V_1 \cos \frac{\theta}{2} + W_1 \sin \frac{\theta}{2}$$

$$V_2^t = V_2 \cos \frac{\theta}{2} + W_2 \sin \frac{\theta}{2}$$

Using these velocities the normal component of velocity and the normal gradient of the tangential velocities can be calculated. Setting these two quantities equal to zero, the boundary conditions for the velocities can be obtained as follows:

$$V_1 = V_2 \cos \theta + W_2 \sin \theta \quad (3.61)$$

$$W_1 = V_2 \sin \theta - W_2 \cos \theta \quad (3.62)$$

As the axial and azimuthal directions are orthogonal to each other, boundary conditions for the axial direction are straightforward in the sense that the axial component of velocities can be directly used. Boundary conditions for the right face in Figure 3.8 can be similarly obtained.

### 3.3 Solution of species transport equations

In Chapter 2 on mathematical formulation of the species transport equations, both dimensional and nondimensional forms were presented. These equa-

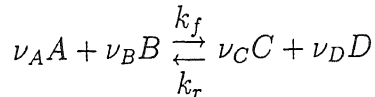
tions use the mass-averaged velocity obtained by solving the Navier Stokes equations. The equations governing the momentum transport and the species transport mechanism form an uncoupled system when their respective time scales are widely separated. The steady state solutions obtained from the momentum equations can then be directly used for solving the species transport equations. For the sake of illustration the discretization of the transport equation for species A is written here in nondimensional form.

$$\frac{\partial}{\partial t}(\rho\omega_A) + \nabla \cdot [(\rho\mathbf{u}\omega_A) - \frac{1}{\text{Pe}_m} \frac{D_{A,o}}{D_{A,o}} \nabla(\rho\omega_A)] = R_A \quad (3.63)$$

where

$$R_A = \nu_A \frac{d}{U_c} \omega_{A,o} \frac{\rho_c}{M_c} \frac{M_A}{M_c} (k_r \omega_C \omega_D - k_f \omega_A \omega_B) \quad (3.64)$$

is the rate of consumption of species A due to a homogeneous elementary chemical reaction of the form



Equation (3.63) is similar to the momentum equation with the exception of the source term  $R_A$ . The source term is appreciable and important since it signifies the consumption of species A. The individual terms in equation (3.63) are discretized in the same fashion as the momentum equations in an advection-diffusion framework. The discretization of the source term requires special treatment and is further discussed. It can be seen from the set of species transport equations (2.33-2.36) that they are coupled with each other by virtue of the source term. Moreover the source term is nonlinear and has to be linearized in order to generate a set of linear algebraic equations.

### 3.3.1 Source term linearization

To develop a numerical algorithm that has a traditional structure, the linearization of the source term is essential Patankar (1980). This can be accomplished as follows. The source term can be approximated as being linearly dependent on the concentration, over a limited range of values. It is self-evident that it



is better to assign the source term to be linearly varying rather than a constant. This linearization formula can be written as

$$R = R_C + R_P \phi_P \quad (3.65)$$

where  $\phi_P$  is the dependent variable of interest (for example, mass fraction of the one of species),  $R_C$  and  $R_P$  are the curve-fitting coefficients of the linearization step. It is required that  $R_P$  is negative. The negative-slope dependence of the source term on  $\phi_P$  is illustrated by the following simple analogy. If in a system there is a volumetric heat source, there should be a proper heat removal mechanism. Otherwise the system will experience an indefinite increase in temperature. Moreover, with the positive slope variation the coefficient of the dependent variable in the algebraic equation may become negative. This is conceptually not acceptable when iterative schemes of matrix inversion are employed Patankar (1980). A negative-slope linearization ensures that instabilities and unrealistic physical solutions do not arise. In the present work, the linearization is obtained by calculating  $R_C$  and  $R_P$  from the previous time step values. The full source term for species  $A$  in linearized form is written below:

$$\begin{aligned} R_A &= \nu_A \frac{d}{U_c} \omega_{A,o} \frac{\rho_c}{M_c} \frac{M_A}{M_c} (k_r \omega_C \omega_D - k_f \omega_A \omega_B) \\ &= R_C - R_P \omega_A \end{aligned} \quad (3.66)$$

where

$$R_C = \nu_A \frac{d}{U_c} \omega_{A,o} \frac{\rho_c}{M_c} \frac{M_A}{M_c} k_r \omega_C \omega_D, \quad R_P = \nu_A \frac{d}{U_c} \omega_{A,o} \frac{\rho_c}{M_c} \frac{M_A}{M_c} k_f \omega_B$$

While discretizing the species transport equations, convective and diffusive fluxes are calculated explicitly and the time marching procedure is used to reach the steady state solution. The discretized equation is written as:

$$\rho V_P \frac{(\omega_i)_P^{n+1} - (\omega_i)_P^n}{\Delta t} = -[\sum_j (F_j^c)^n + \sum_j (F_j^d)^n] + R_C^n - R_P^n (\omega_i)_P^{n+1} \quad (3.67)$$

where  $i$  denotes all the four species. The linearization coefficients are summarized below for all the four species transport equations:

species A

$$R_C = \nu_A \frac{d}{U_c} \omega_{A,o} \frac{\rho_c}{M_c} \frac{M_A}{M_c} k_r \omega_C \omega_D, \quad R_P = \nu_A \frac{d}{U_c} \omega_{A,o} \frac{\rho_c}{M_c} \frac{M_A}{M_c} k_f \omega_B$$

species B

$$R_C = \nu_B \frac{d}{U_c} \omega_{A,o} \frac{\rho_c}{M_c} \frac{M_B}{M_c} k_r \omega_C \omega_D, \quad R_P = \nu_B \frac{d}{U_c} \omega_{A,o} \frac{\rho_c}{M_c} \frac{M_B}{M_c} k_f \omega_A$$

species C

$$R_C = \nu_C \frac{d}{U_c} \omega_{A,o} \frac{\rho_c}{M_c} \frac{M_C}{M_c} k_f \omega_A \omega_B, \quad R_P = \nu_C \frac{d}{U_c} \omega_{A,o} \frac{\rho_c}{M_c} \frac{M_C}{M_c} k_r \omega_D$$

species D

$$R_C = \nu_D \frac{d}{U_c} \omega_{A,o} \frac{\rho_c}{M_c} \frac{M_D}{M_c} k_f \omega_A \omega_B, \quad R_P = \nu_D \frac{d}{U_c} \omega_{A,o} \frac{\rho_c}{M_c} \frac{M_D}{M_c} k_r \omega_C$$

It is clear from the above expressions that the slope of the linearization formula is negative for the reactant species since  $k_f$  denoting forward reaction rate constant is positive for the conventions used in Chapter 2 but is zero for the product species for an irreversible reaction ( $k_r = 0$ ).

### 3.3.2 Operator Splitting algorithm

The chemical reaction we have dealt with is spontaneous and the forward reaction rate constant is quite large in magnitude. In the species transport equations the source term linearly depends on this large constant. With Peclet numbers associated with mass transfer being large as well ( $\gg 1$ ) large value of the source term leads to numerical difficulties during matrix inversion.

Though it has not been the target of the present study to resolve the reaction front moving towards the substrate, the mass transfer problem has been solved by the application of the *Operator Splitting* (OS) algorithm Cooke (1986), Ding and Liu (1989), Muralidhar *et al.* (1993). This technique is well-established to give accurate and detailed results when applied to moving front problems. While

most of the commonly used algorithms fail to explore the sharp variation of a variable in the high Peclet number region, the OS algorithm does not smear the fronts and estimates the transport of the front quite accurately. The basic essence of this algorithm is to split the governing advection-diffusion-reaction equations into two or three equations, one for advection, one for the diffusion and one for the reaction part and solve each of the the homogeneous part of the equation as accurately as possible. Thus the full equation which is difficult to solve in the presence of a large source term is split into parts which are partially solvable preferably by an analytical technique. Hence the splitting procedure not only reduces the computational effort but also ensures successful numerical simulation in the presence of high Peclet numbers and large source terms. In the present study the governing transport equations for each of the species are split into two parts as follows:

$$\frac{\partial}{\partial t}(\rho\omega_i) + \nabla \cdot [(\rho\mathbf{u}\omega_i) - \frac{1}{\text{Pe}_m} \frac{D_{i,o}}{D_{A,o}} \nabla(\rho\omega_i)] = 0 \quad \text{over a time step } \Delta t \quad (3.68)$$

$$\frac{\partial}{\partial t}(\rho\omega_i) = R_i \quad \text{over the time step } \Delta t \quad (3.69)$$

These two equations can also be termed as the predictor (equation 3.68) and corrector (equation 3.69) steps. The predictor step involves solving an advection-diffusion equation without any source term by marching in time, subject to all the boundary conditions for the multidimensional problem. The corrector step is solved with the initial condition derived from equation 3.68. It has a closed form analytical solution. The numerical treatment of the two steps are outlined below.

The predictor step is solved by the finite volume method outlined in section 3.2. After integrating it in an arbitrarily finite volume and approximating various integrals as in the momentum equations we get :

$$\rho V_P \frac{(\omega_i)_P^{n+1} - (\omega_i)_P^n}{\Delta t} = -[\sum_j (F_j^c)^n + \sum_j (F_j^d)^n]$$

The time advanced value of concentration is now obtained as

$$(\omega_i)_P^{n+1} = (\omega_i)_P^n - \frac{\Delta t}{\rho V_P} [\sum_j (F_j^c)^n + \sum_j (F_j^d)^n] \quad (3.70)$$

For the corrector step equation (3.65) is inserted into equation (3.69). By integrating equation (3.69) we get the analytical expression for the mass fraction at  $(n + 1)$ th time level

$$(\omega_i)_P^{n+1} = A_1 - A_2 \exp(-R_P \Delta t) \quad (3.71)$$

where  $A_1$  and  $A_2$  are given by

$$A_1 = \frac{R_C}{R_P} - (\omega_i)_P^n, \quad A_2 = \frac{R_C}{R_P} \quad (3.72)$$

The coefficients  $R_C$  and  $R_P$  are given by the linearization expression for each of the species.

The operator-splitting algorithm for equations (3.68) and (3.69) can be summarized as follows:

Give initial conditions for all the species in the domain to start calculation

Obtain values of mass fraction by solving the predictor step as:

start: 1 For a cell ( $P$ )

$$(\omega_i)_P = (\omega_i)_P^n - \frac{\Delta t}{\rho V_P} \left[ \sum_j (F_j^c)^n + \sum_j (F_j^d)^n \right]$$

close: 1

Obtain values of mass fraction by solving the corrector step using values from the predictor step as the initial condition as:

start: 2 For a cell ( $P$ )

$$(\omega_i)_P^{n+1} = A_1 - A_2 \exp(-R_P \Delta t)$$

( $A_1$  and  $A_2$  are given by equation (3.72) and expressions for  $R_C$  and  $R_P$  are given in section 3.3.1)

close: 2

Apply the boundary conditions.

Repeat the calculations till steady state is reached.

The solution from the OS algorithm was tested directly against that from

the finite volume code applied to the complete system of mass transfer equations. It was found that:

1. The transient details from the two approaches follow each other very closely and the steady state distribution of species are practically identical.
2. Computational time required is lower for the reaction-split approach by a factor of 1.8.
3. With the forward reaction rate parameter  $k_f$  becoming large it is difficult to handle all the terms of the species transport together. specifically, the finite volume code diverged for  $k_f > 10^5$ . The application of the operator splitting algorithm allowed larger source terms upto  $k_f = 10^8$ . In view of these advantages the final results of the present work for mass transfer have been obtained by the OS algorithm.

### 3.3.3 Initial and Boundary conditions

As the present study was targeted towards getting only the steady state solution, constant values have been assigned to all the mass fractions as the initial condition. It has been seen that when converged solution of a particular case is used as the initial condition for an another case whose parameters does not vary significantly convergence is quite faster. All the boundary conditions to be applied for complete solution of the species transport equations have been discussed in Chapter 2. Only the boundary condition at the deposition surface is discussed here.

The mathematical models which consider the surface reactions, derive the boundary condition at the deposition surface by equating net diffusion flux at the surface to the rate of reaction at the surface Mahajan (1996). But for the present model which considers the deposition surface to be inert the specification of boundary condition at the deposition surface is not straight-forward. The above mentioned condition reduces to a no-diffusion condition for a passive surface. The no-diffusion condition does not pose any problem for all the species other than

the species to be deposited. However if this condition is also specified for the depositing species there is no obvious and consistent method for the calculation of deposition rate at the solid surface.

Thus a new homogeneous Dirichlet boundary condition at the deposition surface has been applied to the product species. This boundary condition is consistent with the method of calculation of the deposition rate which directly uses the diffusion mass flux of the product species at the susceptor surface. In the present study product species has been specified as zero at the deposition surface with the view that prediction of diffusion flux at the susceptor surface will serve as an upper limit to the actual deposition. The reason for this is that when a non-negative scalar variable is made to zero at a boundary, the gradient of the variable will be maximum. This can be seen in analogy to convective heat transfer, where the heat transfer at a surface is maximum when the surface is at its coldest possible temperature.

However, the boundary condition at the substrate surface for all the other (reactants) species is just the homogeneous Neumann (no flux) condition.

### 3.4 Grid Independence Test

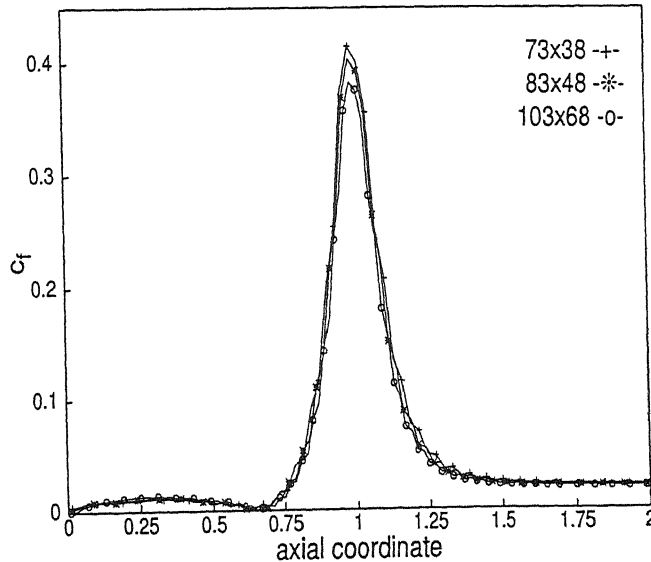


Figure 3.9: Nondimensional shear stress distribution on the reactor wall for the geometry with flat substrate.

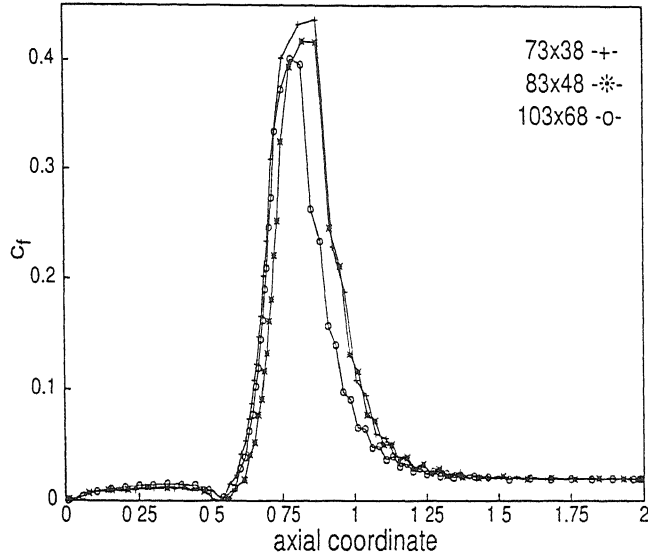


Figure 3.10: Nondimensional shear stress distribution on the reactor wall for a curved substrate.

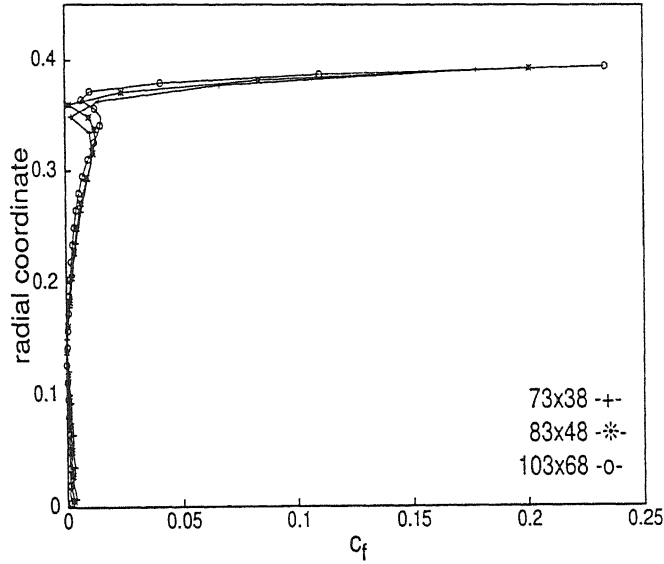


Figure 3.11: Nondimensional shear stress distribution on the substrate surface for a flat substrate.

A grid independence test has been carried out in the present study to investigate the effect of the grid size on the computed results. The case discussed here is the baseline configuration of  $Re = 100$ , velocity ratio of the jets  $V_r = 2$ , angle of the peripheral jet  $\alpha = 30^\circ$ , block position  $Z_b = 1$ . Three grid levels namely,  $73 \times 38$ ,  $83 \times 48$  and  $103 \times 68$  have been studied. Comparative results are presented in terms of velocity vectors and shear stress distribution on the

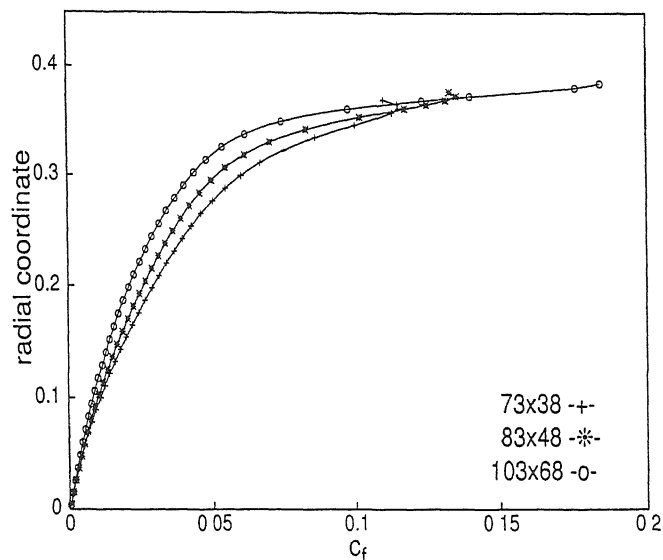


Figure 3.12: Nondimensional shear stress distribution on the reactor wall for a curved substrate.

substrate surface and the reactor wall.

Figures 3.9 and 3.10 show the shear stress distribution on the reactor wall for the flat and concave substrates. Results for the three grids are quite similar in nature for the flat substrate on all the three levels. A slight difference can be seen for the curved substrate. Perhaps this is due to the nonuniformity of the grid lines and the grid spacing in the annular region between the tip of the substrate and the reactor wall. For the three grid levels the peak of the shear stress distribution is not at the same axial location in Figure 3.10. The difference is not due to grid convergence, but arises from the change in the position of the substrate with the number of cells employed in the computation.

Radial shear stress profiles on the substrate surface have been shown in Figures 3.11 and 3.12. For the flat substrate, results compare well with each other while there are differences for the concave substrate. As grids are refined, a greater amount of information is revealed and the stagnation zone attached to the substrate surface is well-resolved. This explains the slightly lower estimation of the shear stress on a fine grid.

The mass transfer code has also been tested for grid independence. Three levels of grids have been used for testing the deposition rate of ZnS on the substrate surface. The results shown in Figure 4.13 match closely with each other



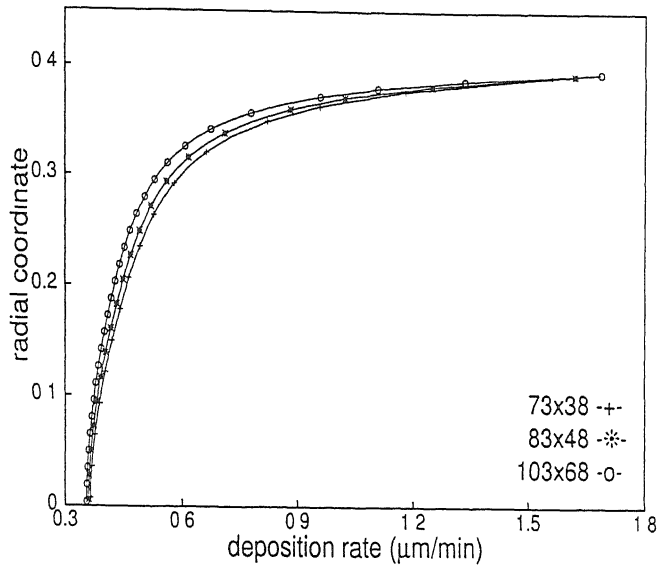


Figure 3.13: Radial variation of deposition rate on the solid surface for a flat substrate.

on all grids.

Figure 3.14 shows the velocity vectors for the three levels of grids. The outermost streamline of the recirculation zone has been superimposed in the figures. These figures show that results from the three levels of grid are quite similar to each other. The position and size of the recirculation patterns are also the same. Figure 3.15 shows the contours of the consumption rates of zinc and the mass fractions of zinc sulphide. Only the significant contours are shown to maintain the clarity of the figures. The results are practically identical. Only the region rich in zinc sulphide becomes slightly larger for fine grid.

It was seen that with an increase in the number of finite volumes, the computational time increased approximately as the cube of the number of cells employed for the calculations. Thus with a grid level as high as  $103 \times 68$ , the economy and accuracy of the calculations could not be simultaneously maintained. Due to the requirement of a severe computational effort, no attempt was made to generate results on a finer grid. Considering the accuracy achieved and the computational time involved a moderate grid level of  $83 \times 48$  has been adopted as the basis of all subsequent calculations. On the  $83 \times 48$  grid, a flow calculation took twenty hours of CPU time; a mass transfer calculation took thirty hours of CPU time. A Pentium III, 766 MHz and 512 MB RAM PC was used for all the calculations.

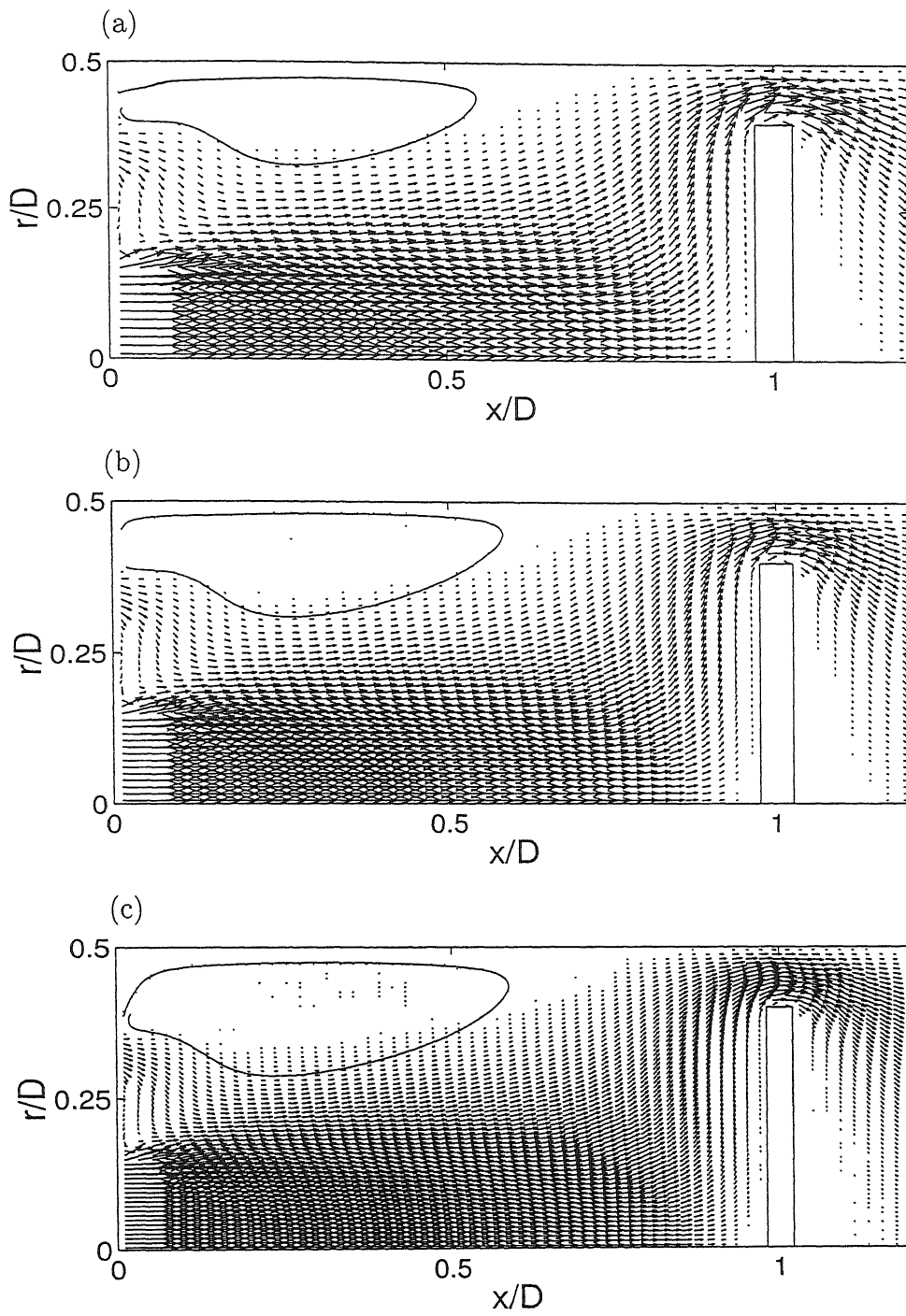


Figure 3.14: Velocity vectors for the reactor with a flat substrate, (a)  $73 \times 38$ , (b)  $83 \times 48$ , (c)  $103 \times 68$ ; Configuration  $Re = 100$ ,  $V_r = 5$ ,  $r_b = 0.8$ ,  $Z_b = 1$ ,  $\alpha = 30^\circ$

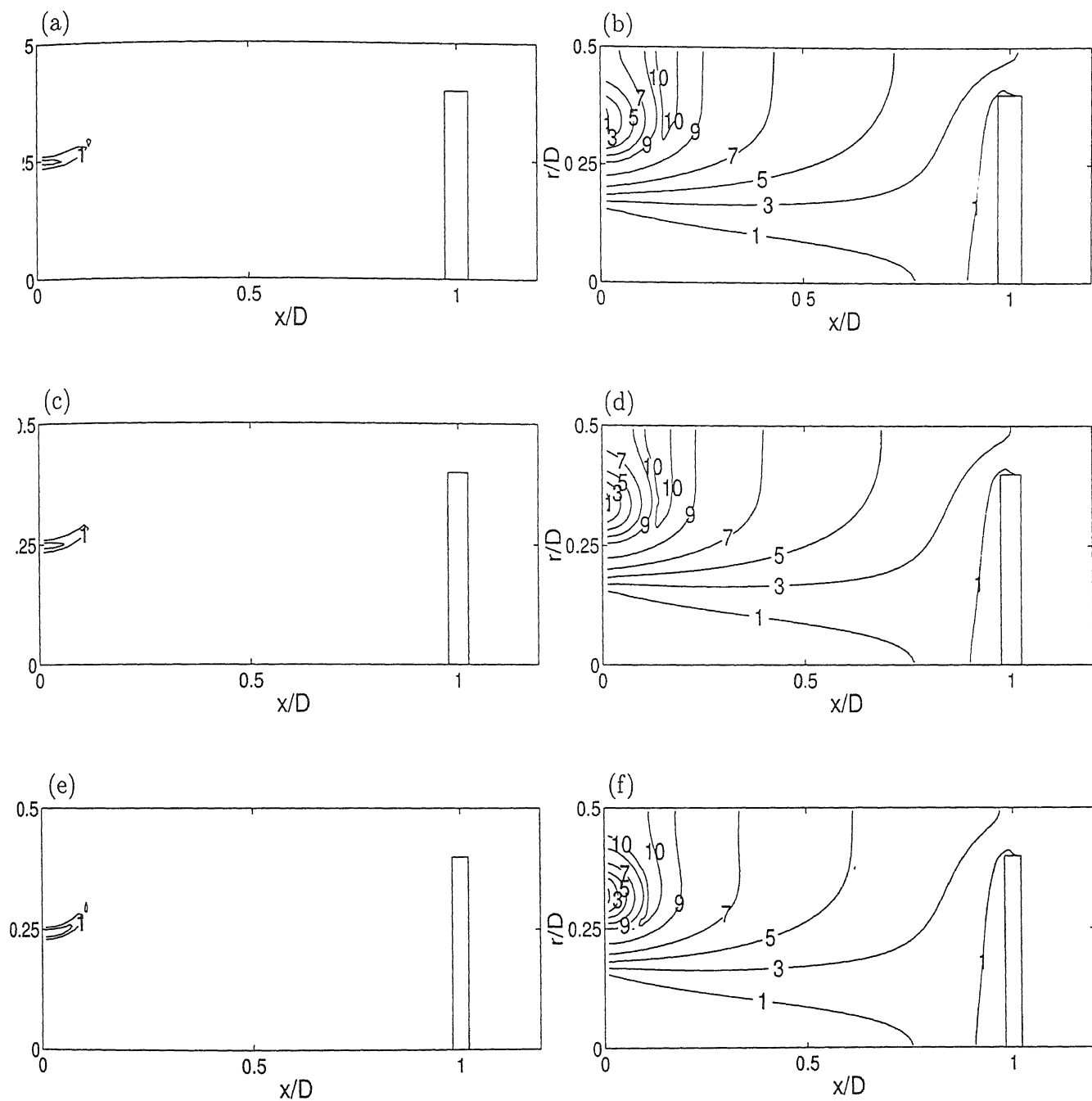


Figure 3.15: steady state contours of consumption rate of Zn (a)  $73 \times 38$ , (c)  $83 \times 48$ , (e)  $103 \times 68$ ; steady state contours of ZnS mass fractions (b)  $73 \times 38$ , (d)  $83 \times 48$ , (f)  $103 \times 68$ ; configuration:  $Re=100$ ,  $V_r = 5$ ,  $r_b = 0.8$ ,  $\alpha = 30^\circ$ ,  $Z_b = 1$

# Chapter 4

## Results and Discussion

Results for fluid flow and mass transfer in the CVD reactor are presented in this Chapter. In the first section results for the flow and concentration fields are presented. The flow field is shown by velocity vectors; significant streamlines are superimposed to identify the recirculation pattern, specifically its size, strength and location. Contours of the steady state consumption rate of zinc and the steady state production rate of zinc sulphide have been shown to get an idea of the reaction zone. The mass fraction contours of zinc and zinc sulphide have also been shown on a per unit mass of the carrier gas basis. In the following section, the deposition rate of zinc sulphide along with the shear stress on the substrate are discussed. Flat and curved substrate shapes have been individually considered.

### 4.1 Flow and concentration fields

#### 4.1.1 Reactor with a flat substrate

Figure 4.1(a) shows the flow field for the baseline case ( $Re = 100, V_r = 2, r_b = 0.8, Z_b = 1$ ). At the Reynolds number studied, the central jet reaches the substrate surface. The peripheral jet is weak and cannot penetrate into the central jet which has a higher momentum. The recirculation pattern is weak when the peripheral jet is injected at an angle of  $30^\circ$  towards the central jet (Figure 4.2a). This pattern however disappears for the parallel jet configuration.

Due to the rapid expansion of both the jets, mixing of the two streams starts closer to the inflow plane. A thin stagnation zone appears adjacent to the flat substrate. This condition is favourable for uniform deposition. The deposition rates would however be low. The uniformity is due to the fact that the carrier gas has negligible velocity in the immediate vicinity of the substrate that gives zinc sulphide particles enough residence time to be deposited on the substrate surface. The concentration fields in Figures 4.1(b-e) and Figures 4.2(b-e) reveal a strong influence of the flow pattern. As the reaction is spontaneous zinc spreads a small downstream distance from the inlet plane. Hydrogen sulphide that is injected through the central jet spreads throughout the domain. Its distribution is also strongly controlled by the basic flow pattern of the carrier gas. The zinc consumption rate and the zinc sulphide production rate show that the stretch of the reaction zone does not reach the substrate and is confined near the inlet plane where the two streams mix.

Figures 4.3 and 4.4 show the results with the substrate placed at a dimensionless distance of 0.6 from the inflow plane. The flow fields in the two figures are similar, with the exception of an appearance of a recirculation pattern for the jet angle  $\alpha = 30^\circ$ . The spread of the reaction zone for the parallel jet case ( $\alpha = 0$ ) is slightly higher due to the delay in mixing of the two streams. The zinc consumption zone and zinc sulphide production zone are stretched slightly for the parallel jet configuration ( $\alpha = 0$ ). Zinc spreads a greater distance for the parallel jet configuration as in this case the expansion of the peripheral jet occurs freely without any constraint. But as the peripheral jet is injected with an inward angle it does not expand much and reacts with hydrogen sulphide in the central jet closer to the inflow plane. The distribution of zinc sulphide for the two jet angles are quite similar. But the regions where maximum concentration of zinc sulphide occurs are different. For the parallel jet configuration, this region does not spread to the reactor surface while for the inclined jet configuration, a significant amount of ZnS reaches the reactor side wall. The presence of the recirculation zone does not have any influence on the concentration distribution.

Figures 4.5 and 4.6 show the flow field and species distribution when the diameter of the substrate is higher, (The blockage ratio being 0.45). A weak recirculatory flow occurs for the configuration  $\alpha = 30^\circ$  and is completely absent for the parallel configuration. It is to be noted that with higher blockage levels of velocity near the reactor side wall increases and is more uniform compared to

the lower blockage geometry. The zinc consumption rate and zinc sulphide production rate clearly show that due to free expansion of the peripheral jet, the mixing region is longer for the parallel jet configuration. Hence, the extent of the reaction zone is longer for the parallel jet geometry. The distribution of zinc and zinc sulphide do not show any significant variation from the baseline calculation (Figures 4.1 and 4.2). With higher blockage, a lesser amount of species escapes the reaction zone and is indicative of a reduced loss. The recirculatory pattern is once again quite weak to influence the species distribution. Hence it has no effect on the establishment and size of the reaction zone.

Figures 4.7 and 4.8 present results for the central-to-peripheral jet velocity ratio of 5. Both  $\alpha = 0$  and  $30^\circ$  cases show strong recirculation. For parallel jets, the eye of the vortex appears approximately midway between the inlet and the substrate. For  $\alpha = 30^\circ$ , the recirculation zone shifts toward the inflow plane. Its size being larger, the top of the peripheral jet is reached. The occurrence of a strong recirculatory flow can be attributed to the fact that the peripheral jet is weak and the main flow envelopes the region above the peripheral jet. As the peripheral jet is weaker the extent of the reaction zone is shorter compared to the baseline geometry. Thus it can be concluded that the jet velocity ratio has a stronger influence on mixing over the jet angle. This is clear from Figures 4.7(b,c) and 4.8(b,c). The reaction zones are similar for the two jet angles. The distributions of zinc and zinc sulphide lead to the same conclusion. Thus for a lower jet velocity ratio results are almost independent of the jet angle. A controlling influence is seen only for higher velocity ratios.

With a changes in Reynolds number, the flow field and the distribution of species are significantly altered. Reynolds number is directly related to the mass flow rate of central jet. Figures 4.9 and 4.10 show the results for  $Re=10$ . The central jet expands in the cross-stream direction faster than in the stream-wise direction due to reduced momentum. This improves the mixing of the two streams. The size of the stagnation zone adjacent to the flat substrate increases as the momentum of the central jet diffuses quickly due to a strong viscous effect. Only a weak recirculatory pattern appears for a jet angle of  $30^\circ$ . The reaction zones are similar for the two jet angles. This zone spreads a smaller distance compared to the baseline case indicating good mixing closer to the inflow plane. Distribution of zinc an zinc sulphide show that the species do not spread much and accumulate near the inflow plane. The species that is carried by the central

jet becomes immobile beyond the central plane of the reactor. Thus zinc sulphide remains in vertical layers in the region adjacent to the substrate surface. The species concentration varies near the inlet plane and is nearly uniform at the mid-section of the reactor. The effect of the orientation of the peripheral jet is suppressed by the strong viscous effect at low Reynolds number. Thus, lowering the Reynolds number does not offer any advantage in the reactor performance.

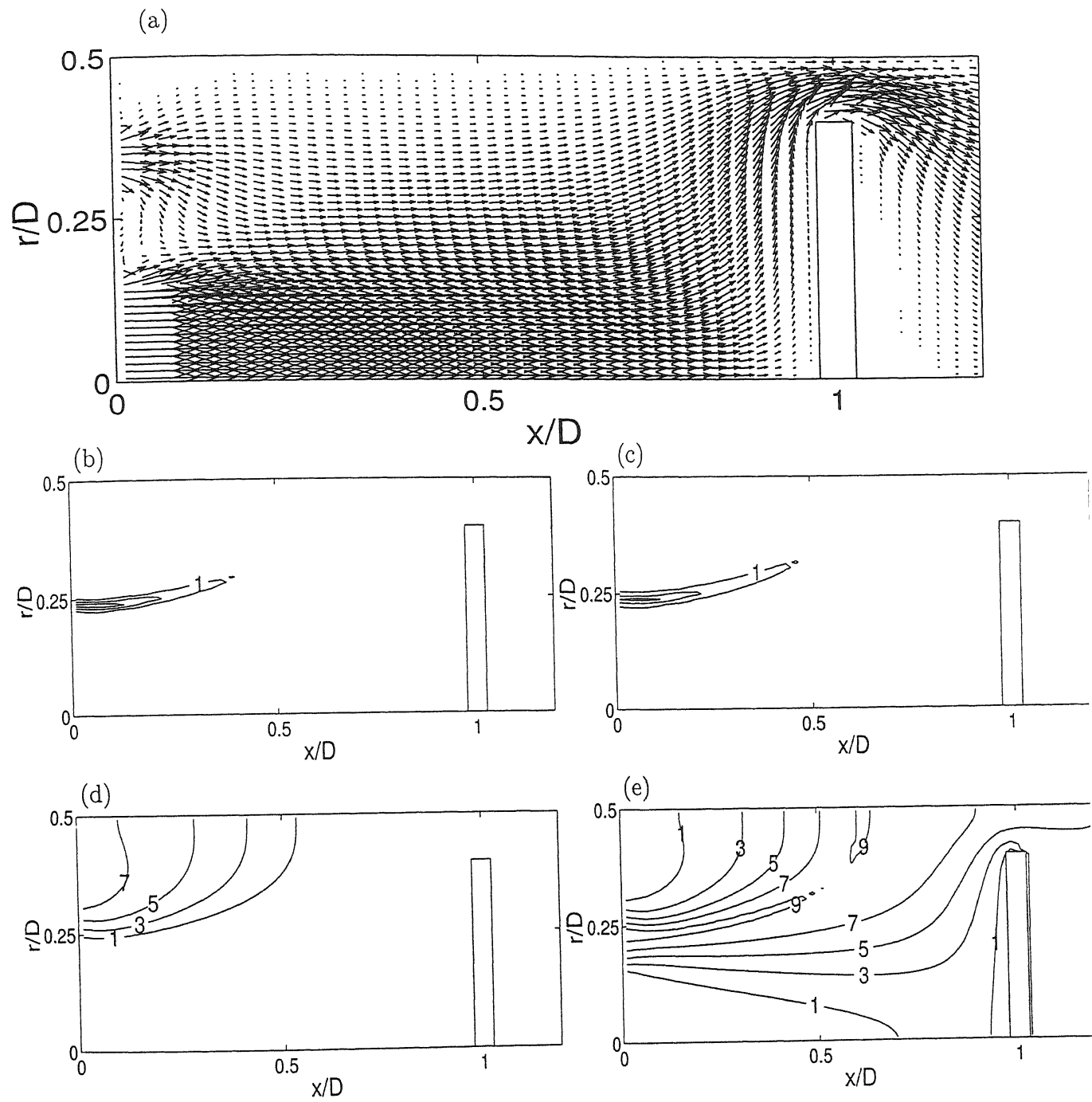


Figure 4.1: Velocity vectors (a), steady state contours of consumption rate of Zn (b), steady state contours of production rate of ZnS (c), contours of mass fraction of Zn (d), contours of mass fraction of ZnS (e), Baseline configuration:  $Re=100$ ,  $V_r = 2$ ,  $r_b = 0.8$ ,  $\alpha = 0$ ,  $Z_b = 1$



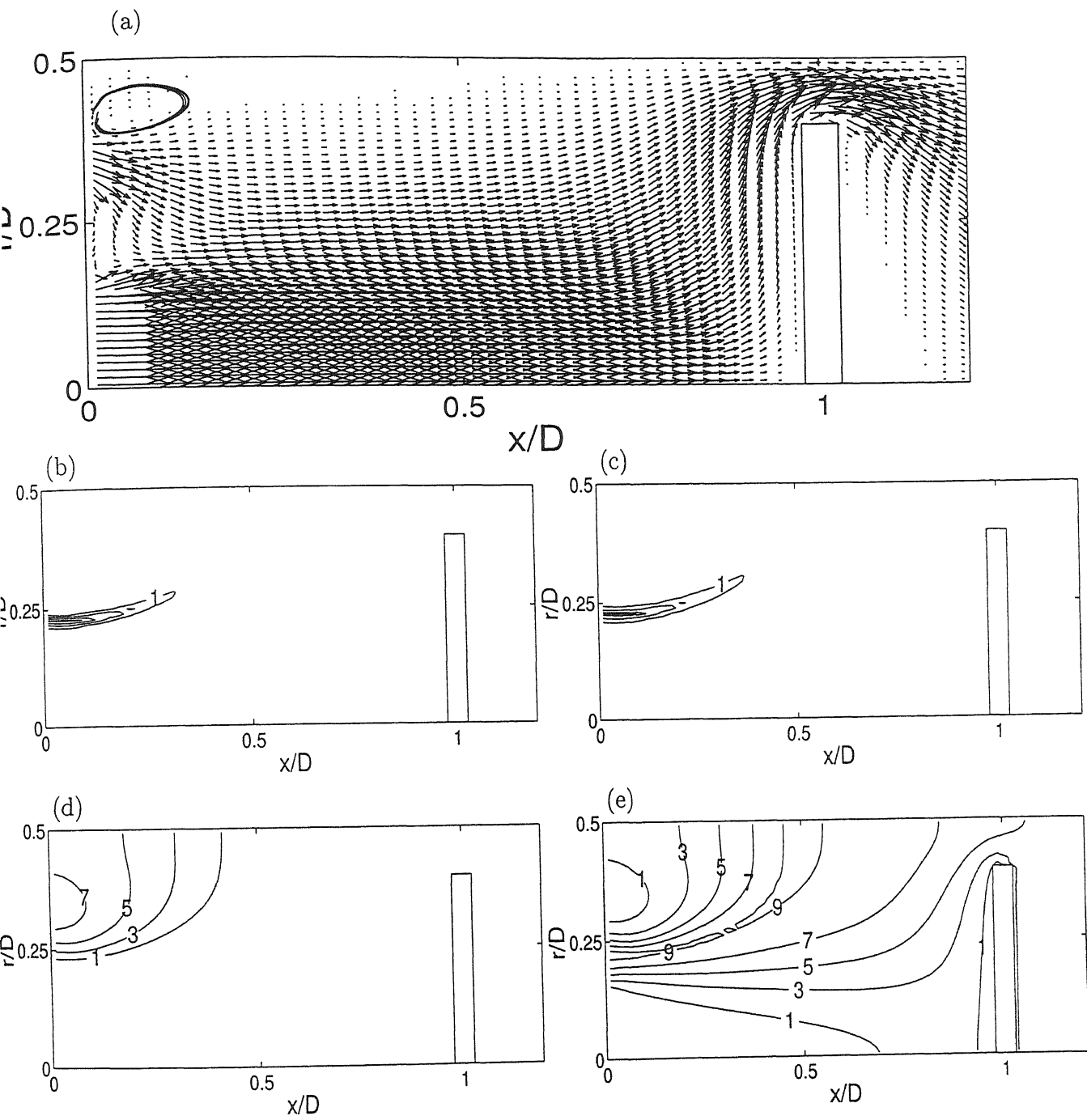


Figure 4.2: Velocity vectors (a), steady state contours of consumption rate of Zn (b), steady state contours of production rate of ZnS (c), contours of mass fraction of Zn (d), contours of mass fraction of ZnS (e),  $Re=100$ ,  $V_r = 2$ ,  $r_b = 0.8$ ,  $\alpha = 30^\circ$  inwards,  $Z_b = 1$

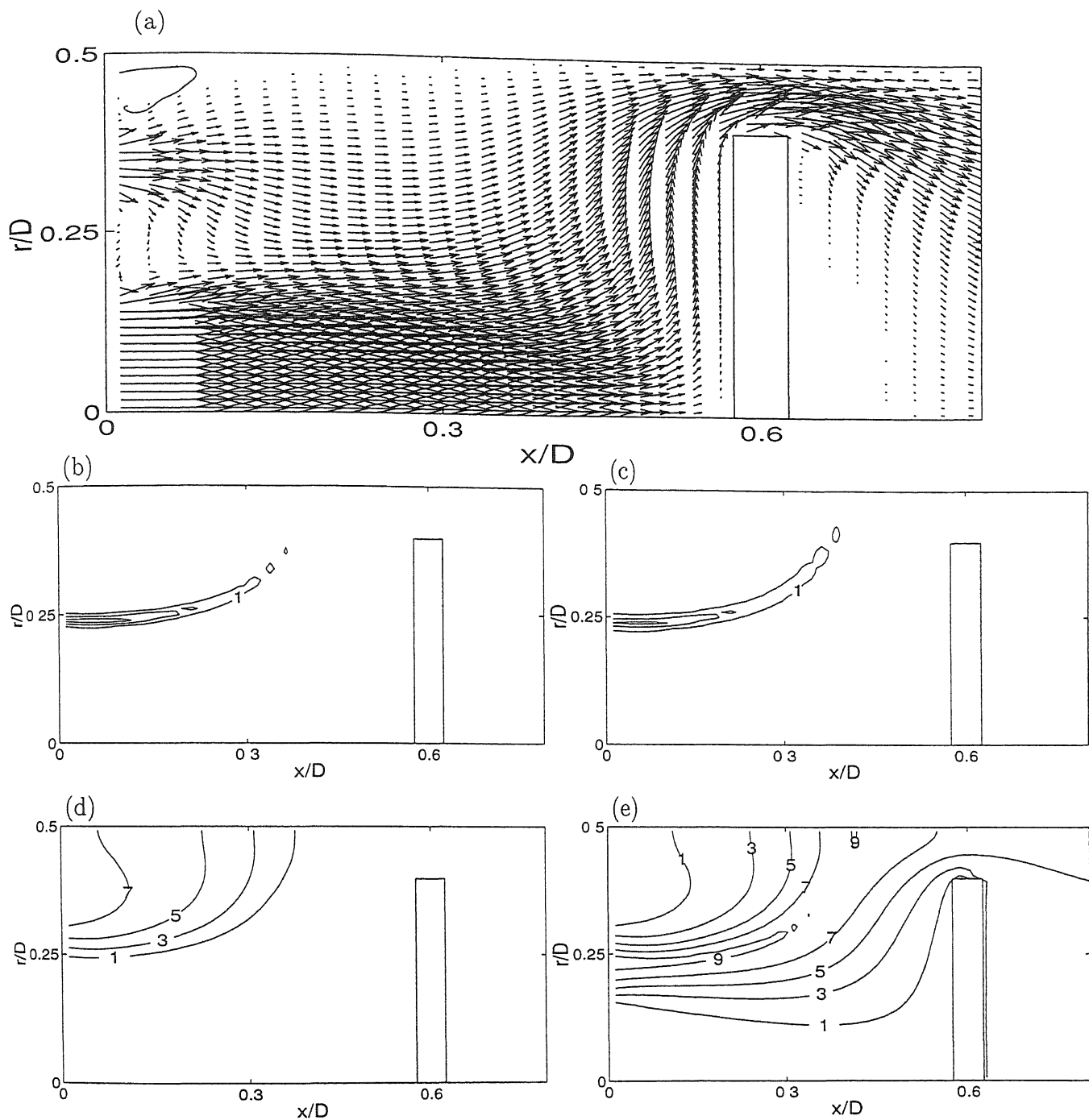


Figure 4.3: Velocity vectors (a), steady state contours of consumption rate of Zn (b), steady state contours of production rate of ZnS (c), contours of mass fraction of Zn (d), contours of mass fraction of ZnS (e),  $Re=100$ ,  $V_r = 2$ ,  $r_b = 0.8$ ,  $\alpha = 0$ ,  $Z_b = 0.6$

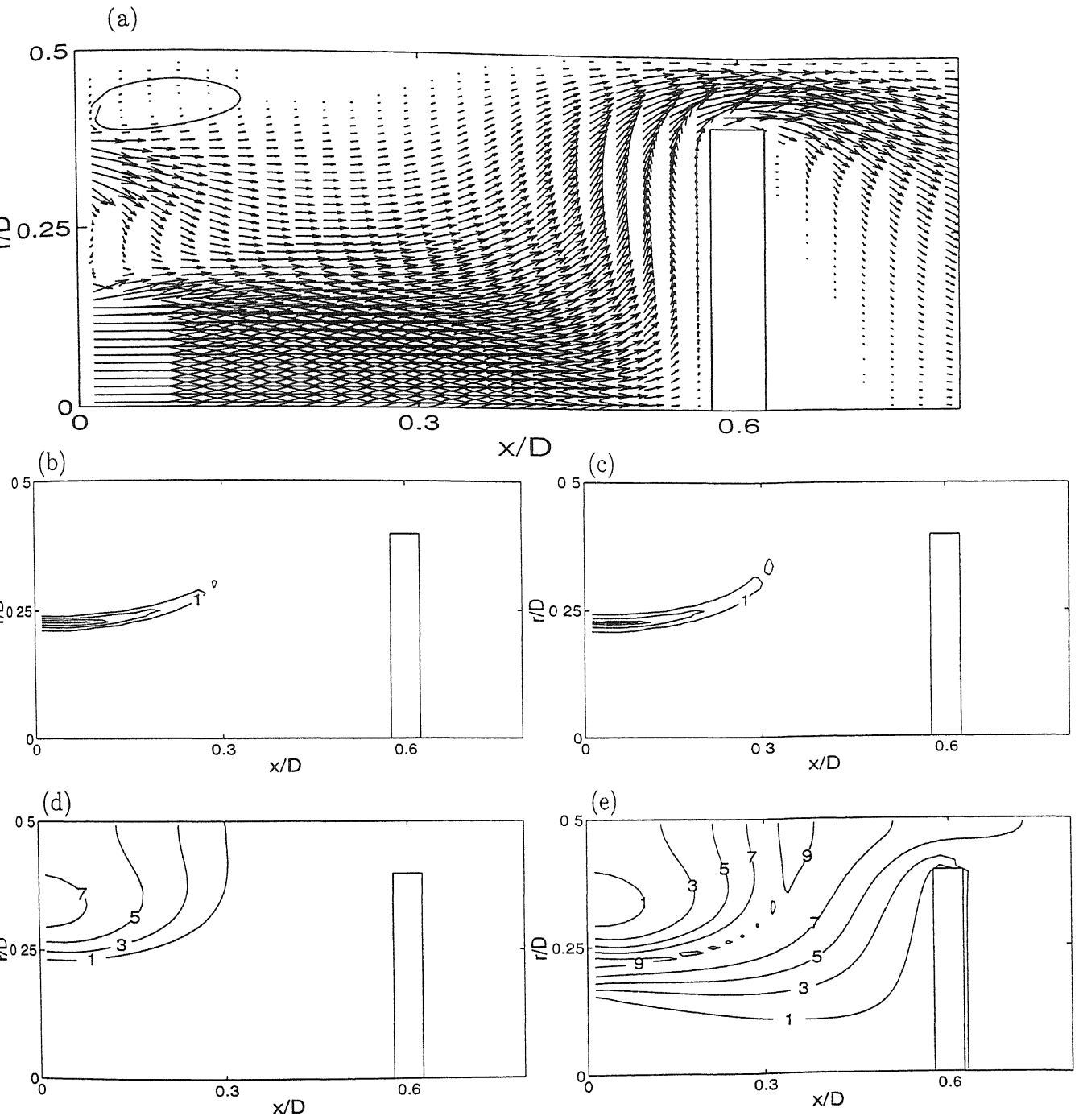


Figure 4.4: Velocity vectors (a), steady state contours of consumption rate of Zn (b), steady state contours of production rate of ZnS (c), contours of mass fraction of Zn (d), contours of mass fraction of ZnS (e),  $Re=100$ ,  $V_r = 2$ ,  $\tau_b = 0.8$ ,  $\alpha = 30^\circ$  inwards,  $Z_b = 0.6$

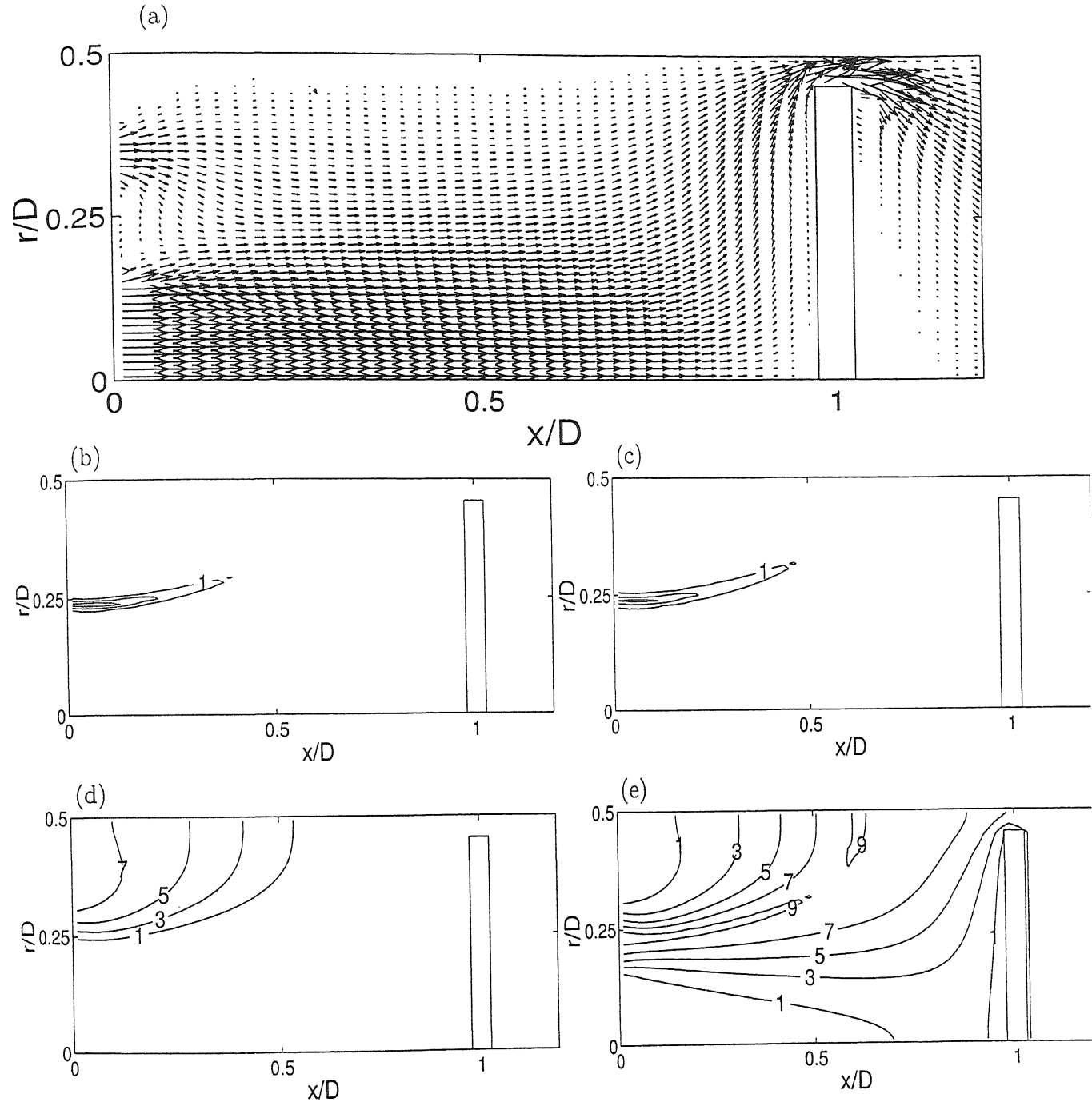


Figure 4.5: Velocity vectors (a), steady state contours of consumption rate of Zn (b), steady state contours of production rate of ZnS (c), contours of mass fraction of Zn (d), contours of mass fraction of ZnS (e),  $Re=100$ ,  $V_r = 2$ ,  $r_b = 0.9$ ,  $\alpha = 0$ ,  $Z_b = 1$

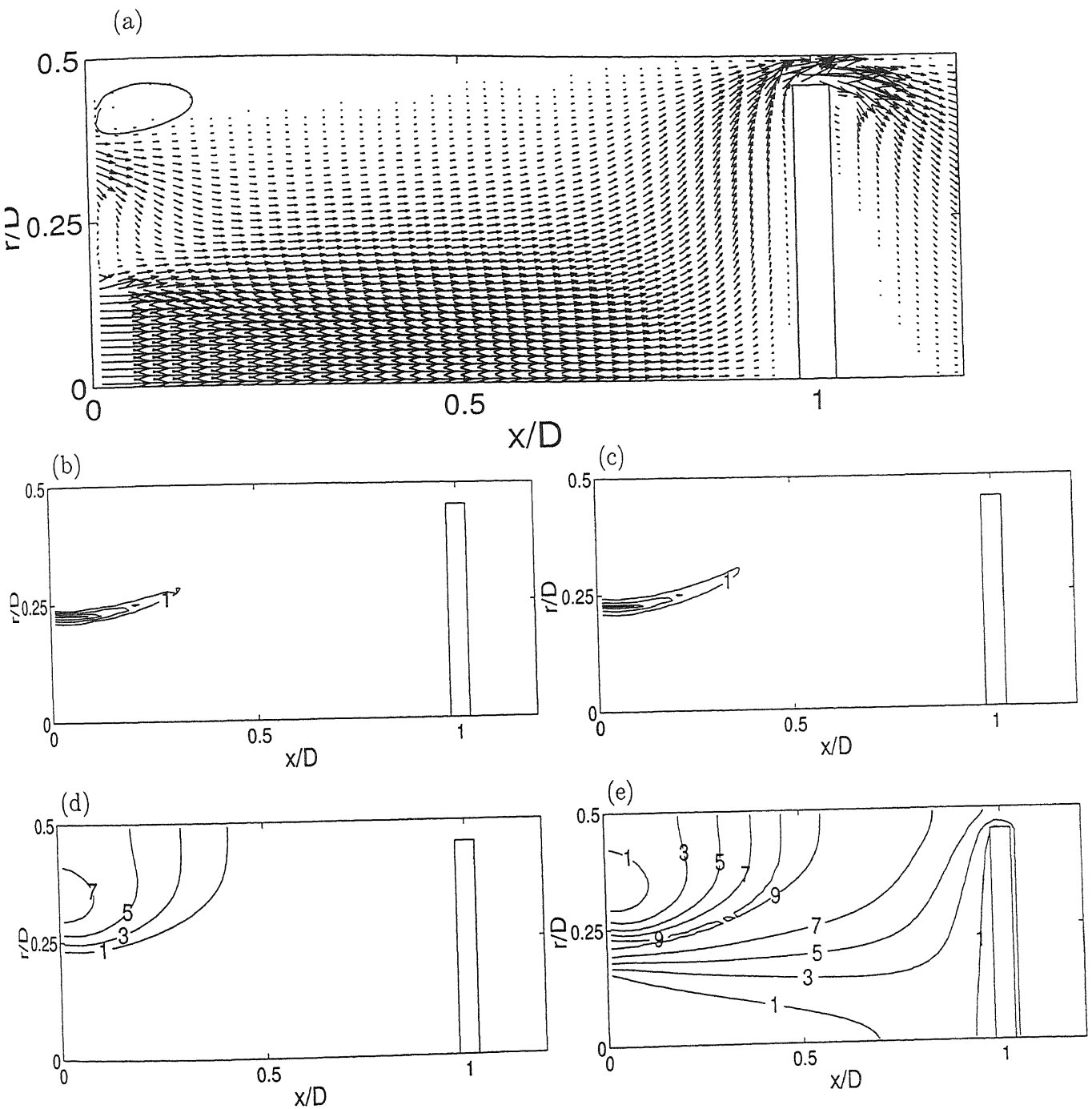


Figure 4.6: Velocity vectors (a), steady state contours of consumption rate of Zn (b), steady state contours of production rate of ZnS (c), contours of mass fraction of Zn (d), contours of mass fraction of ZnS (e),  $Re=100$ ,  $V_r = 2$ ,  $r_b = 0.9$ ,  $\alpha = 30^\circ$  inwards,  $Z_b = 1$

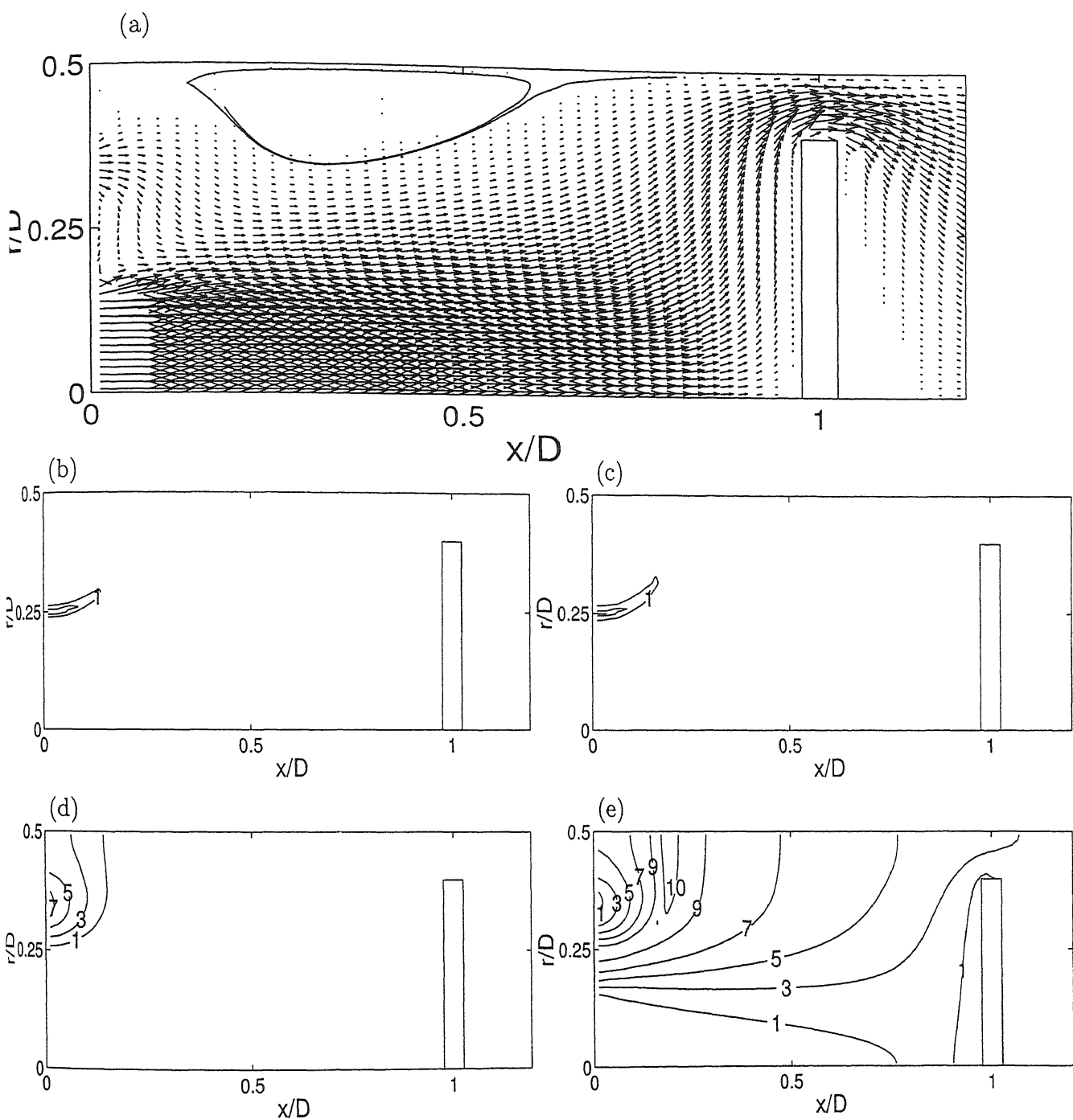


Figure 4.7: Velocity vectors (a), steady state contours of consumption rate of Zn (b), steady state contours of production rate of ZnS (c), contours of mass fraction of Zn (d), contours of mass fraction of ZnS (e),  $Re=100$ ,  $V_r = 5$ ,  $r_b = 0.8$ ,  $\alpha = 0$ ,  $Z_b = 1$

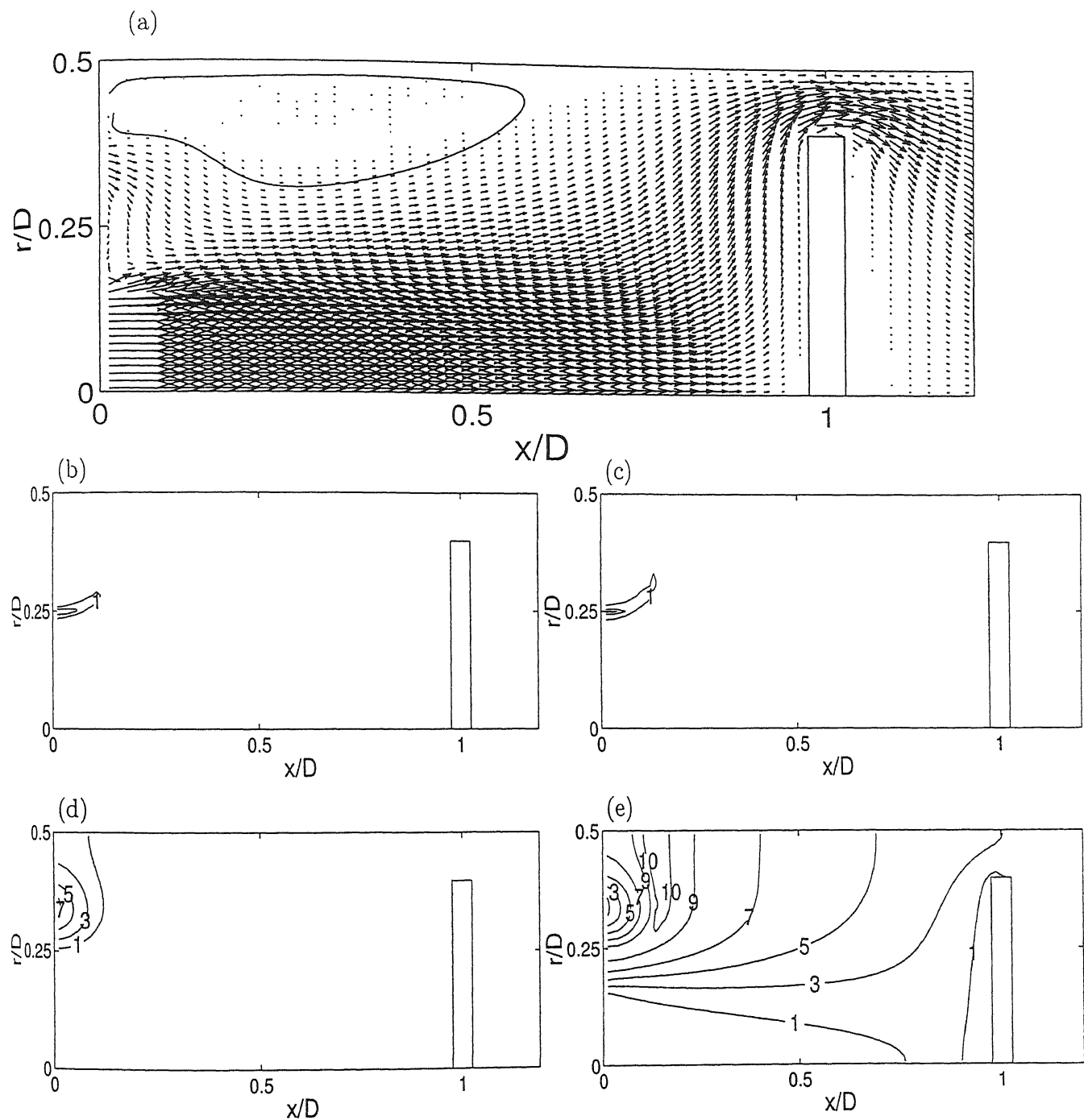


Figure 4.8: Velocity vectors (a), steady state contours of consumption rate of Zn (b), steady state contours of production rate of ZnS (c), contours of mass fraction of Zn (d), contours of mass fraction of ZnS (e),  $Re=100$ ,  $V_r = 5$ ,  $r_b = 0.8$ ,  $\alpha = 30^\circ$  inwards,  $Z_b = 1$

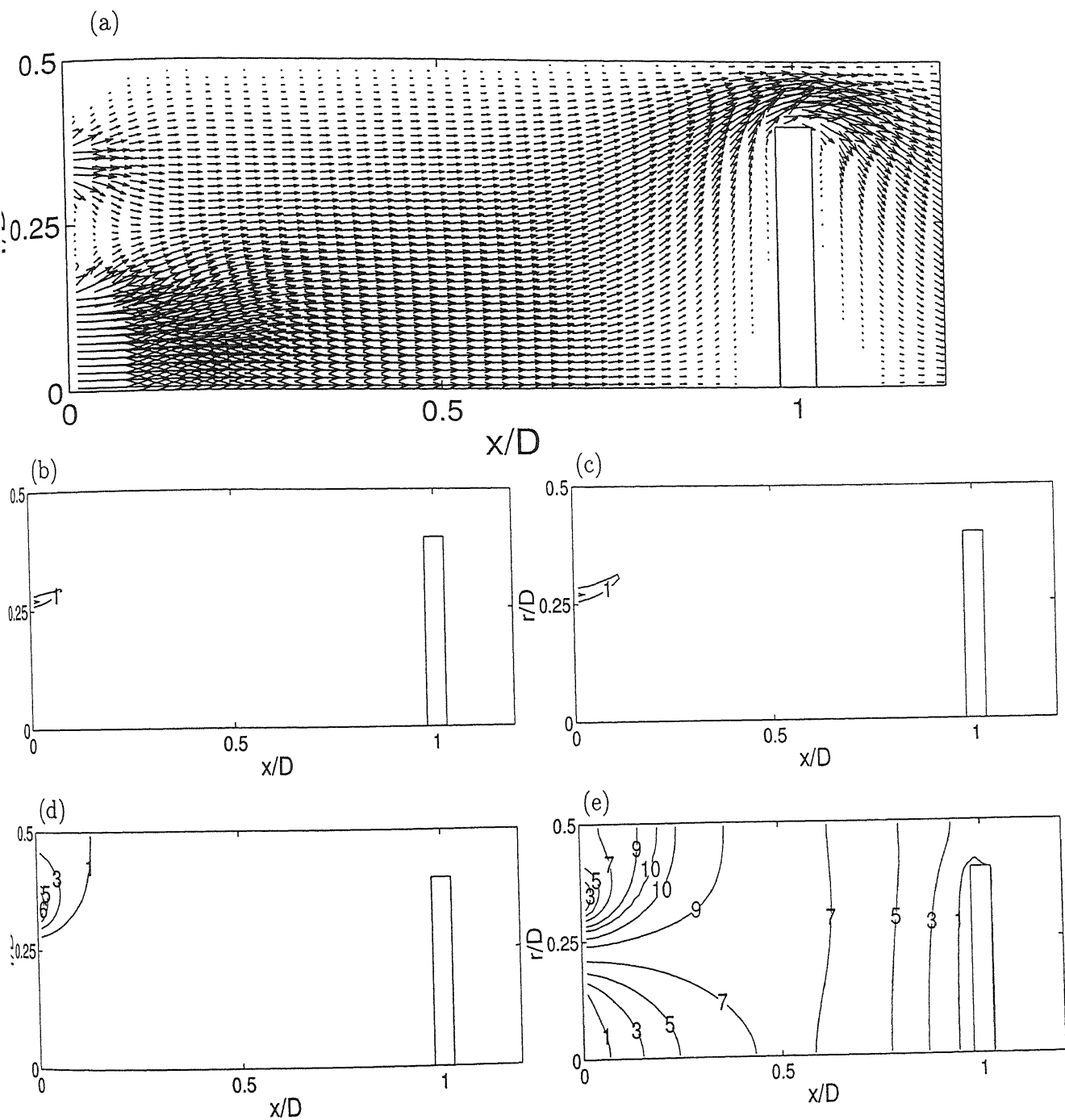


Figure 4.9: Velocity vectors (a), steady state contours of consumption rate of Zn (b), steady state contours of production rate of ZnS (c), contours of mass fraction of Zn (d), contours of mass fraction of ZnS (e),  $Re=10$ ,  $V_r = 2$ ,  $r_b = 0.8$ ,  $\alpha = 0$ ,  $Z_b = 1$



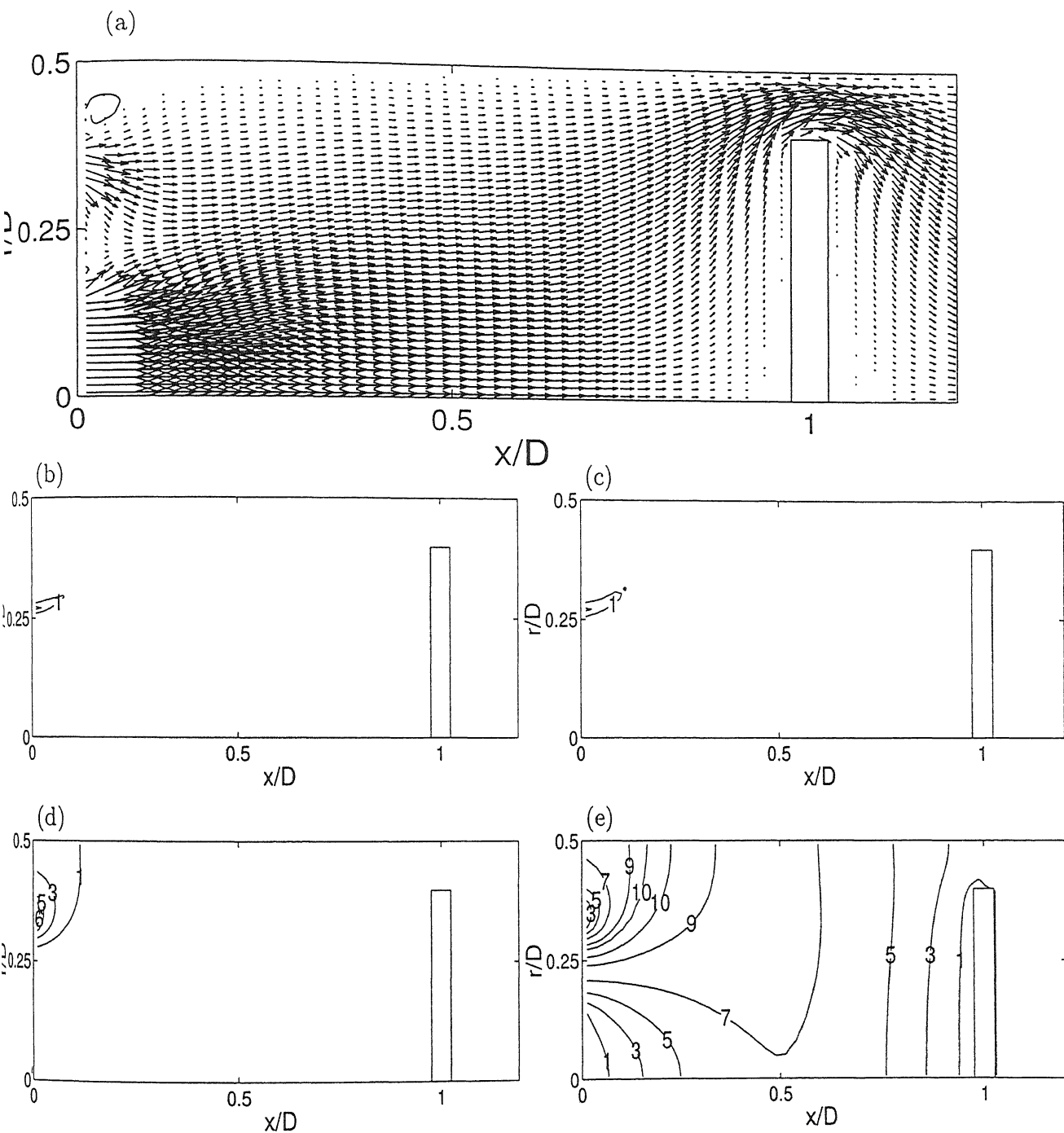


Figure 4.10: Velocity vectors (a), steady state contours of consumption rate of Zn (b), steady state contours of production rate of ZnS (c), contours of mass fraction of Zn (d), contours of mass fraction of ZnS (e),  $Re=10$ ,  $V_r = 2$ ,  $r_b = 0.8$ ,  $\alpha = 30^\circ$  inwards,  $Z_b = 1$

### 4.1.2 Reactor with a concave substrate

Results for the CVD reactor with a concave substrate are discussed below along with the figures for flow and concentration fields.

Figures 4.11 and 4.12 show the results for the baseline case of  $Re = 100$ ,  $V_r = 2$ ,  $r_b = 0.8$ ,  $Z_b = 1$ . Flow fields for the cases of  $\alpha = 0$  and  $30^\circ$  are practically similar. For the geometry with  $\alpha = 30^\circ$  a recirculation pattern is visible while for the parallel jets case it disappears. The stagnation zone attached to the substrate surface is larger when compared to the flat substrate geometry. The recirculatory zone occurs just above the peripheral jet and velocity near the reactor wall is small everywhere. An exception occurs in the annular region between the substrate and the reactor wall. In this region the fluid stream passes through a narrow annulus. Hence flow accelerates and the velocity is quite high. In the parallel jet geometry the peripheral jet freely expands and thus mixing with the central jet occurs over a longer distance compared to  $\alpha = 30^\circ$ . The reaction zone is not affected due to the curvature of the substrate as it is placed at a downstream distance that is not enough to alter remarkably the flow field. Thus the stretch of the reaction zone is similar to the case of flat substrate.

The distribution of zinc in the reactor is similar for the two jet angles. It spreads however for a longer distance for the parallel jet geometry. Zinc sulphide spreads over the entire domain up to the substrate and its distribution is identical for the two angles. In the present geometry, the concavity of the substrate surface alters the flow direction near the obstacle and is not similar to the case of a flat substrate. Flow moves backward near the surface which pushes the region rich in zinc towards the inflow plane. Thus the zinc-rich region is smaller and nearer to the inlet plane for the concave geometry. This result is not seen in the hydrogen sulphide distribution because the central jet through which this species is injected has significant inertia in the stream-wise direction.

Figures 4.13 and 4.14 present the results for the case with substrate placed at a dimensionless distance of 0.6 from the inflow plane. There is no significant recirculation pattern for the parallel jet case while a weak pattern appears for  $\alpha = 30^\circ$ . This pattern occurs at an angle to the flow direction for the curved block, in comparison to the flat substrate. The size of the stagnation region decreases when the substrate is brought closer to the inflow plane. The length of the reaction zone is greater for the parallel jet geometry ( $\alpha = 0$ ) compared

to  $\alpha = 30^\circ$ . It can be seen in Figures 4.13(b,c) and 4.11(b,c) that the reaction zone reaches the reactor side wall to a greater extent when compared to the flat substrate, mainly due to its dependence on the basic flow pattern of the carrier gas. Zinc sulphide distribution for the curved block also shows a similar deviation from the flat substrate. The reason is the backflow of the bulk fluid ahead of the stagnation zone. Thus for the concave substrate, though more zinc sulphide reaches the substrate surface due to its concavity, the reaction zone and the region rich in zinc sulphide shift in the upstream direction.

With the increase in the diameter of the substrate, Figures 4.15 and 4.16, the flow field does not change significantly. Trends observable for the flat substrate geometry are once again reproduced. For the parallel and inclined jets  $\alpha = 0$  and  $\alpha = 30^\circ$ , the recirculation pattern is absent. The velocities throughout the domain are slightly higher due to a higher blockage ratio. The effect of blockage and the concavity of the substrate surface does not lead to a velocity distribution that varies significantly in the middle section of the reactor. This result was also obtained in the flat substrate simulation. For the parallel jet geometry the reaction region is slightly stretched, indicating that mixing occurs over a longer distance compared to  $\alpha = 30^\circ$ . This reaction zone is quite similar to the baseline case. The distribution of zinc is similar for the two geometries with different peripheral jet angles. The zone rich in zinc shifts upstream compared to the flat substrate geometry. Zinc sulphide distribution also shows a similar trend. These observations lead to the conclusion that the blockage ratio has a marginal effect on the flow and species concentration fields.

Figures 4.17 and 4.18 present numerical results when the central-to-peripheral jet velocity ratio is 5. For both cases ( $\alpha = 0$  and  $\alpha = 30^\circ$ ) a strong recirculation pattern occurs near the reactor wall. The size of this pattern however is smaller when compared to the flat substrate geometry. This is due to the concavity of the substrate which leads to a considerable negative axial velocity. The zinc consumption rate and zinc sulphide production rate decrease significantly due to incomplete mixing. There are no observable differences in the reaction zone between the present case and the one with a flat substrate at a jet velocity ratio of 5. Concentration distribution of all the species show that due to lower velocity of the peripheral jet, zinc does not spread over an appreciable distance. It leads to a reaction zone confined closer to the inlet plane. Moreover, the zone containing the maximum zinc sulphide shifts to the reactor wall due to the presence

of a weak peripheral jet. This is certainly an adverse effect with respect to the deposition rate and the throughput of the reactor.

Figures 4.19 and 4.20 show the flow and concentration fields for  $Re=10$ . Due to larger viscous forces both the central and the peripheral jets expand near the inlet plane leading to an early mixing of the streams. The lower levels of velocity through out the domain compounded with the effect of concavity of the substrate surface results in a large stagnation region. This result was also seen for the flat substrate. The absence of convective effects leads to stagnant vertical layers of ZnS over a larger portion of the reactor. This distribution is not helpful for higher rates of deposition but is favorable if the goal is to form a uniform layer. The distribution of zinc shows that due to a higher transverse diffusion of momentum this species has been restricted to a limited zone near the inlet plane. The region where zinc is consumed and zinc sulphide is produced are also restricted to the vicinity of the inlet plane.

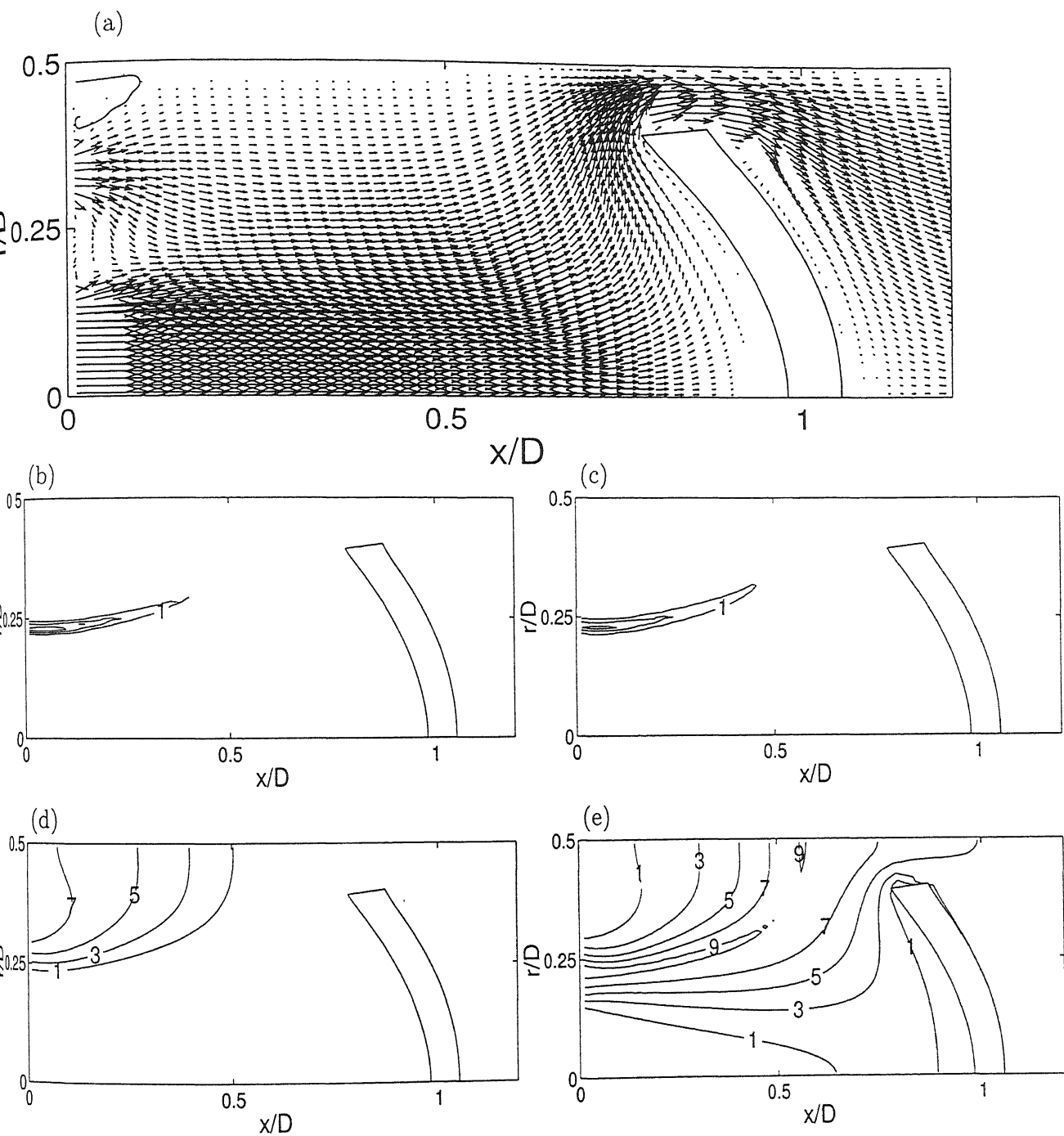


Figure 4.11: Velocity vectors (a), steady state contours of consumption rate of Zn (b), steady state contours of production rate of ZnS (c), contours of mass fraction of Zn (d), contours of mass fraction of ZnS (e), Baseline configuration:  $Re=100$ ,  $V_r = 2$ ,  $r_b = 0.8$ ,  $\alpha = 0$ ,  $Z_b = 1$

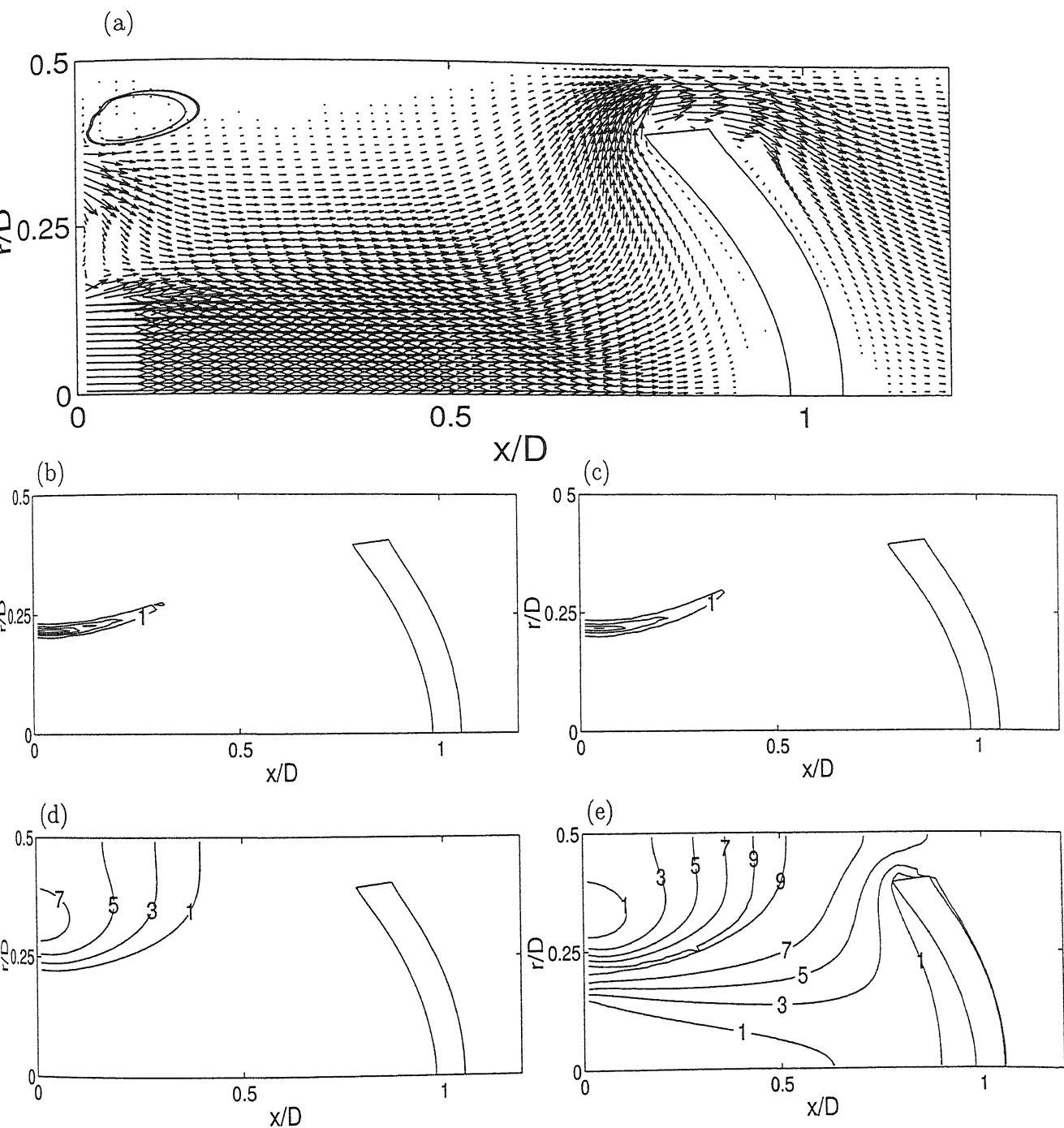


Figure 4.12: Velocity vectors (a), steady state contours of consumption rate of Zn (b), steady state contours of production rate of ZnS (c), contours of mass fraction of Zn (d), contours of mass fraction of ZnS (e),  $Re=100$ ,  $V_r = 2$ ,  $r_b = 0.8$ ,  $\alpha = 30^\circ$  inwards,  $Z_b = 1$

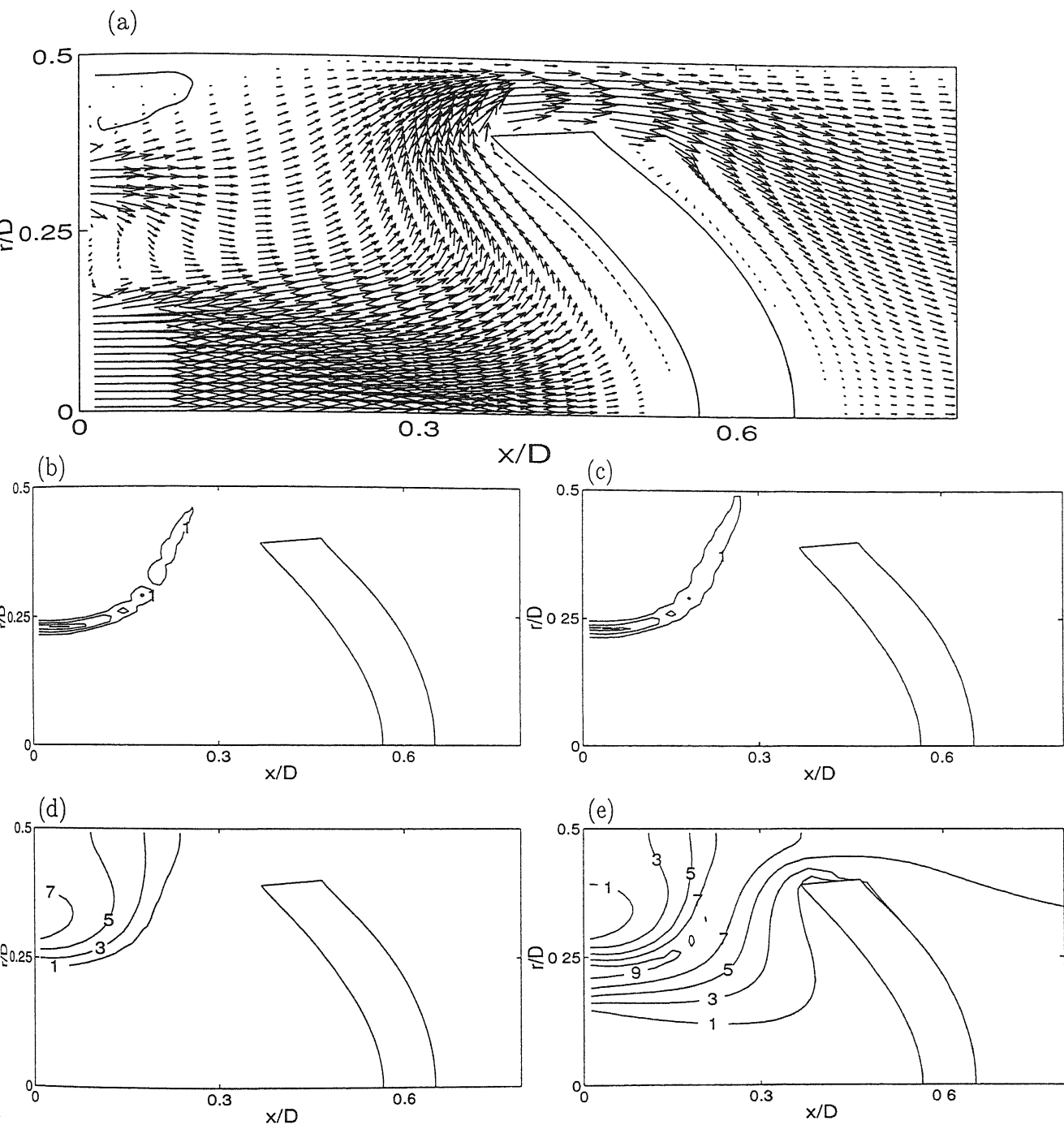


Figure 4.13: Velocity vectors (a), steady state contours of consumption rate of Zn (b), steady state contours of production rate of ZnS (c), contours of mass fraction of Zn (d), contours of mass fraction of ZnS (e),  $Re=100$ ,  $V_r = 2$ ,  $r_b = 0.8$ ,  $\alpha = 0$ ,  $Z_b = 0.6$

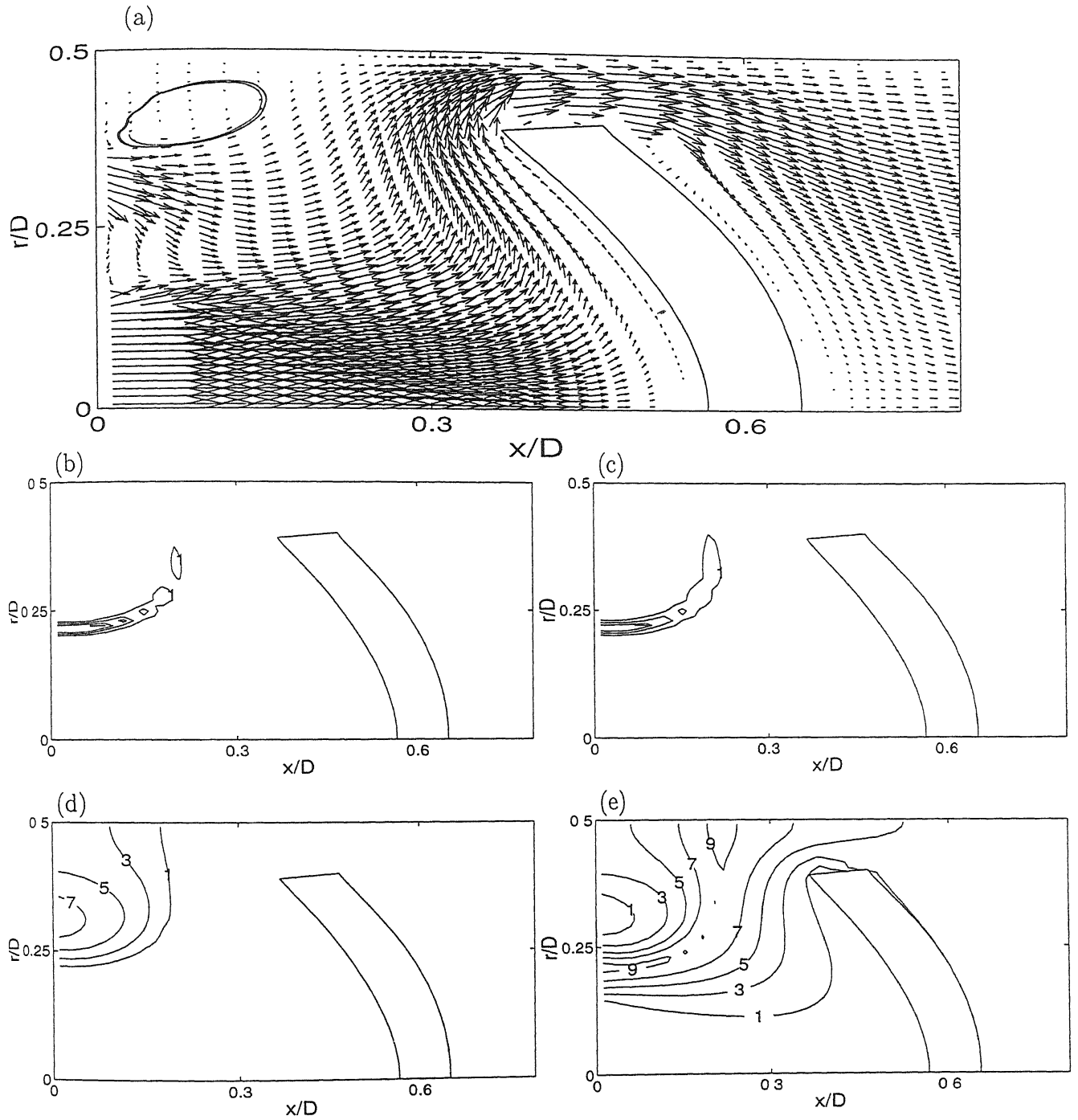


Figure 4.14: Velocity vectors (a), steady state contours of consumption rate of Zn (b), steady state contours of production rate of ZnS (c), contours of mass fraction of Zn (d), contours of mass fraction of ZnS (e),  $Re=100$ ,  $V_r = 2$ ,  $r_b = 0.8$ ,  $\alpha = 30^\circ$  inwards,  $Z_b = 0.6$



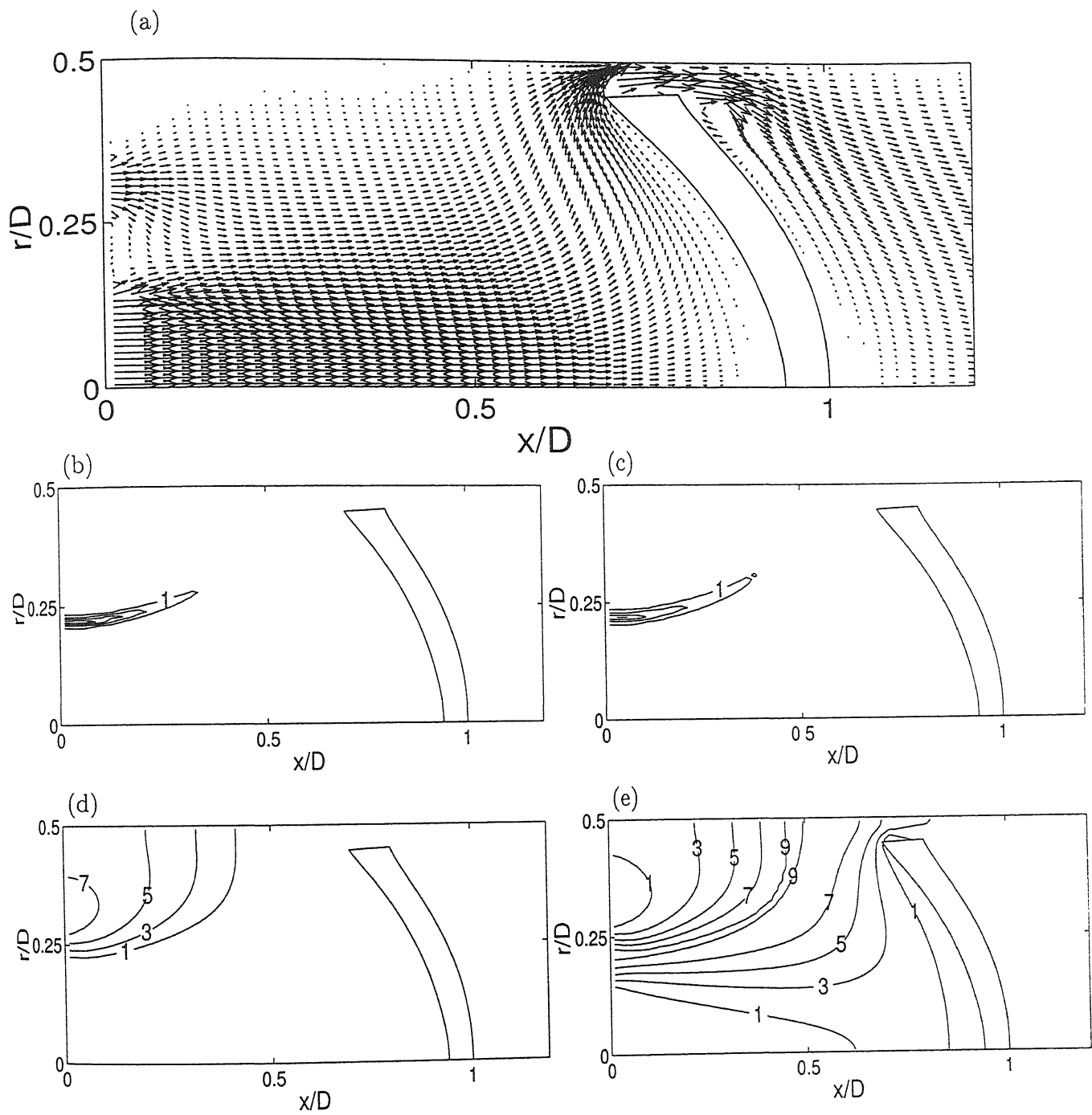


Figure 4.15: Velocity vectors (a), steady state contours of consumption rate of Zn (b), steady state contours of production rate of ZnS (c), contours of mass fraction of Zn (d), contours of mass fraction of ZnS (e),  $Re=100$ ,  $V_r = 2$ ,  $r_b = 0.9$ ,  $\alpha = 0$ ,  $Z_b = 1$

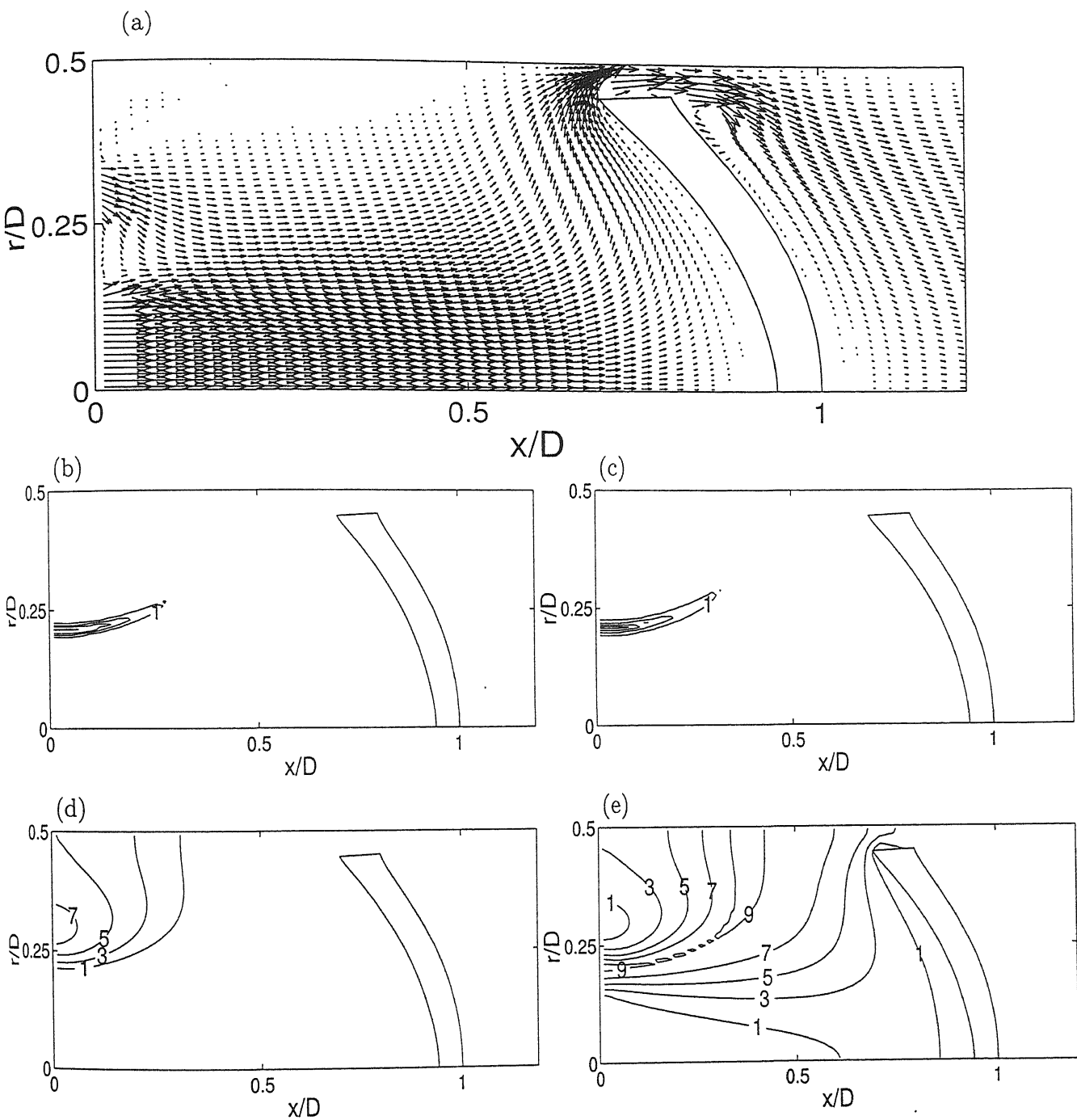


Figure 4.16: Velocity vectors (a), steady state contours of consumption rate of Zn (b), steady state contours of production rate of ZnS (c), contours of mass fraction of Zn (d), contours of mass fraction of ZnS (e),  $Re=100$ ,  $V_r = 2$ ,  $r_b = 0.9$ ,  $\alpha = 30^\circ$  inwards,  $Z_b = 1$

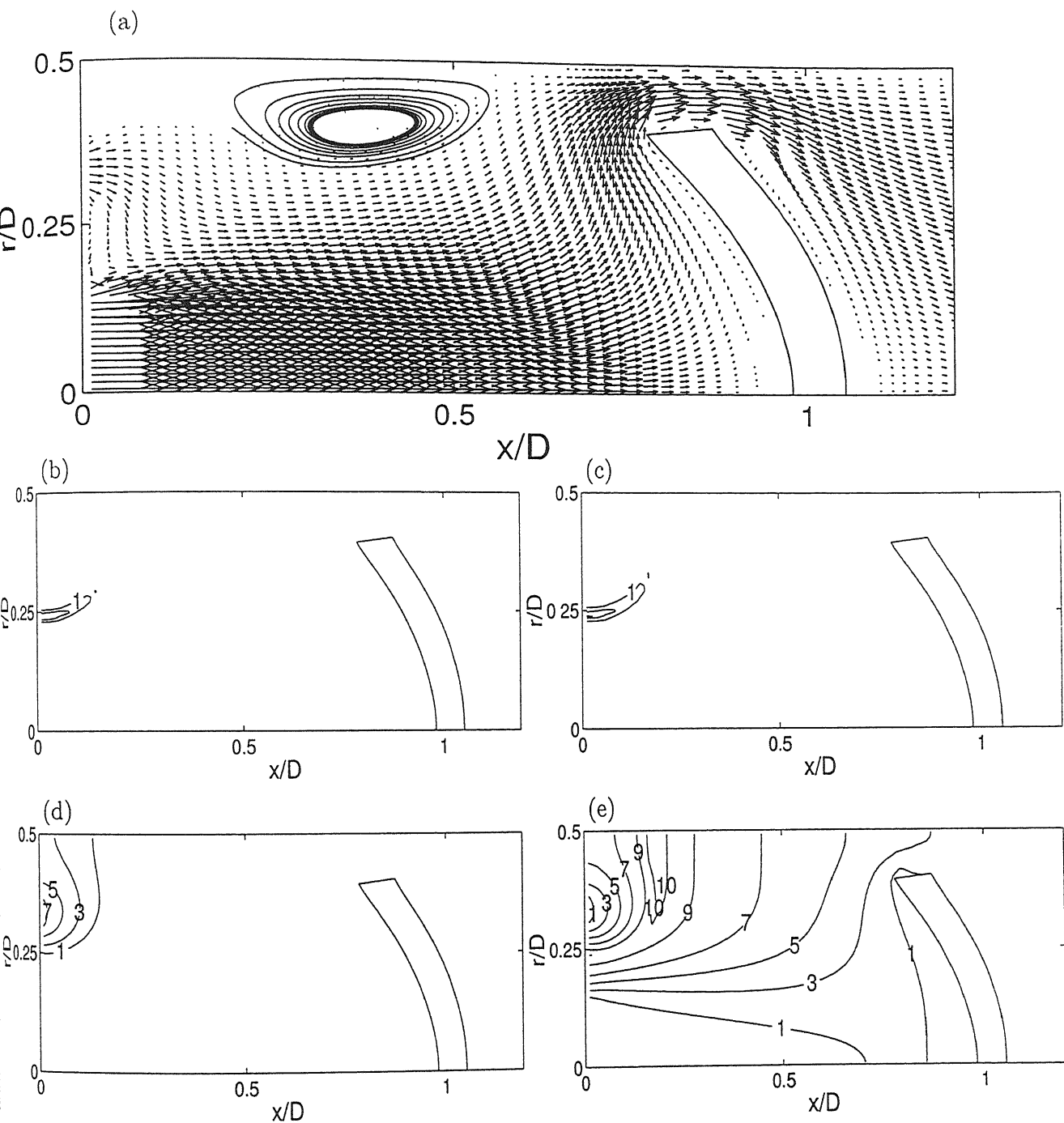


Figure 4.17: Velocity vectors (a), steady state contours of consumption rate of Zn (b), steady state contours of production rate of ZnS (c), contours of mass fraction of Zn (d), contours of mass fraction of ZnS (e),  $Re=100$ ;  $V_r = 5$ ,  $r_b = 0.8$ ,  $\alpha = 0$ ,  $Z_b = 1$

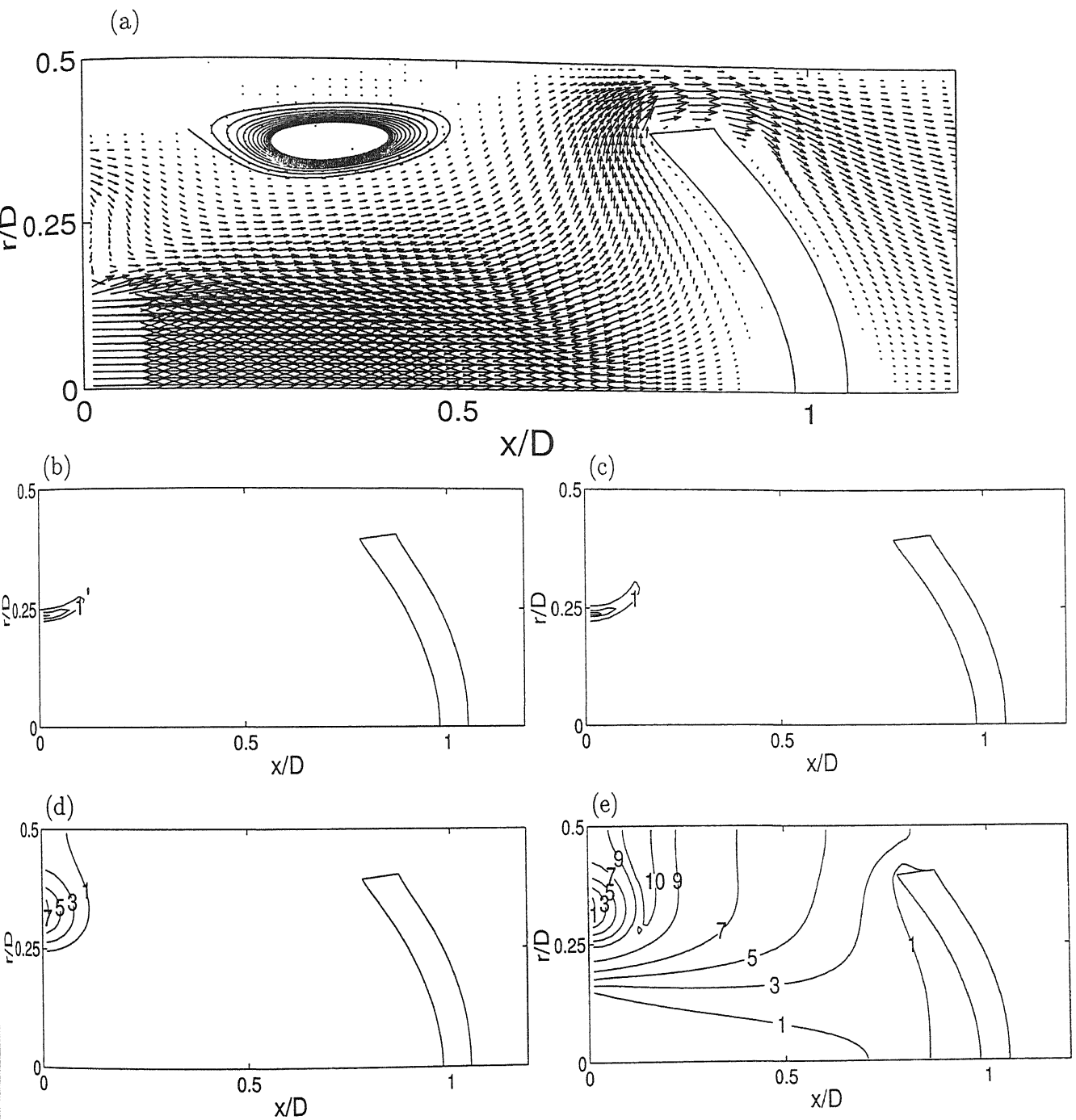


Figure 4.18: Velocity vectors (a), steady state contours of consumption rate of Zn (b), steady state contours of production rate of ZnS (c), contours of mass fraction of Zn (d), contours of mass fraction of ZnS (e),  $Re=100$ ,  $V_r = 5$ ,  $r_b = 0.8$ ,  $\alpha = 30^\circ$  inwards,  $Z_b = 1$

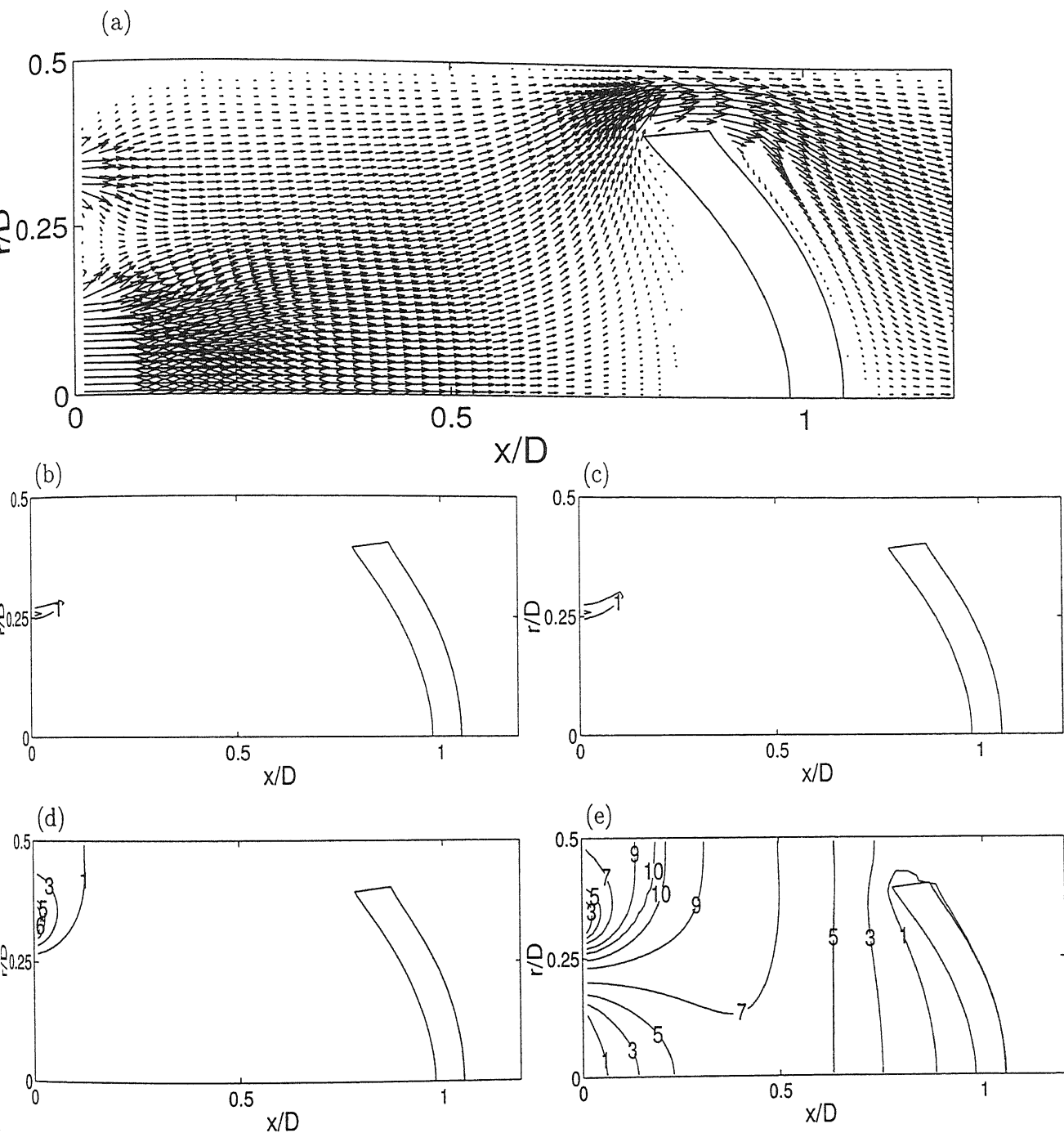


Figure 4.19: Velocity vectors (a), steady state contours of consumption rate of Zn (b), steady state contours of production rate of ZnS (c), contours of mass fraction of Zn (d), contours of mass fraction of ZnS (e),  $Re=10$ ,  $V_r = 2$ ,  $r_b = 0.8$ ,  $\alpha = 0$ ,  $Z_b = 1$

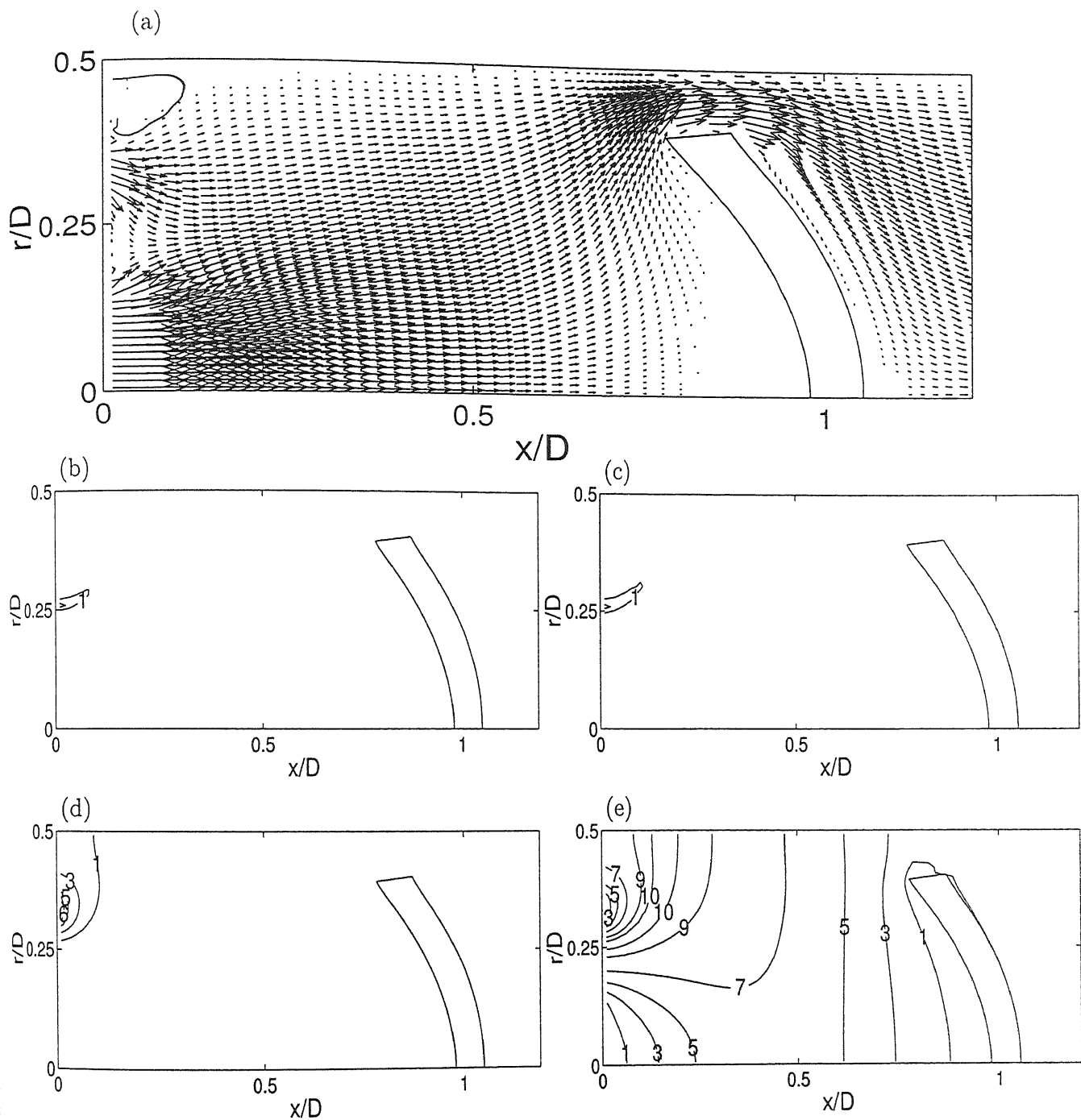


Figure 4.20: Velocity vectors (a), steady state contours of consumption rate of Zn (b), steady state contours of production rate of ZnS (c), contours of mass fraction of Zn (d), contours of mass fraction of ZnS (e),  $Re=10$ ,  $V_r = 2$ ,  $r_b = 0.8$ ,  $\alpha = 30^\circ$  inwards,  $Z_b = 1$

## 4.2 Wall shear stress and deposition rate of zinc sulphide

In this section results are presented in terms of wall shear stress and the deposition rate of zinc sulphide on the substrate surface. the dimensionless local wall shear stress, namely the skin friction coefficient is defined as

$$C_f = \frac{\tau_w}{\frac{1}{2}\rho_{ca}U_c^2} = \frac{\mu \frac{\partial u}{\partial n}}{\frac{1}{2}\rho_{ca}U_c^2}$$

The deposition rate signifies the volumetric rate at which a zinc sulphide layer is added to the substrate. Instead of the absolute thickness, the deposition rate is a more relevant parameter since it permits a comparative assessment of the role of the flow parameters and reactor geometry. The local deposition rate is calculated as follows.

$$\frac{ds}{dt} = \frac{F_d^s}{\rho_{ZnS}A_s} = \frac{\rho_{ca}D_{ZnS}\nabla\omega.A_s}{\rho_{ZnS}A_s}$$

where  $s$  is the thickness of zinc sulphide deposited,  $F_d^s$  is the diffusive mass flux of zinc sulphide on the substrate given in Kg/s,  $A_s$  is the surface area vector of the substrate and  $D_{ZnS}$  is the binary diffusion coefficient of zinc sulphide into argon.

### 4.2.1 Properties of a flat substrate

Figure 4.21 shows the axial variation of the skin friction coefficient along the reactor wall. shear stresses are significantly higher on the wall adjacent to the annular region. As the bulk fluid stream passes through this narrow annulus fluid stream accelerates leading to increase in shear stress. Elsewhere shear stress is uniform and quite low in magnitude. It can be seen that values of the skin friction coefficient are relatively higher at all the points on the reactor wall for  $Re=10$ . Shear stress is minimum for jet ratio 5 which shows that at lower peripheral jet velocities very small amount of fluid reaches the reactor wall. The variation of skin friction coefficient is practically identical for  $\alpha = 0$  and  $\alpha = 30^\circ$  as can be seen from the Figures 4.21(a) and (b). Thus effect of jet angles is not felt at the reactor wall.

Figure 4.22 shows the effect of Reynolds number on the skin friction coefficient  $C_f$  and the deposition rate of zinc sulphide on the substrate surface. Shear stress increases linearly along the substrate surface as one moves away from the axis of the reactor. Fairly large shear stresses are encountered at the tip of the substrate. Fluid velocities are small in the stagnation zone adjacent to the substrate. The extent of this region decreases as one progresses towards the tip of the substrate, leading to significant velocity gradients. It can be seen that shear stress levels are lower for  $Re=100$ . This shows that viscous forces acting on the substrate are relatively higher at  $Re=10$ .

The deposition rate is almost invariant closer to the axis and varies significantly around the tip of the substrate. This trend near the edges of the substrate is an indication of a nonuniform thickness of the deposited material. The growth rate is higher at  $Re=100$  at the tip of the substrate. This is because at higher velocities near the substrate surface, particles of zinc sulphide do not have the residence time for deposition, leading to a lower deposition rate. In the region near the reactor axis deposition rate is small because generation rates of zinc sulphide are negligible (Section 4.1). Results show that jet angle at the inlet plane does not have an impact on the deposition rate and the shear stress on the solid surface.

Figure 4.23 shows the effect of the position of the substrate on the shear stress and deposition profile on the substrate surface. When substrate is placed closer to the inlet plane the fluid stream injected through the central jet reaches the substrate leading to higher velocities near the substrate. This leads to a higher skin friction coefficient for the case  $Z_b = 0.6$  on the substrate surface. This effect is significant away from the tip as well. The deposition rate distribution follows the trends of shear stress on the surface. The deposition rate at the tip of the substrate does not depend strongly on substrate position. The effect of the jet injection angle  $\alpha$  is insignificant, though the parallel jet configuration predicts a marginally higher deposition rate.

The effect of an increase in the diameter of the substrate is depicted in Figure 4.24. Shear stress and deposition rate profiles on the substrate surface are practically identical for the two blockage ratios. With a higher blockage, shear stress at the tip of the substrate is approximately twice the value for the lower blockage. This is due to the fact that increase in blockage reduces the area of the annulus between the substrate and the reactor wall. Thus fluid acceleration is



higher compared to the case of lower blockage ratio leading to significant increase in velocity gradient in the annular region. Figure 4.21 shows the axial variation of the skin friction coefficient on the reactor wall for the increased blockage ratio. The shear stress is significantly higher at the region above the substrate. Elsewhere it is almost a constant with a small value. The injection angle of the peripheral jet has only a marginal effect on the wall properties.

Figure 4.25 shows the effect of changing the central-to-peripheral jet velocity ratio on the shear stress and growth profile on the substrate surface. The interdependence of the distribution of shear stress and the deposition rate on the substrate surface for this case is different from the other parameters. A higher peripheral jet velocity (a lower velocity ratio  $V_r = 2$  compared to 5) shows higher levels of shear stress and deposition rate on the surface. This is in contrast to the earlier results. The transport aspects of the species are seen to be more important than the base flow field of argon. Due to a higher peripheral jet velocity, the extent of the reaction zone is larger leading to the production of zinc sulphide closer to the substrate.

For lower velocity ratio, the species front moves very slowly and reactions occur within a restricted zone close to the injection plane. Thus the distribution of the shear stress on the substrate surface does not give an estimate of the deposition profile. The axial variation of the shear stress on the reactor wall follows the same trend over a range of parameters. When the velocity ratio is higher, a slightly higher shear stress in the tip region of the substrate is observed. The injection angle of the peripheral jet does not have any significant effect on the reactor properties. Thus changing the jet velocity ratio from 2 to 5 at  $Re=100$  does not improve the deposition rate quantitatively but becomes more uniform along the substrate.

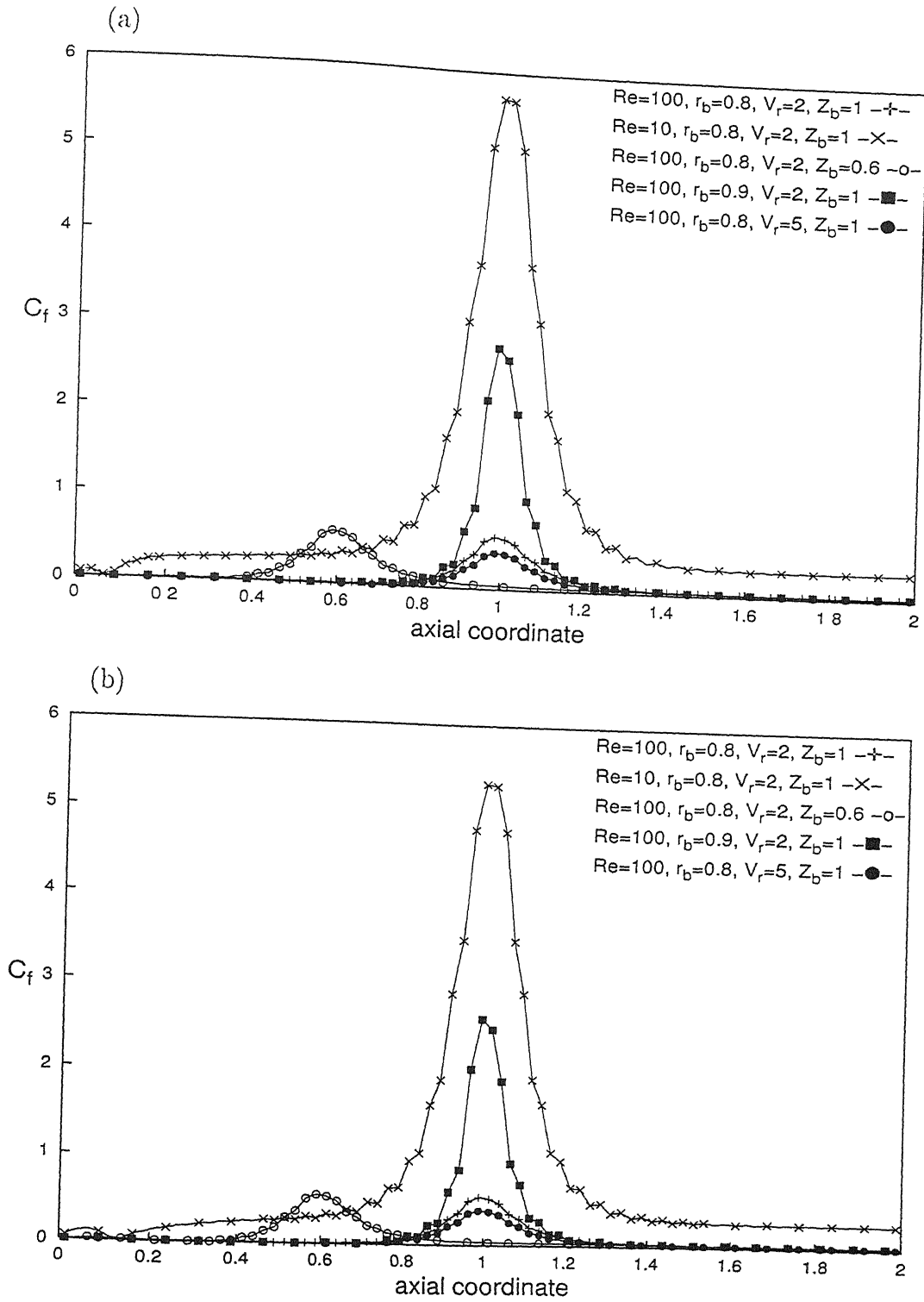


Figure 4.21: Axial variation of the skin friction coefficient on the wall of the reactor tube for the flat substrate geometry;  $\alpha = 0$  (a),  $\alpha = 30^\circ$  (b).

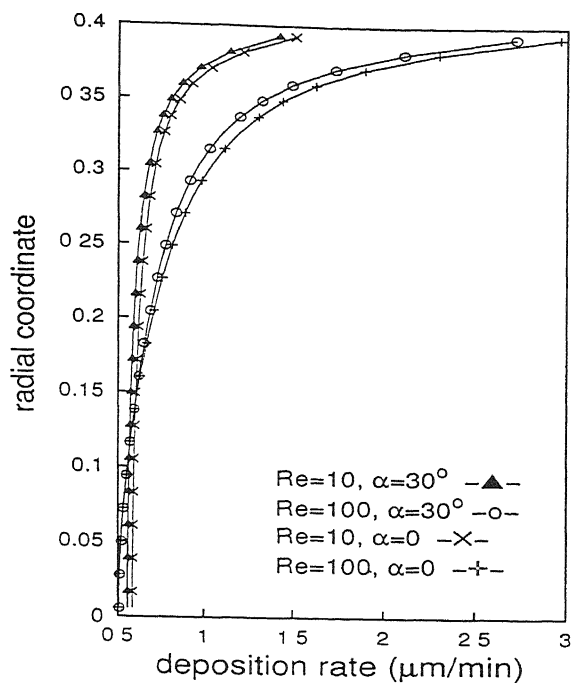
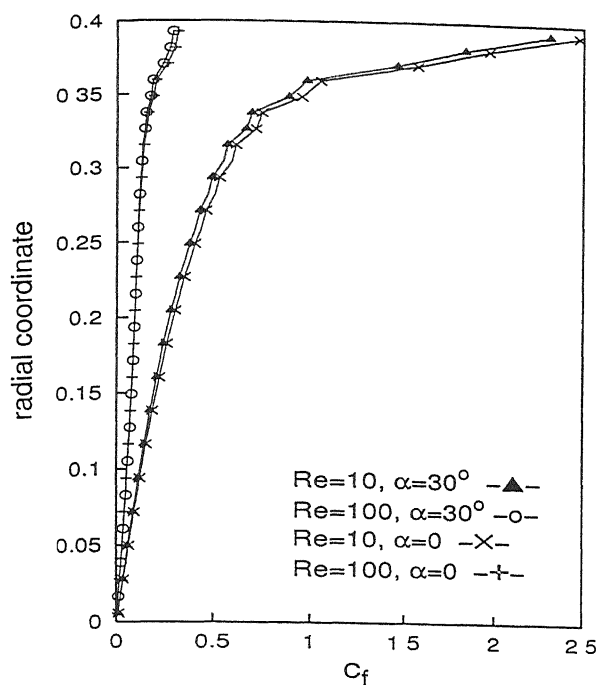


Figure 4.22: Effect of Reynolds number on the skin friction coefficient and the deposition rate on the substrate surface,  $r_b = 0.8$ ,  $V_r = 2$ ,  $Z_b = 1$ .

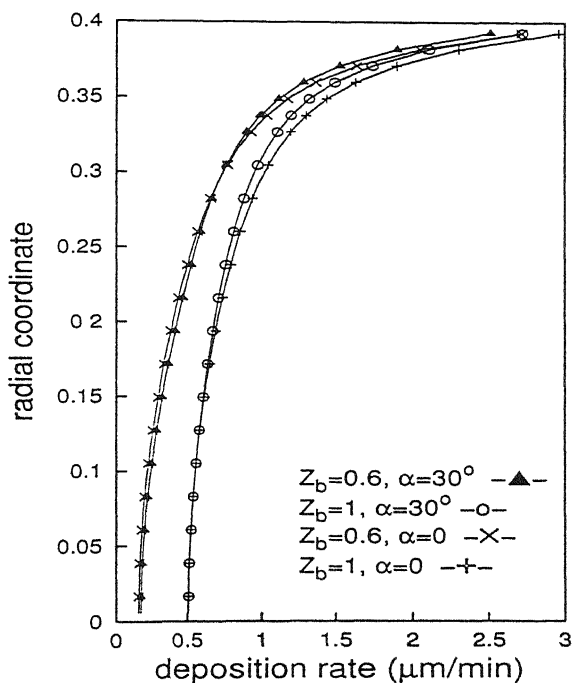
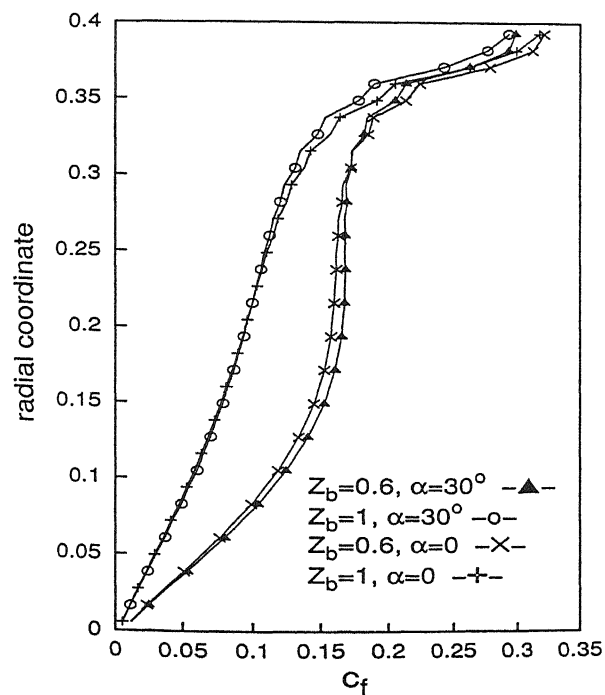


Figure 4.23: Effect of the position of the substrate on the skin friction coefficient and the deposition rate on the substrate surface,  $Re=100$ ,  $r_b = 0.8$ ,  $V_r = 2$ .

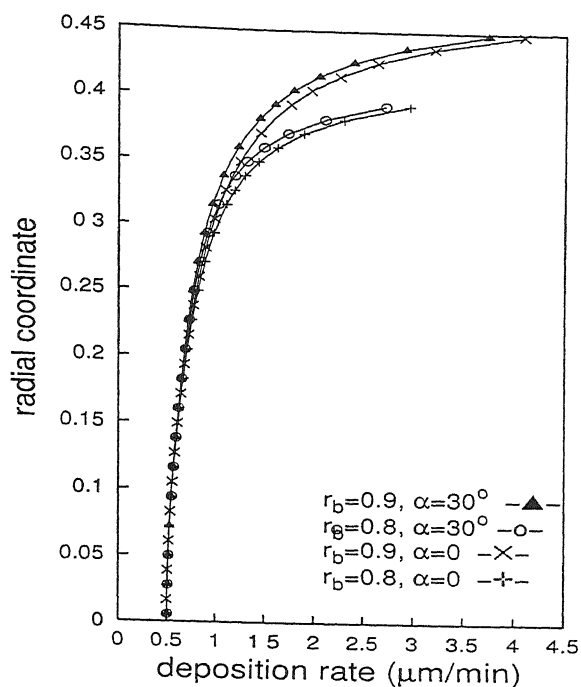
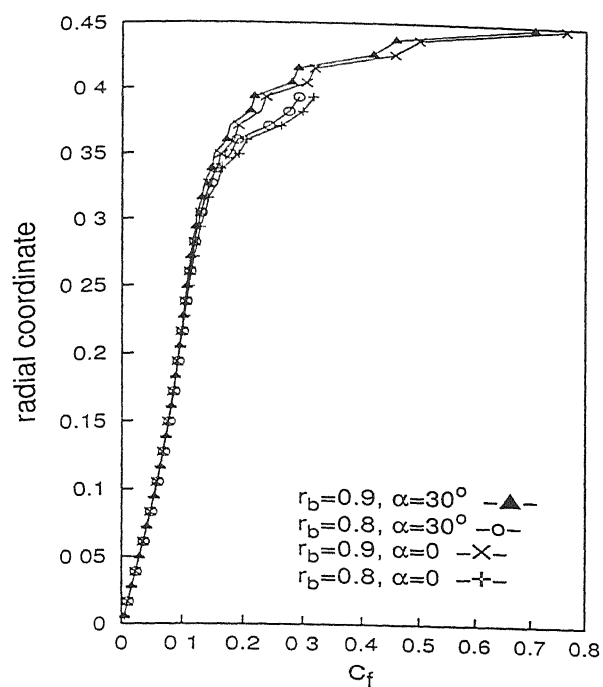


Figure 4.24: Effect of the diameter of the substrate on the skin friction coefficient and the deposition rate on the substrate surface,  $Re=100$ ,  $V_r = 2$ ,  $Z_b = 1$ .

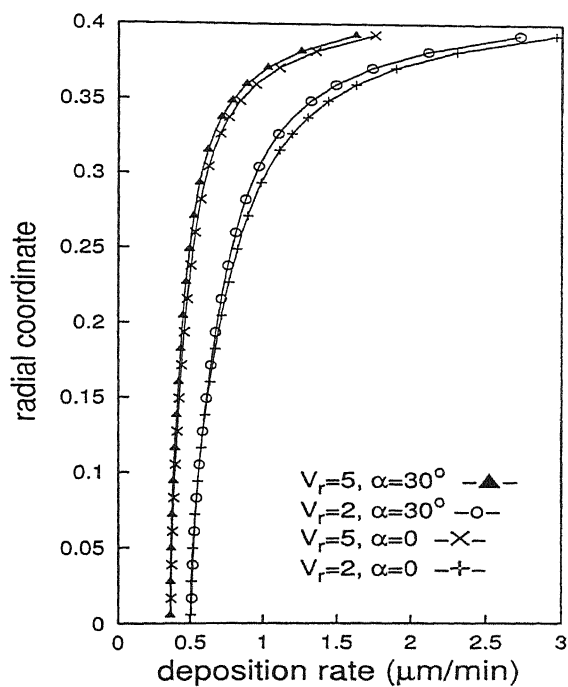
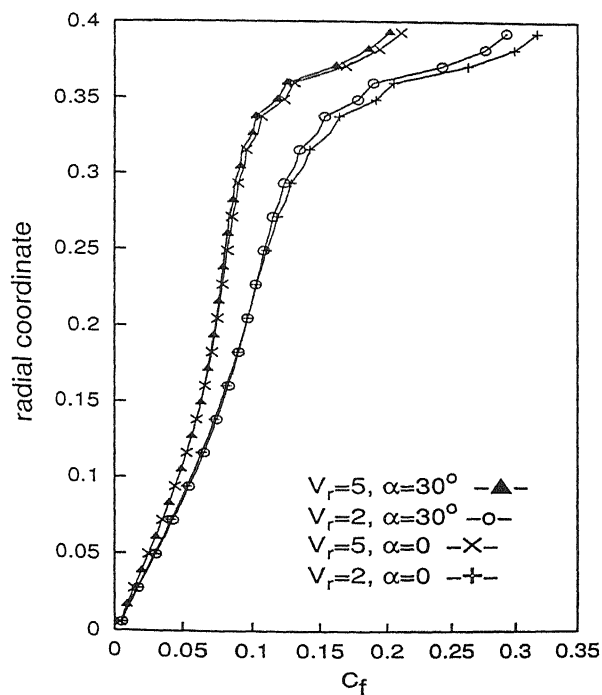


Figure 4.25: Effect of the central-to-peripheral jet velocity ratio on the skin friction coefficient and the deposition rate on the substrate surface,  $Re=100$ ,  $r_b = 0.8$ ,  $Z_b = 1$ .

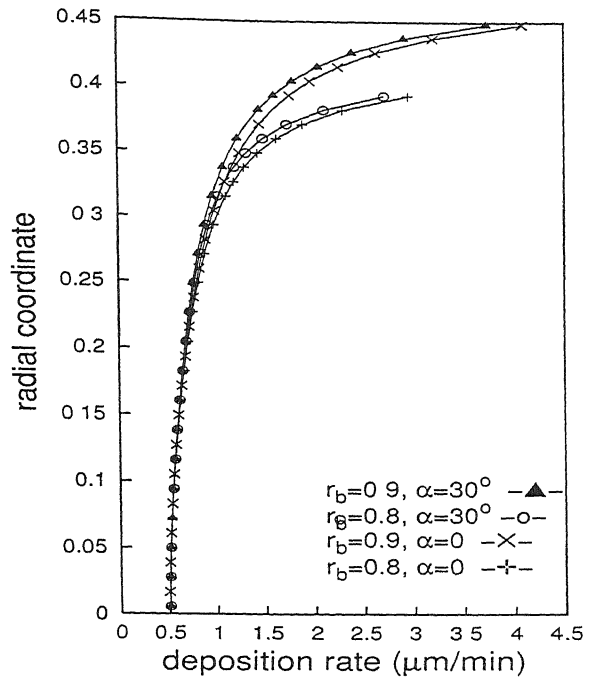
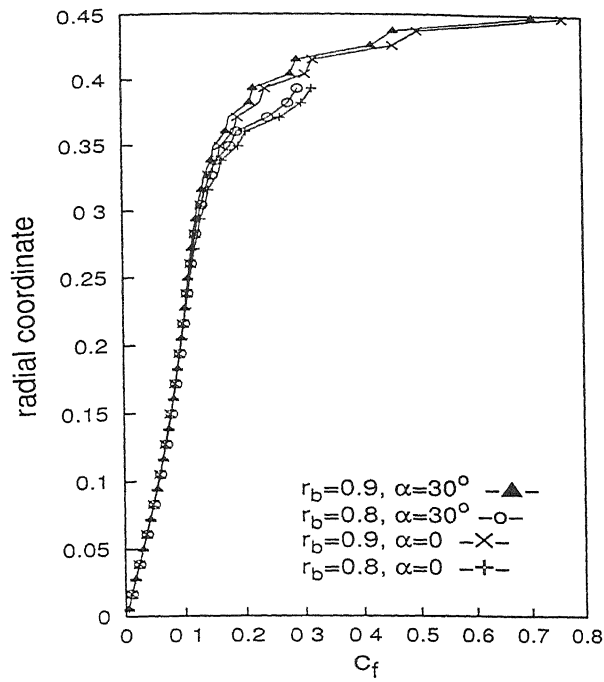


Figure 4.24: Effect of the diameter of the substrate on the skin friction coefficient and the deposition rate on the substrate surface,  $Re=100$ ,  $V_r = 2$ ,  $Z_b = 1$ .

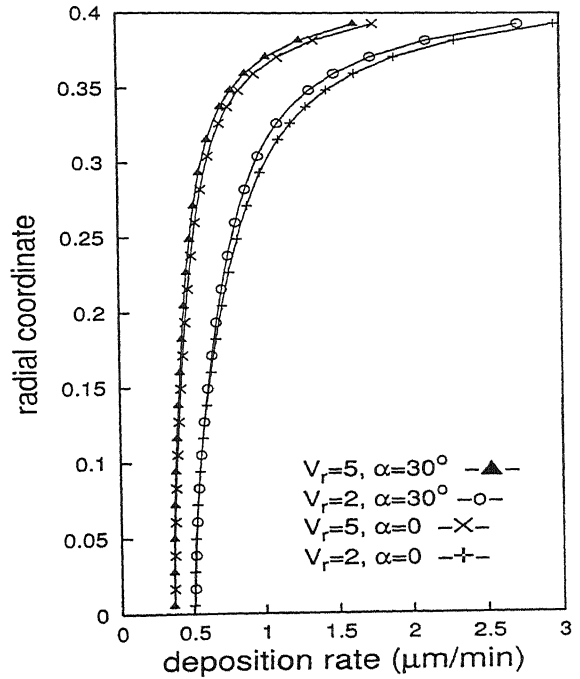
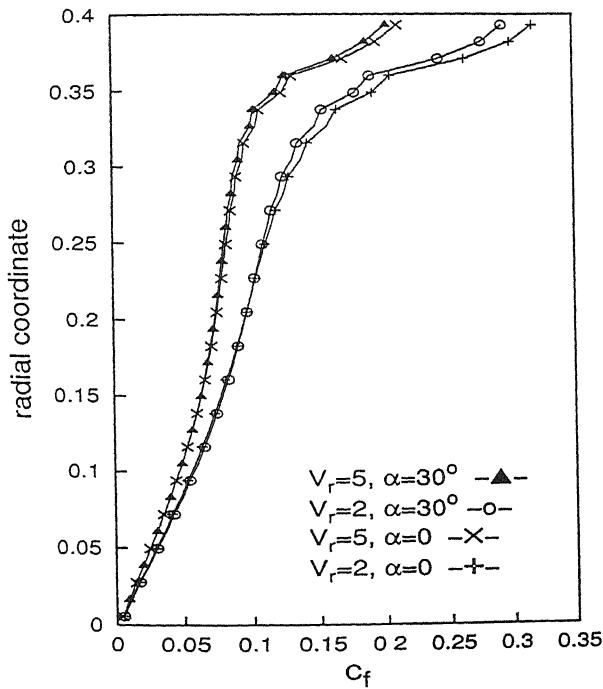


Figure 4.25: Effect of the central-to-peripheral jet velocity ratio on the skin friction coefficient and the deposition rate on the substrate surface,  $Re=100$ ,  $r_b = 0.8$ ,  $Z_b = 1$ .

### 4.2.2 Properties of a concave substrate

The shear stress distribution on the solid surfaces and the deposition characteristics on a concave substrate have been presented below. In the figures, the effect of various parameters has been depicted by varying one of them at a time with respect to the baseline case ( $Re = 100, V_r = 2, r_b = 0.8, Z_b = 1$ ).

Figure 4.26 shows the axial variation of skin friction coefficient on the reactor wall. Levels of shear stress are low and uniform along the reactor wall. A sudden increase in shear stress occurs above the substrate surface. This region moves upstream when compared to the flat substrate configuration. This is because the annular gap where fluid accelerates is located approximately at a dimensionless axial location of 0.4 from the inlet plane.

Reynolds number does not drastically alter the skin friction coefficient and the deposition rate on the substrate surface as seen in Figure 4.27. Although at a lower Reynolds number, viscous effects predominate over inertia forces, the skin friction coefficient does not show any significant variation along the substrate surface with Reynolds number. It is only near the tip of the substrate surface that the viscous effect is felt and shear stresses are relatively higher for  $Re=10$ .

There is a reduction in the shear stress at the tip of the substrate at both Reynolds numbers. The result does not match the flat substrate profile. One reason for this trend could be the numerical treatment of the corner cells. As zero penetration of mass has been implemented as the boundary condition, local tangential velocity is nonzero at the cell faces. This leads to a reduction in the velocity gradient and a lowering of the shear stress.

Figures 4.28 shows the distribution of skin friction coefficient and the deposition rate on the substrate surface for a block position of  $Z_b = 0.6$ . As the substrate is placed closer to the inlet plane, the velocity front from the central jet completely reaches the substrate and the size of the stagnation zone decreases. This leads to higher velocity near the substrate and consequently higher shear stresses. Due to the concavity of the substrate surface, appreciable negative axial velocity occurs when the bulk of the fluid is diverted along the substrate. The evolution of the negative axial velocity retards zinc sulphide particles in their movement towards the substrate surface. The stagnation zone in the immediate vicinity of the surface helps the diffusing species to overcome the convective effect and deposit on the substrate. It should be noted that the growth rate profile and

the shear stress distribution at the tip of the substrate follow closely the trends for a flat substrate. This emphasizes the role of species diffusion in deposition with respect to the bulk convection of the fluid.

Figure 4.29 shows the effect of increasing the diameter of the substrate and hence the blockage ratio. Both skin friction coefficient and the deposition rate on the substrate surface do not vary significantly along the substrate surface. This is similar to what happens in the case of a flat substrate. Only a slight deviation of the shear stress and growth rate is observable at the tip of the substrate. This result has also been discussed in context of the flat substrate. A minor variation in the shear stresses and the deposition profile along the substrate surface for different blockage ratios shows that increasing the diameter of the substrate does not alter the flow field or the deposition characteristics. Figure 4.26 shows the axial variation of the skin friction coefficient on the reactor wall for a blockage ratio. At a higher blockage, the shear stress is higher due to an increase in the velocity gradient at the substrate tip. This occurs due to the acceleration of the fluid stream passing through the narrow annular gap.

The effect of the central-to-peripheral jet velocity ratio on the shear stress distribution and the growth rate are depicted in Figure 4.30. No deviation in the shear stress and the deposition rate is observed with respect to the flat substrate configuration for a given set of parameters. The deposition profile for the two velocity ratios are identical in nature. Due to the longer reaction zone at a higher velocity ratio, a greater amount of zinc sulphide reaches the substrate, thus increasing the average level of deposition. The axial distribution of the skin friction coefficient on the reactor wall for a higher velocity ratio is shown in Figure 4.26. The values of shear stress are nearly equal everywhere except in the annular gap at the substrate location. With a higher peripheral jet velocity a greater amount of flow occurs through the annulus leading to a slight increase in the velocity gradient.

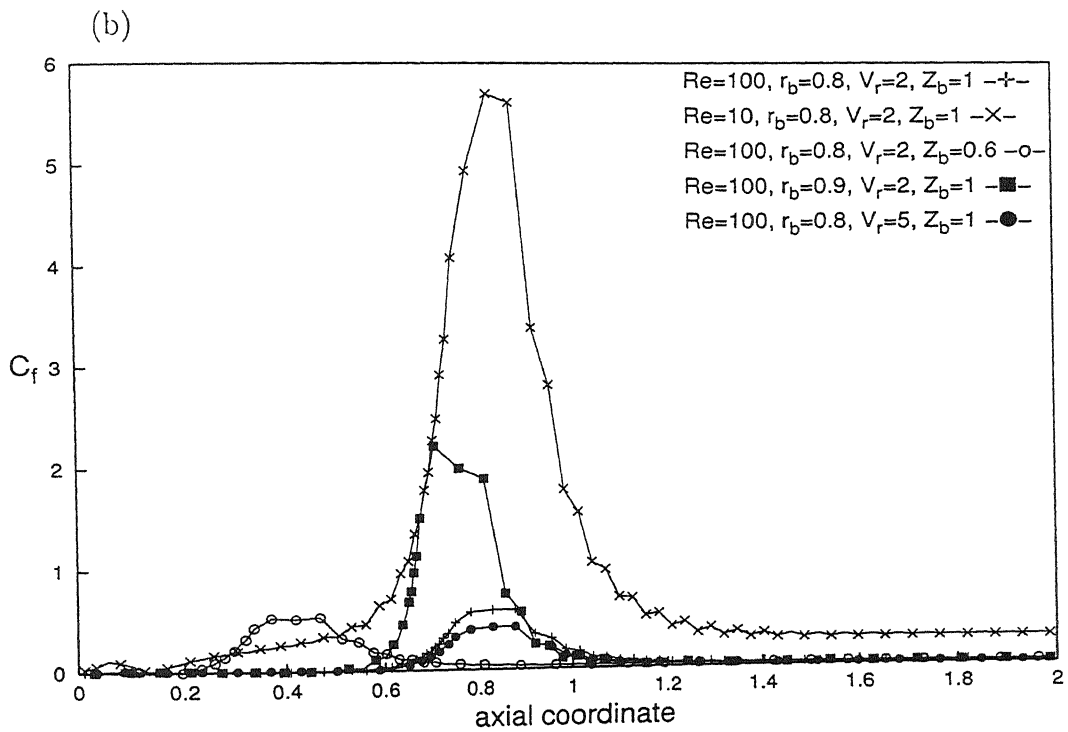
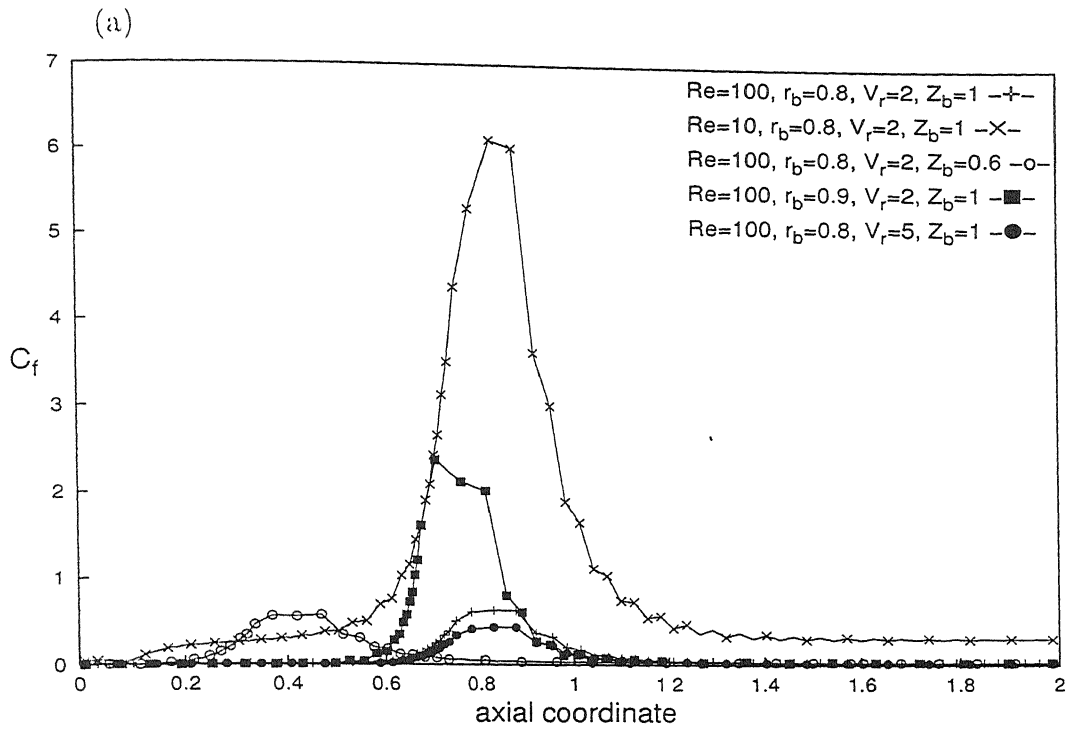


Figure 4.26: Axial variation of skin friction coefficient on the reactor wall for the concave substrate geometry;  $\alpha = 0$  (a),  $\alpha = 30^\circ$  (b).



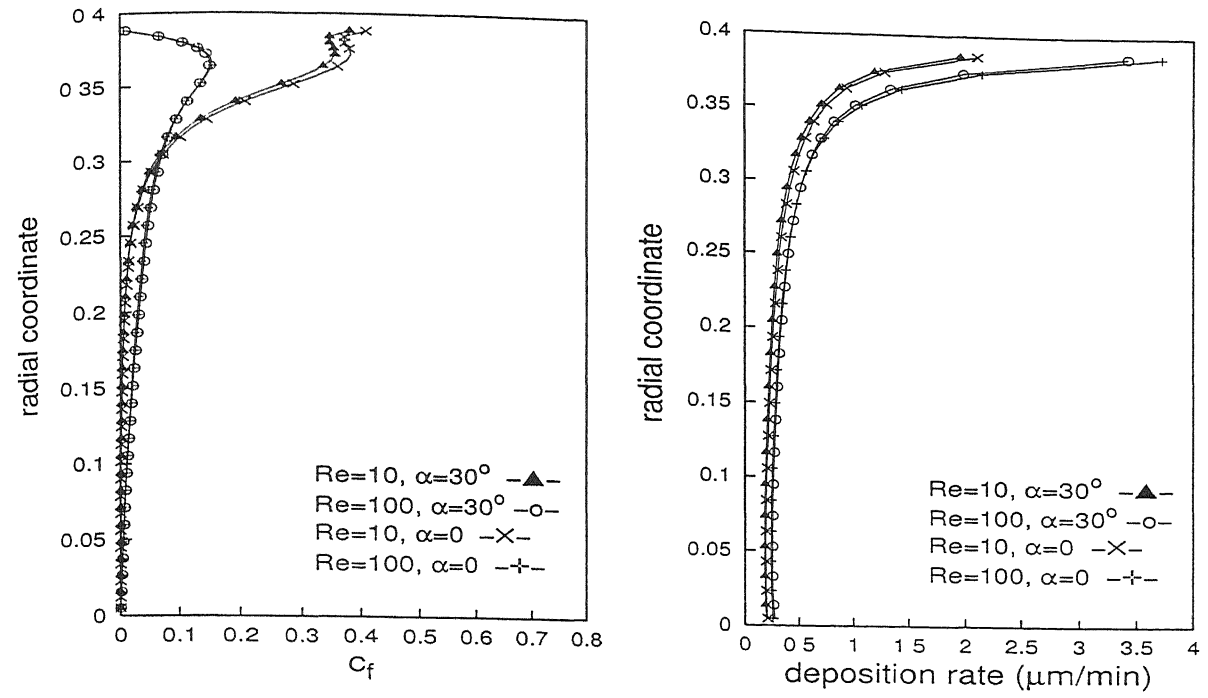


Figure 4.27: Effect of Reynolds number on the skin friction coefficient and the deposition rate on the substrate surface,  $r_b = 0.8$ ,  $V_r = 2$ ,  $Z_b = 1$ .

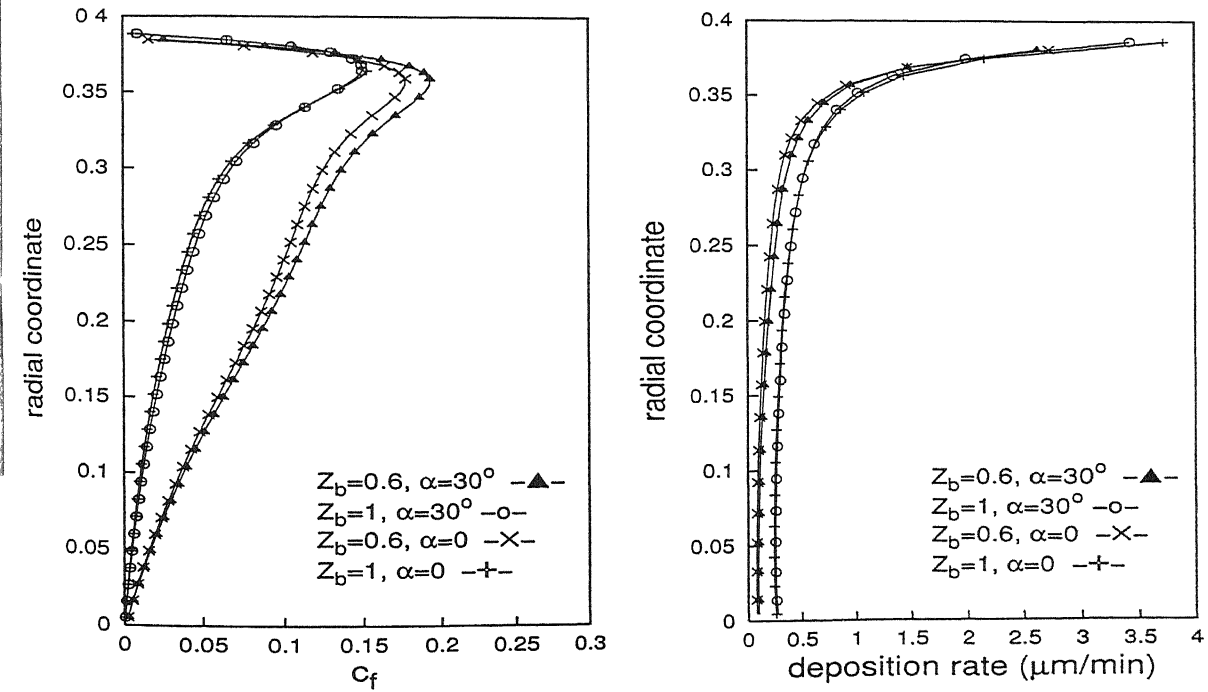


Figure 4.28: Effect of the position of the substrate on the skin friction coefficient and the deposition rate on the substrate surface,  $Re=100$ ,  $r_b = 0.8$ ,  $V_r = 2$ .

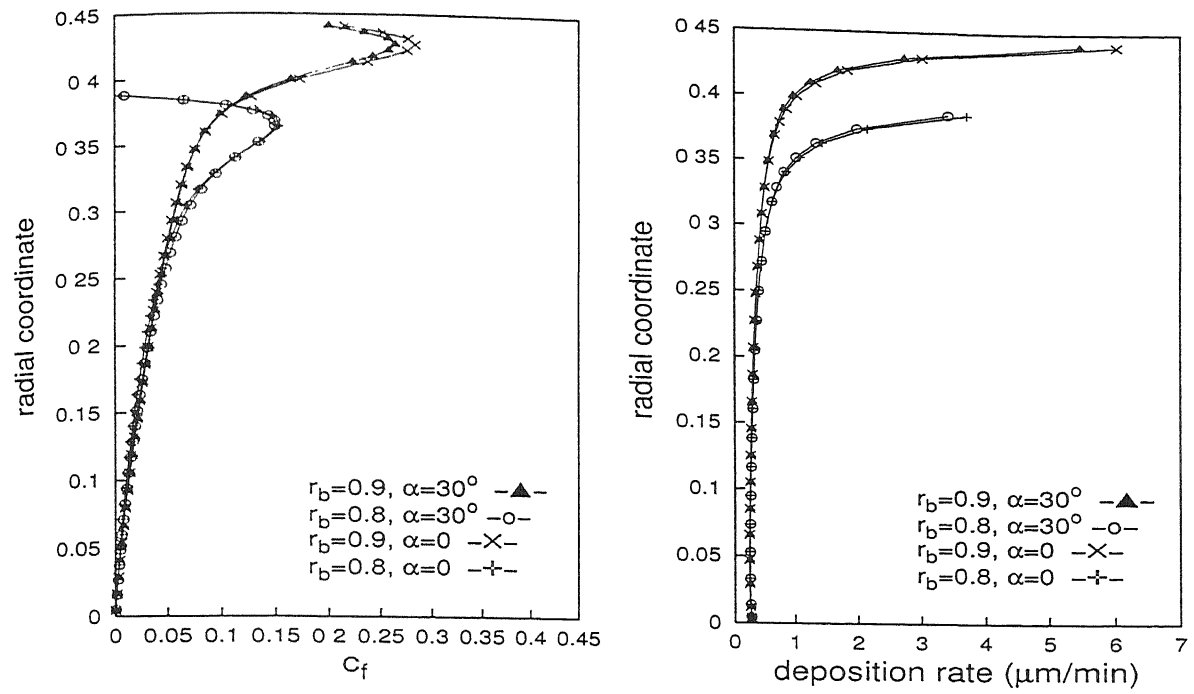


Figure 4.29: Effect of the diameter of the substrate on the skin friction coefficient and the deposition rate on the substrate surface,  $Re=100$ ,  $V_r = 2$ ,  $Z_b = 1$ .

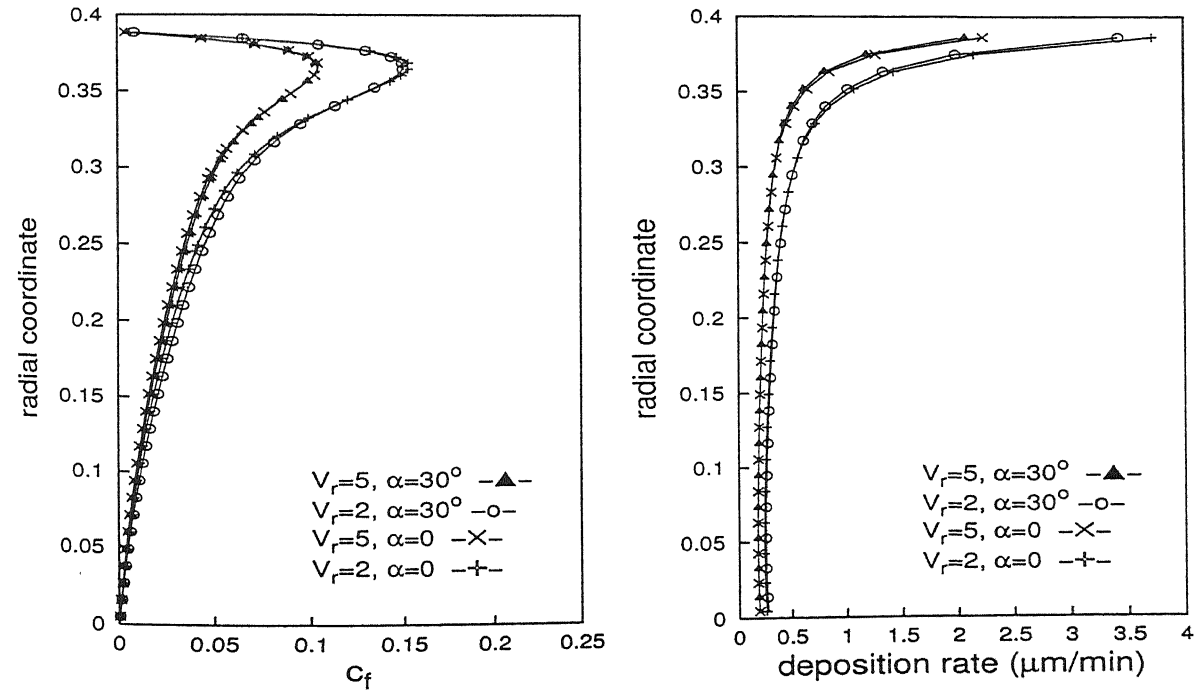


Figure 4.30: Effect of the central-to-peripheral jet velocity ratio on the skin friction coefficient and the deposition rate on the substrate surface,  $Re=100$ ,  $r_b = 0.8$ ,  $Z_b = 1$ .

## 4.3 Evaluation of alternative geometries

In this section limited results for the alternative geometries have been presented. The schematic views of these geometries are shown Figures 1.5(a) and 1.5(b) of Chapter 1. The first of these geometries consists of a substrate whose surface is convex facing the main flow direction. The second has coaxial jets with  $H_2S$  and  $Zn$  are injected through the central and the annular nozzle respectively. It is expected that when the convex surface of the substrate faces the flow significant changes in the flow distribution occur, in turn leading to different deposition characteristics. The coaxial geometry is expected to extend the size of the reaction zone towards the substrate and once again improves the deposition characteristics of the CVD reactor.

### 4.3.1 Flow and concentration fields with a convex substrate

In this section the flow and the concentration fields have been discussed with the parameters set at  $Re = 100$ ,  $V_r = 2$ ,  $r_b = 0.8$ ,  $Z_b = 1$  and  $\alpha = 30^\circ$ . The significant contours of species distribution, their consumption rates and production rates have been shown. This approach has retained the clarity of the figures.

The baseline case employed for comparison of different parameters is identical to that of the concave substrate configuration ( $Re = 100$ ,  $V_r = 2$ ,  $r_b = 0.8$ ,  $Z_b = 1$  and  $\alpha = 30^\circ$ ). Figure 4.31 shows the flow and concentration fields for the baseline configuration. Due to the convexity of the substrate surface the stagnation zone is seen to disappear. The geometric shape of the substrate aids the fluid stream to reach closer to the solid surface. This is an important difference with respect to the previous geometries. The expansion of the central jet occurs up to a greater distance downstream compared to the previous geometries. Moreover, uniformity of the velocity at the central zone of the reactor is improved, leading to enhanced transport of the species. The shape and size of the recirculation pattern however do not change. This is because the presence of the peripheral jet that confines it in the cross-stream direction, restricting it to the corner of the reactor. The flow field near the inlet plane remains unaltered as the geometry of the substrate does not propagate sufficiently upstream against

the momentum of the central jet. This leads to a reaction zone of almost the same length as the reactor with a concave substrate. The distribution of zinc is similar to that of the concave block due to the absence of any changes in the flow field near the inflow plane. The region rich in zinc sulphide is located at the same position and its size and shape also do not change. This emphasizes that at low Reynolds numbers it is the basic flow field that controls the transport of the species. Changes in the shape of the substrate do not alter the flow field due to the presence of the strong central jet.

Figure 4.32 shows the flow field and species distribution for the case of substrate being placed closer to the inflow plane. The stagnation zone reduces even further compared to the case of  $Z_b = 1$ . Expansion of the central jet occurs quite smoothly due to the absence of negative axial velocity near the substrate surface. Levels of velocity near the substrate are higher compared to the two earlier geometries. Severe non-uniformities in the velocity profile in the central zone observed in the case of a concave substrate are absent here. This is due to the convexity of the substrate that allows the fluid stream to pass by the substrate without moving upstream. The recirculation zone does not change in shape and size with respect to the block position of  $Z_b = 1$ . Upward stretching of the reaction envelope towards the annular gap here is a favorable feature. Thus the transport of the species occurs in the stream-wise direction towards the substrate. The distribution of zinc shows that the species-rich regions do not get compressed by the backflow of the bulk fluid. This adverse effect was weakness of the concave substrate. The zinc sulphide-rich zone increases in size and is a continuous layer because the reduced upstream diffusion of momentum does not interrupt the mixing. This shows smooth mixing of the two fluid streams injected through the central and peripheral jets for the present geometry has been accomplished.

Figure 4.33 shows the results for a central-to-peripheral jet velocity ratio of  $V_r = 1$ . Velocity levels inside the reactor increases while the cross-stream velocity is small everywhere. This is due to the fact that the fluid stream injected through the peripheral jet has a higher momentum and flows in the axial direction after meeting the central jet. It can be noted that the mixing interface is flat and spreads in the stream-wise direction. This region also advances towards the substrate leading to an enhanced transport of the species. With the increase in the velocity of the peripheral jet, the reaction envelope stretches to almost twice the distance compared to the higher jet velocity ratio. The distribution of

zinc sulphide is also favourable for deposition compared to a higher peripheral jet velocity. Due to the longer reaction zone in the stream-wise direction, the shape of the zinc sulphide-rich zone also changes. This zone is increasingly parallel to the reactor axis compared to the case of a lower peripheral jet velocity where it spreads in the cross-stream direction. This is a feature which is desirable since the growth rate is expected to increase and results in lower material losses.

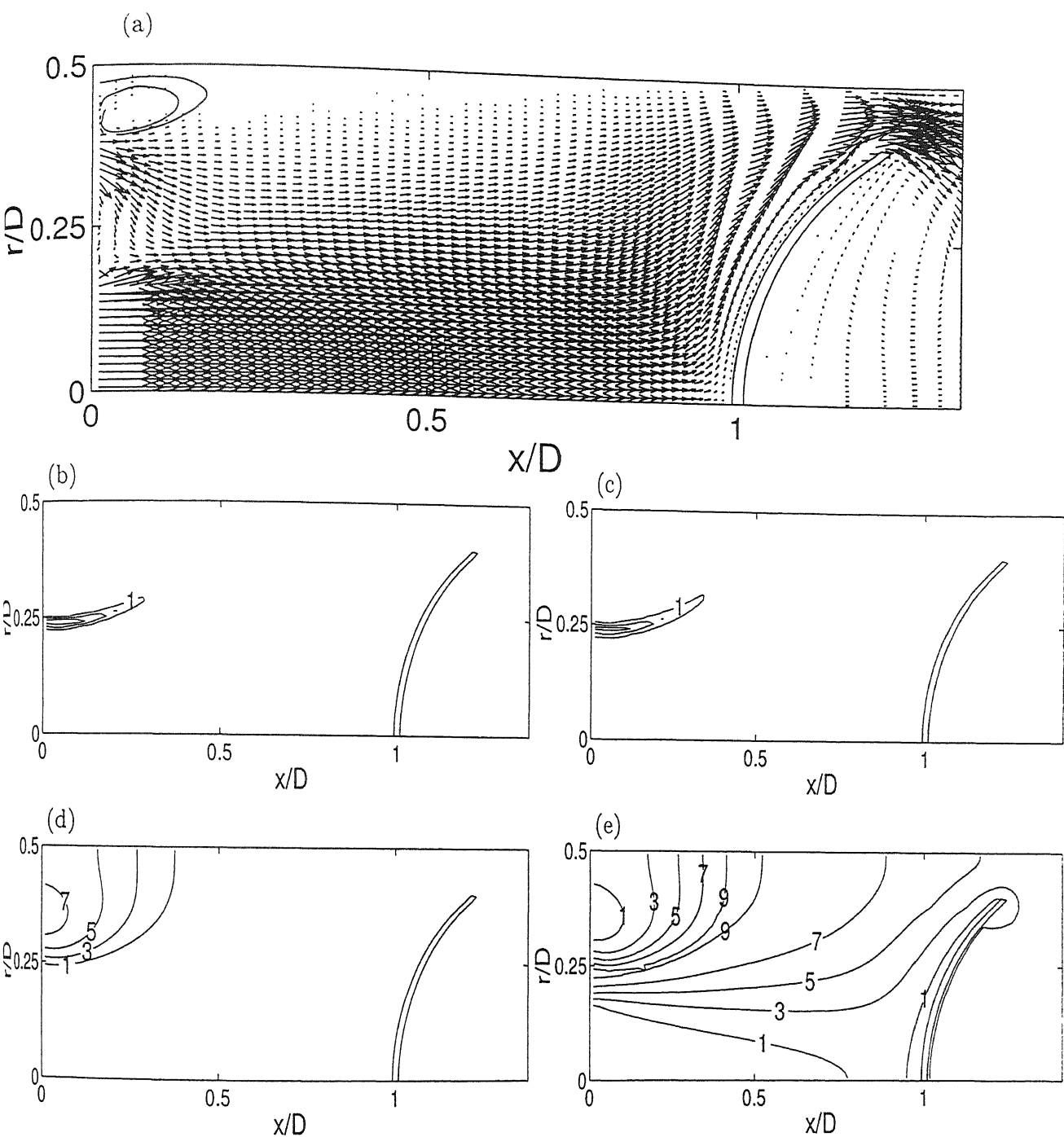


Figure 4.31: Velocity vectors (a), steady state contours of consumption rate of Zn (b), steady state contours of production rate of ZnS (c), contours of mass fraction of Zn (d), contours of mass fraction of ZnS (e), Baseline configuration:  $Re=100$ ,  $V_r = 2$ ,  $r_b = 0.8$ ,  $\alpha = 30^\circ$  inwards,  $Z_b = 1$

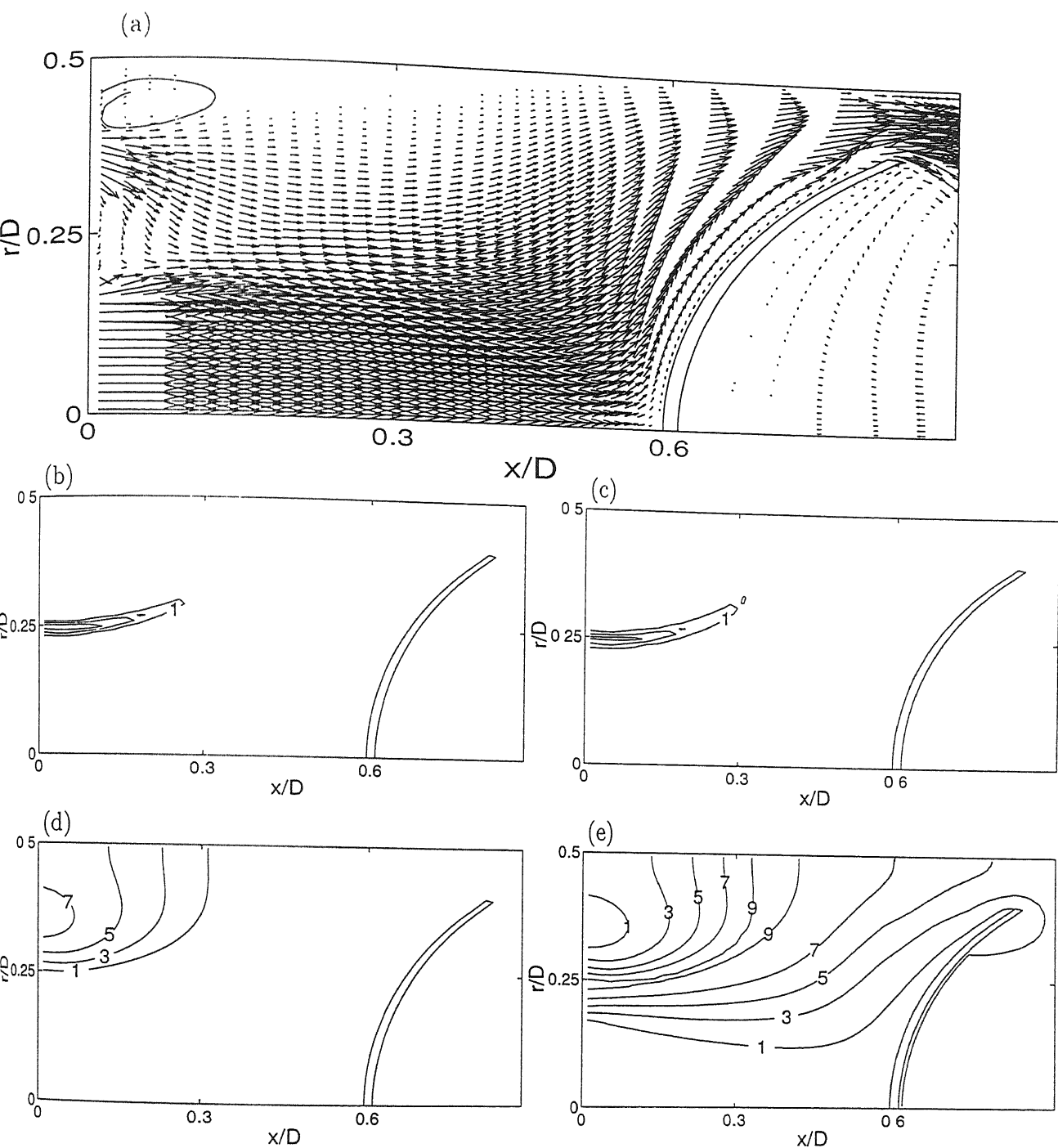


Figure 4.32: Velocity vectors (a), steady state contours of consumption rate of Zn (b), steady state contours of production rate of ZnS (c), contours of mass fraction of Zn (d), contours of mass fraction of ZnS (e),  $Re=100$ ,  $V_r = 2$ ,  $r_b = 0.8$ ,  $\alpha = 30^\circ$  inwards,  $Z_b = 0.6$

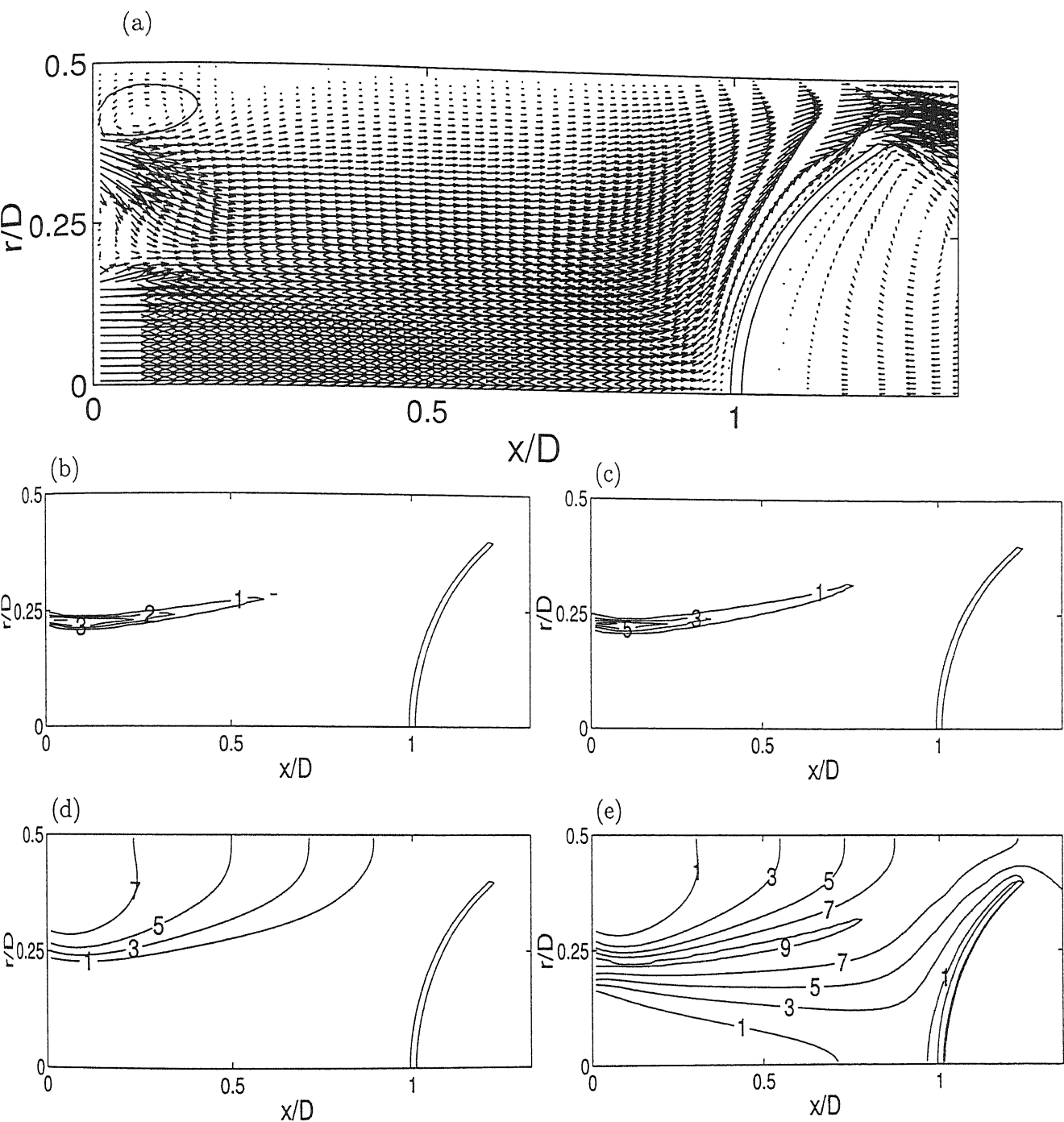


Figure 4.33: Velocity vectors (a), steady state contours of consumption rate of Zn (b), steady state contours of production rate of ZnS (c), contours of mass fraction of Zn (d), contours of mass fraction of ZnS (e),  $Re_{\infty}=100$ ,  $V_r = 1$ ,  $r_b = 0.8$ ,  $\alpha = 30^\circ$  inwards,  $Z_b = 1$



### 4.3.2 Flow and concentration fields with coaxial jets

For the coaxial jet configuration the parameters considered are:  $Re = 100$ ,  $V_r = 1, 2$ ,  $r_b = 0.8$ ,  $Z_b = 1, 0.6$ . Calculations have been carried out with a concave substrate.

Figure 4.34 shows the flow and species concentration fields for the baseline case of  $Re = 100$ ,  $V_r = 2$ ,  $r_b = 0.8$ ,  $Z_b = 1$ . The central jet does not expand freely due to the confining effect of the peripheral jet. Mixing starts at the inlet plane as the jets meet after their injection. The recirculation region is stronger as the peripheral jet has been moved towards the axis of the reactor. This region is at a small angle with the axial direction, thus revealing a gradual expansion of the peripheral jet. The strong recirculating flow brings a certain portion of the zinc stream to the vicinity of the inlet plane. But as the initial zinc stream envelopes the central jet only a fraction of the recirculated zinc particles react with hydrogen sulphide. The shear between the two jets at their interface leads to vigorous and accelerated mixing. The reaction zone is thus limited to a small distance from the inlet plane. A secondary zinc sulphide production zone is observed at the boundary of the peripheral jet and is attached to the inflow plane. This is due to the reaction between zinc particles moving in the recirculation zone and traces of hydrogen sulphide available in the vicinity of the inlet plane. Zinc is distributed in the region very close to the inlet plane, the reason being the accelerated mixing and spontaneous reaction of the injected species. The regions of large zinc sulphide which show the zone of mixing with the most favourable stoichiometry is almost reduced to a point. This again emphasizes the adverse role of the accelerated mixing and reaction on the zinc sulphide distribution.

Figure 4.35 shows the flow and concentration fields for the case of coaxial jets when the substrate is placed closer to the inflow plane. The shape of the recirculation pattern is now different and is closer to being circular. The effect of concavity of the substrate surface is felt by the fluid stream at a plane closer to the injection surface and the expansion of the peripheral jet is impeded. The inflexion point in the velocity profile is clearly visible near the mid plane of the reactor,  $x/d = 0.3$ . The shearing effect of the two streams at their interface occurs over a shorter distance due to a closer placement of the substrate from the inflow plane. The reaction envelope is similar to the baseline case, where  $Z_b = 1$ . The secondary zinc sulphide production zone however increases in size

and mixes with the primary zone. Also a secondary zinc consumption zone is visible. This shows that the recirculatory flow is stronger in the present case owing to a sharper variation of the axial velocity in the cross-stream direction compared to the baseline case ( $Z_b = 1$ ). The distribution of zinc shows that the zinc-rich zone is compressed owing to greater amount of reaction with hydrogen sulphide. The maximum zinc sulphide-rich zone stretches towards the reactor axis. These zones were practically a point for the baseline case. Thus with the substrate placed nearer to the inlet plane, strong recirculating current increases the reaction between the trace quantities of hydrogen sulphide and the recirculated zinc in the secondary mode, leading to a larger volume where the zinc sulphide concentration is quite high.

Figure 4.36 shows results when the central-to-peripheral jet velocity ratio  $V_r$  is reduced to unity. The recirculation pattern is similar in shape, size and position to the baseline case of  $V_r = 2$ . The shearing effect at the jet interface decreases as their velocities are now equal. A velocity profile at any cross-section is smoother, and strong gradients are absent. The reduction in shear between the two streams leads to gradual mixing followed by reactions. This is manifested in the increased extent of the reaction zone. Zinc consumption rate and in turn zinc sulphide production rate significantly increases. Quantitatively they are almost five times the rates for the baseline case of  $V_r = 2$ . The gradual mixing of the two streams leads to a reaction zone that spreads in the stream-wise direction pointing towards the substrate. The region rich in zinc increases due to the higher peripheral jet velocity as well as its free expansion. This is aided by the absence of a strong backflow that occurs at a block position of  $Z_b = 0.6$ . The size of the maximum zinc sulphide region also increases due to the gradual mixing of the streams over a longer downstream distance from the inflow plane.

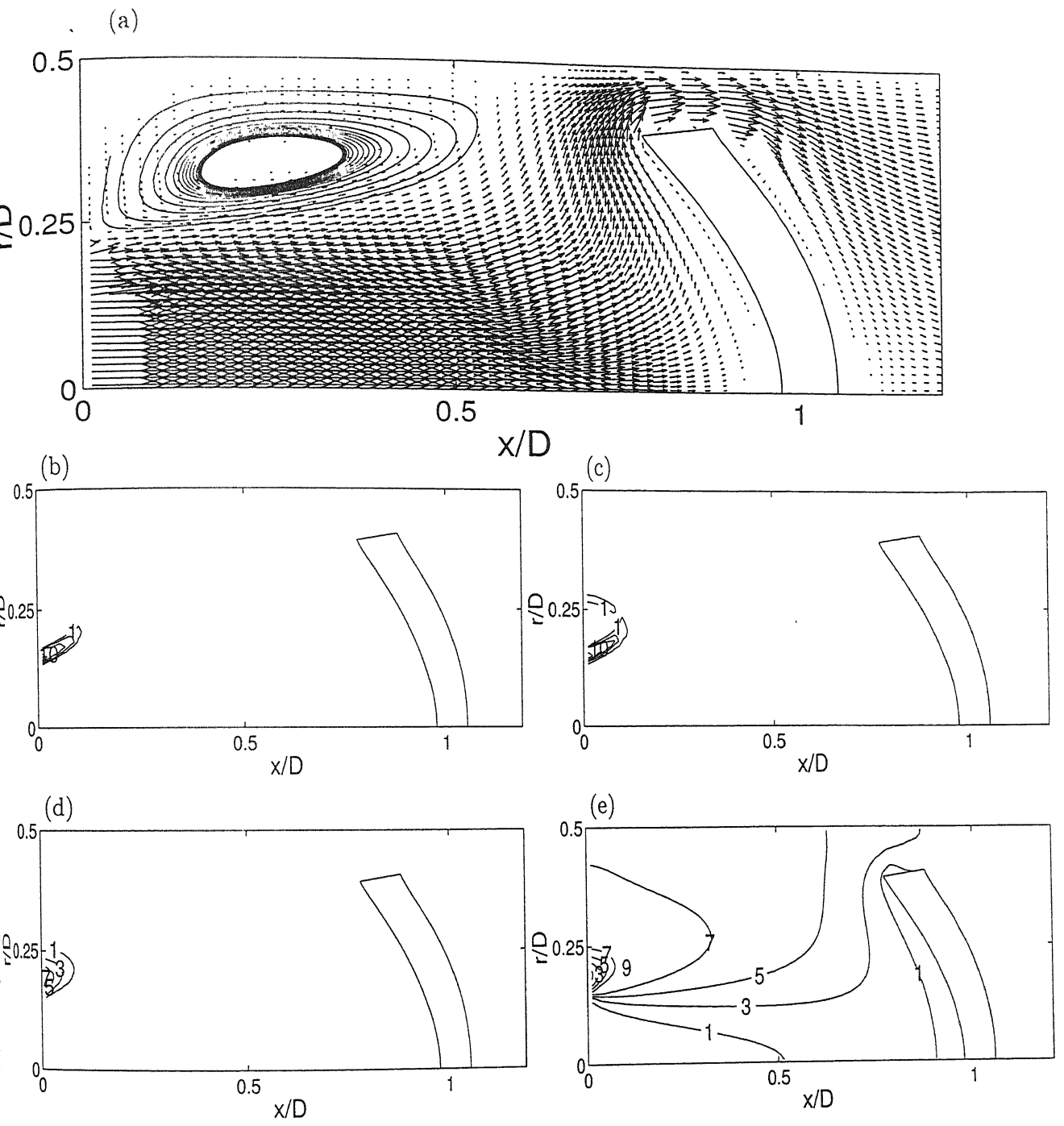


Figure 4.34: Velocity vectors (a), steady state contours of consumption rate of Zn (b), steady state contours of production rate of ZnS (c), contours of mass fraction of Zn (d), contours of mass fraction of ZnS (e), Baseline configuration:  $Re=100$ ,  $V_r = 2$ ,  $r_b = 0.8$ ,  $\alpha = 0$ ,  $Z_b = 1$

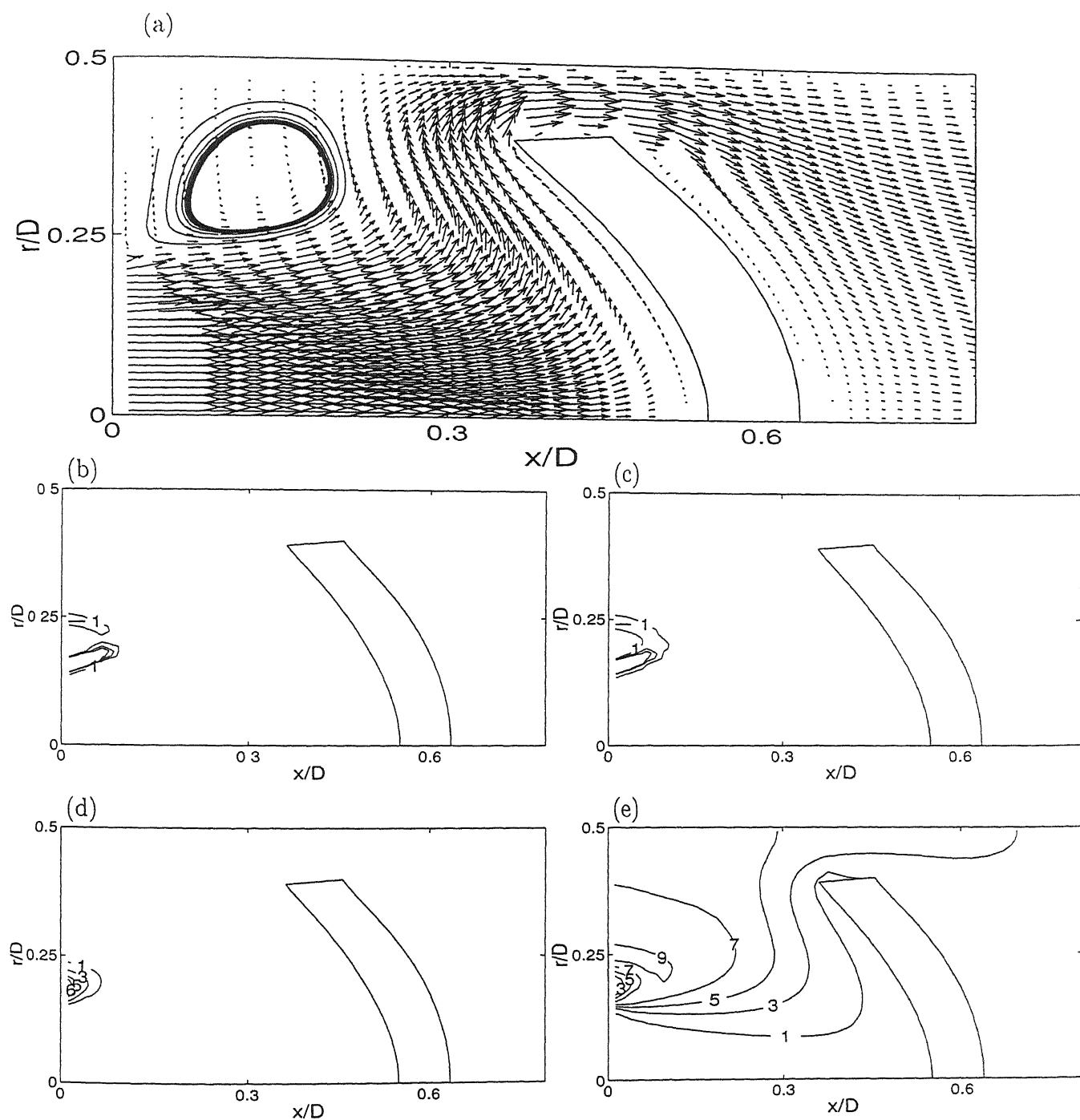


Figure 4.35: Velocity vectors (a), steady state contours of consumption rate of Zn (b), steady state contours of production rate of ZnS (c), contours of mass fraction of Zn (d), contours of mass fraction of ZnS (e),  $Re=100$ ,  $V_r = 2$ ,  $\tau_b = 0.8$ ,  $\alpha = 0$ ,  $Z_b = 0.6$

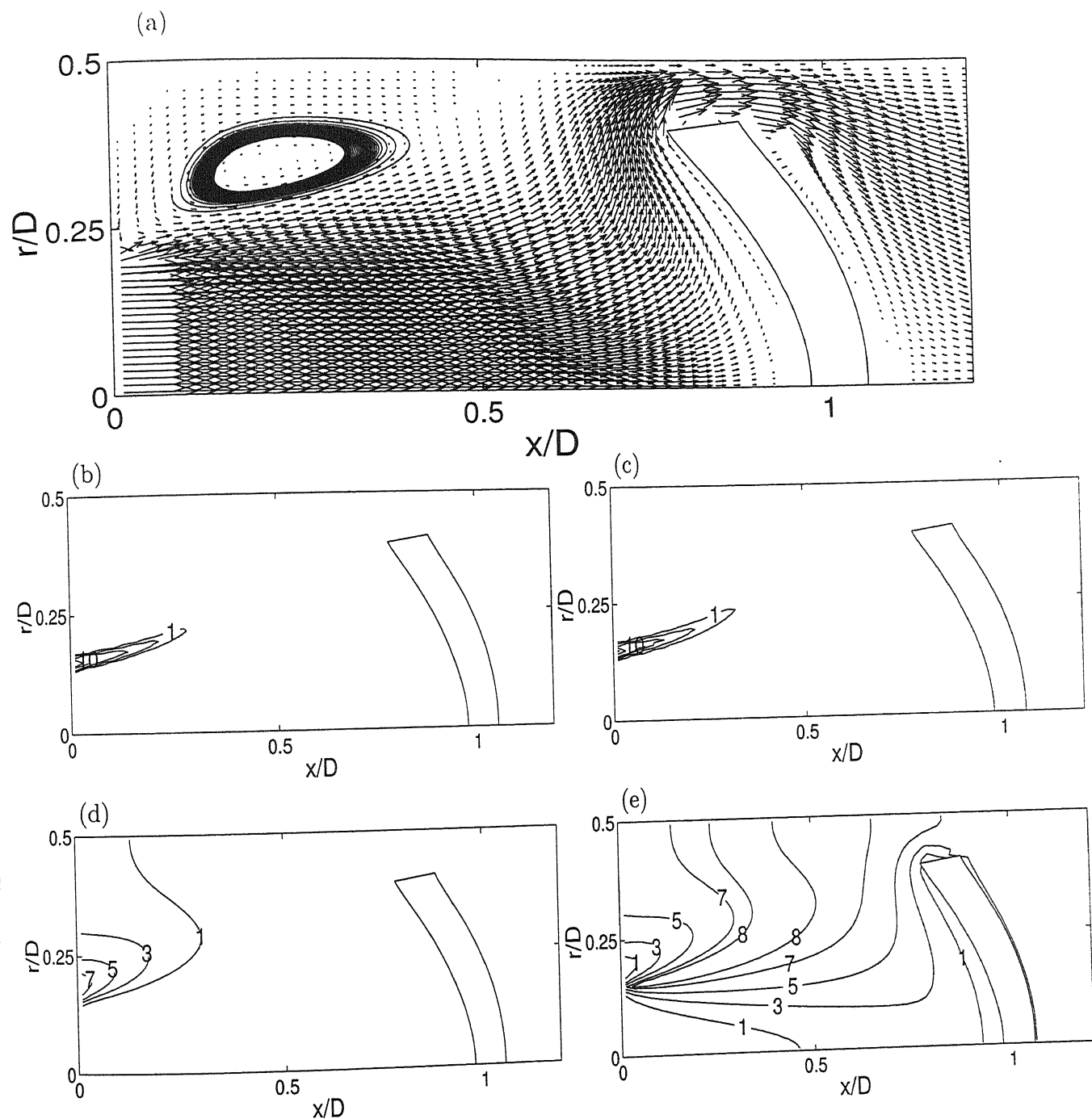


Figure 4.36: Velocity vectors (a), steady state contours of consumption rate of Zn (b), steady state contours of production rate of ZnS (c), contours of mass fraction of Zn (d), contours of mass fraction of ZnS (e),  $Re=100$ ,  $V_r = 1$ ,  $r_b = 0.8$ ,  $\alpha = 0$ ,  $Z_b = 1$

### 4.3.3 Wall shear stress and Deposition rate Profiles for a convex substrate

Distributions of the skin friction coefficient and the deposition rate on the substrate surface have been presented in this section. Also skin friction coefficient on the reactor wall has been shown.

Figure 4.37 shows the axial variation of the skin friction coefficient on the reactor wall. The trends are same to those of earlier geometries (Figures 4.21b and 4.26b). The values of  $C_f$  is considerably lower for the present case. The reason for this is the uniformity in the flow field. Large velocity gradients that was obtained for the flat and concave substrate geometries are absent here. The convex shape of the substrate has a streamlining effect on the flow which passes over it without moving upstream.

Figure 4.39 shows the radial variation of the skin friction coefficient and the deposition rate on the convex substrate for three sets of parameters. Shear stresses on the substrate surface are comparable for the three cases. Near the axis the shear stress is slightly higher due to higher velocity levels near the substrate surface when the block position is  $Z_b = 0.6$ . It should be noted that shear stress increases at the tip of the substrate, a result that is the reverse of what was presented for the concave surface. The explanation for this anomaly is the following. For the convex substrate the stagnation zone completely disappears leading to a considerably large velocity in the vicinity of the substrate. Thus the velocity gradient is also greater in magnitude along the surface. At the tip of the surface, the fluid stream transits from a gradual passage to a narrow annulus. This leads to acceleration in the fluid stream. It is to be noted that in the present configuration the tip of the substrate lies near the annulus. This is not the case for the concave substrate due to its finite thickness. Thus the proximity of the substrate tip and the narrow annulus results in a greater velocity gradient, and in turn the skin friction coefficient. The effect of fluid acceleration completely overwhelms the presence of a low tangential velocity related to approximate handling of the corner cells in the numerical algorithm. This issue has been discussed in the context of an increase of shear stress at the tip of the concave substrate. The distribution of the deposition rate follows the trend of shear stress on the substrate surface. Due to a higher skin friction along the substrate for a block position of  $Z_b = 0.6$ , the deposition rate is low at all the points on the substrate.

With a central-to-peripheral jet ratio  $V_r = 1$ , the growth rate is considerably higher compared to the other case of  $V_r = 2$ . This occurs due to the stretching of the reaction zone in the axial direction as a greater amount of zinc sulphide is transported to the substrate. There are no significant deviations in the axial distribution of the skin friction coefficient on the reactor wall with reference to the concave substrate geometry. This shows that the effect of the shape of the substrate is not felt in the region near the reactor wall.

#### 4.3.4 Wall shear stress and Deposition rate Profiles for coaxial jets

Figure 4.38 shows the axial variation of the skin friction coefficient on the reactor wall. The trends are similar to the earlier case (Figure 4.37). The peaks of the shear stress distribution are now different. Due the changes in the direction of curvature of the substrate surface, the position of the annular region between the substrate tip and the reactor wall is different for the two cases. Thus maximum shear stress occurs at a different axial location for the two geometries (Figure 4.37 and 4.38). The values of  $C_f$  for the present case is smaller than the cases considered in section 4.2. This is due to the fact that for a coaxial jet configuration both the central and the peripheral jets constitute the bulk flow, leading to a uniformity in the velocity field.

Figure 4.40 shows the variation of the skin friction coefficient and the deposition rate on the substrate surface for the coaxial jet configuration. The slope of the shear stress along the surface is higher for the three sets of parameters studied. This is due to a greater uniformity of the flow field. Skin friction coefficient is also higher for the case when the substrate is placed closer to the inflow plane. In this configuration, the streams from the central and the peripheral jet constitute the bulk flow. As a greater amount of fluid stream passes over the substrate that has a poor streamline shape, an appreciable amount of shear and hence skin friction occurs along the surface. The values of the skin friction coefficient are comparable with the configuration when the jets are separated by a certain distance. A reduction in the shear stress is observed at the tip of the substrate. This has been pointed out in the discussions for the concave substrate and jets that are not coaxial. For the present simulation, the deposition rate along the surface is quite uniform (Figure 4.40). But the increase in the growth rate at the tip of the

substrate continues to occur. This feature has also been observed for the concave substrate with separated jets. The deposition rate of zinc sulphide is higher at all the points on the substrate due to the axial alignment of the reaction zone. The deposition rates for the other two sets of parameters are also close. Thus for a coaxial jets configuration, the uniformity of the central and peripheral jet velocities is favourable for a uniform as well as higher levels of the deposition rate. The axial variation of the skin friction coefficient on the reactor wall is shown in Figure 4.38. The trend is similar to the earlier geometries studied in section 4.2. Only a slight variation is observed in the region between the inlet plane and the substrate. The variation is due to the backflow near the reactor tube wall for the present geometry.



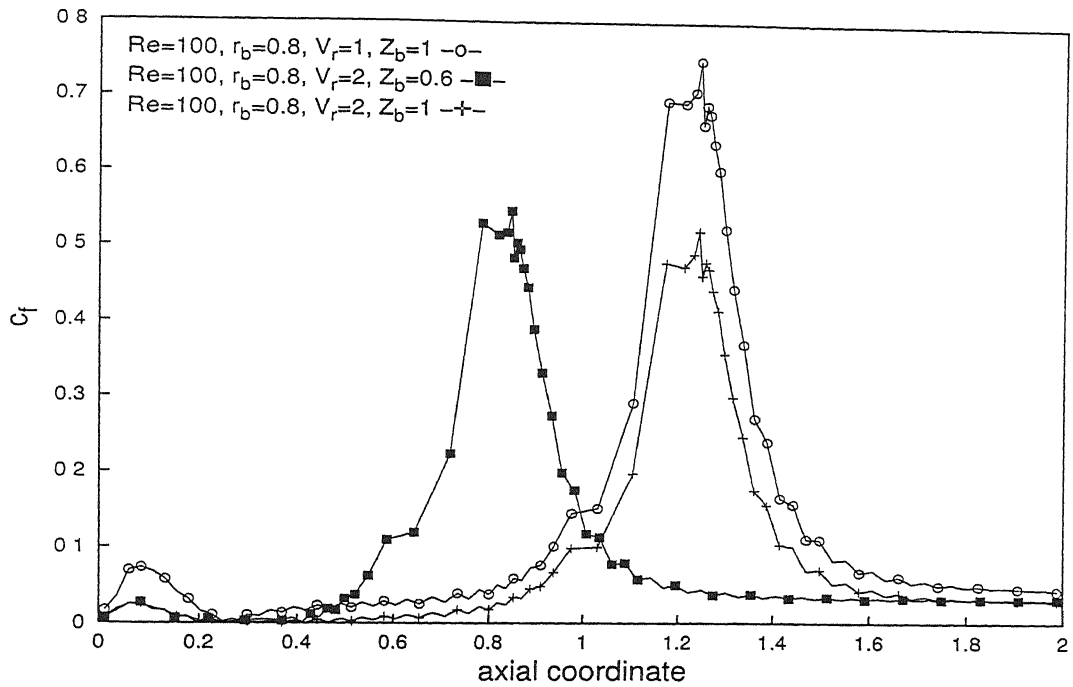


Figure 4.37: Axial variation of skin friction coefficient on the reactor tube wall for the convex substrate geometry;  $\alpha = 30^\circ$ .

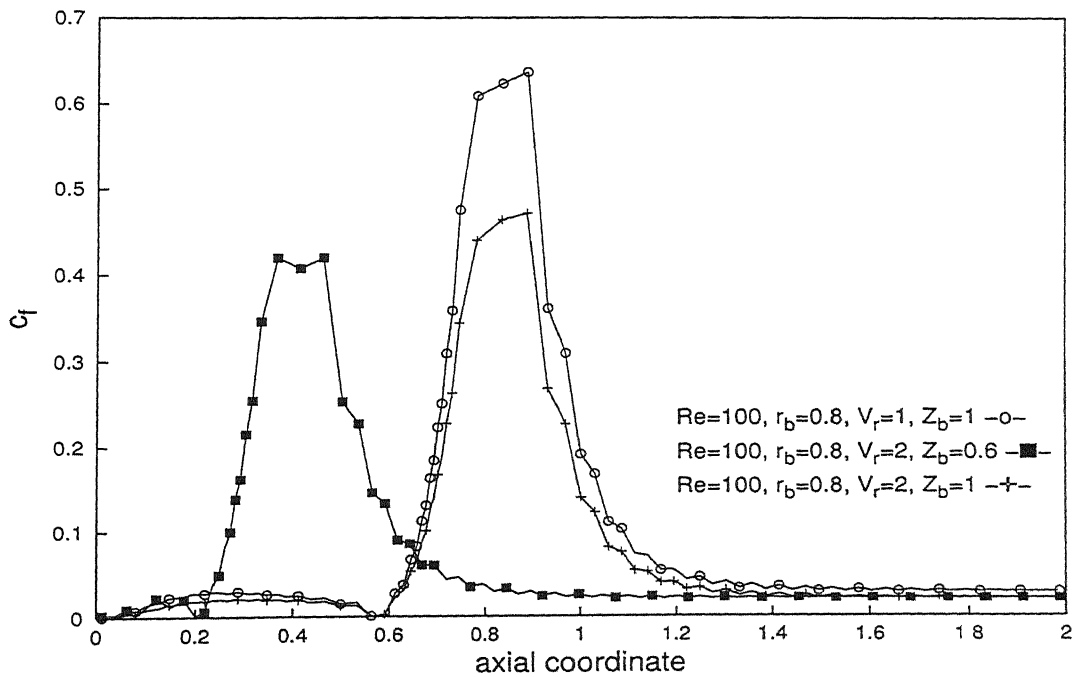


Figure 4.38: Axial variation of skin friction coefficient on the reactor tube wall for the coaxial jets configuration;  $\alpha = 0$ .

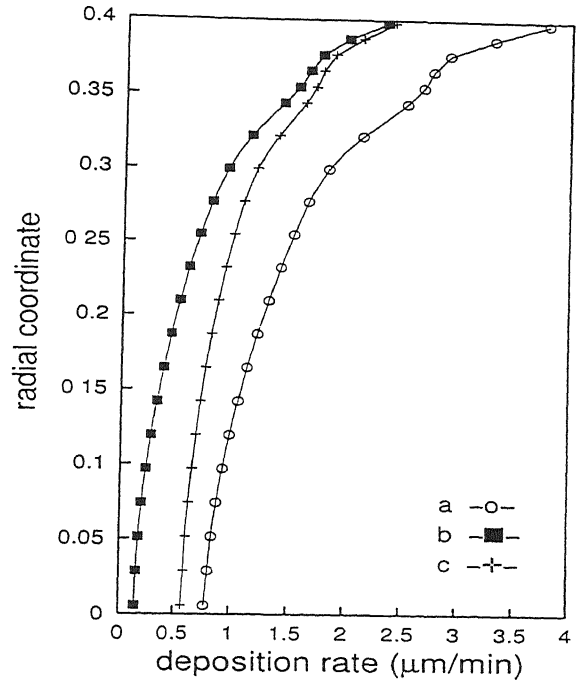
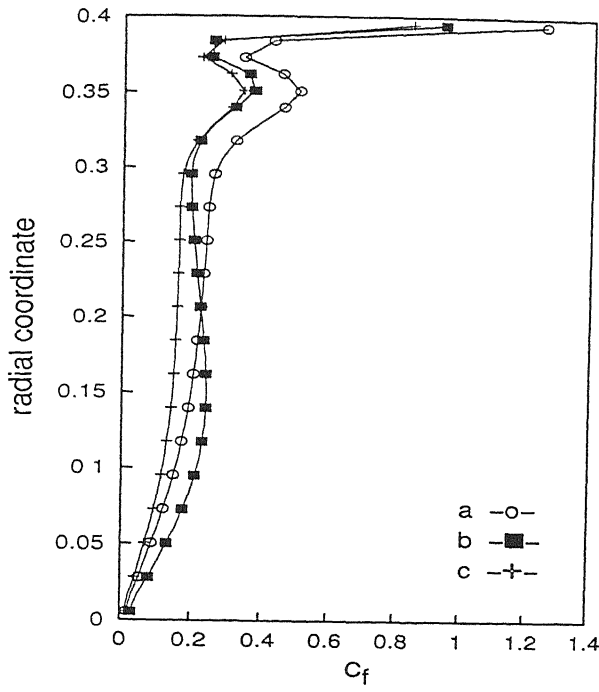


Figure 4.39: Skin friction coefficient and the deposition rate on the substrate surface for the convex substrate geometry with  $Re=100$ ,  $\alpha = 30^\circ$  and  $r_b = 0.8$ ; (a)  $V_r = 1$ ,  $Z_b = 1$ ; (b)  $V_r = 2$ ,  $Z_b = 0.6$ ; (c)  $V_r = 2$ ,  $Z_b = 1$ .

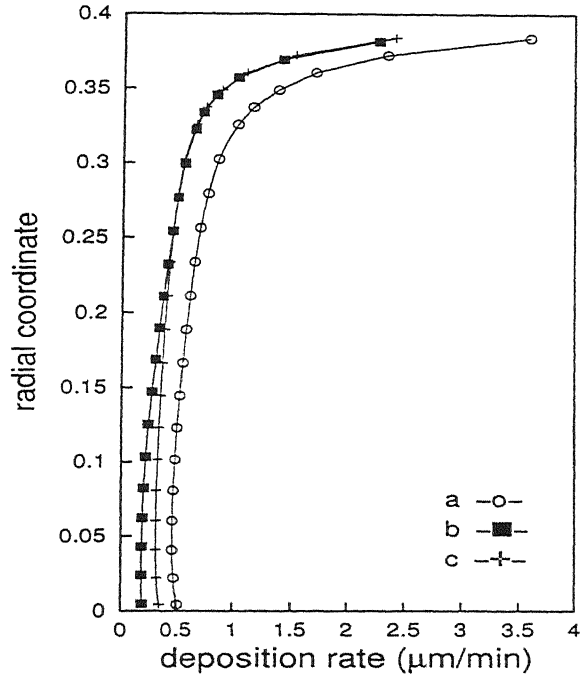
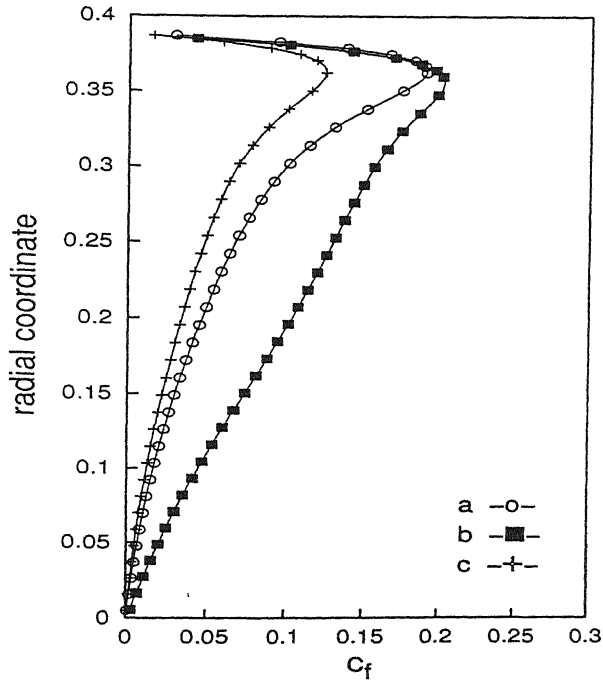


Figure 4.40: Skin friction coefficient and the deposition rate on the substrate surface for the coaxial jets configuration with  $Re=100$ ,  $\alpha = 0$  and  $r_b = 0.8$ ; (a)  $V_r = 1$ ,  $Z_b = 1$ ; (b)  $V_r = 2$ ,  $Z_b = 0.6$ ; (c)  $V_r = 2$ ,  $Z_b = 1$ .

# Chapter 5

## Conclusions and Scope for Future Work

Major conclusions arrived at in the present work are summarized in the present Chapter.

### 5.1 Conclusions

The fluid flow and mass transfer phenomena inside a low pressure CVD reactor have been studied via a mathematical model. Of special interest is the deposition characteristics of zinc sulphide on a passive substrate from zinc and hydrogen sulphide in the gas phase. The results obtained in the present study help judging the merit of a reactor when the geometric configuration and flow parameters are changed. The following conclusions have been arrived at in the present work

1. For a flat substrate placed at right angles to the reactor axis, the flow field mimics the properties of a two-dimensional stagnation flow. Here the streamlines as well as the bulk of the product species bypass the substrate. Hence, the deposition rate on the substrate is uniform but the magnitude of the deposition rate is low.

2. When a concave surface is employed, the stagnation region is further enlarged over which the fluid velocities are small. The bypassing of the concave substrate by the product species continues as in the flat substrate. Once again,

the deposition rate is uniform but is quite small to be of practical value.

3. A convex substrate is better streamlined, and allows the bulk of flow and the reacting species to come close to it. This results in a much smaller stagnation zone. Thus convective flow significantly contributes towards the deposition of zinc sulphide on the substrate in addition to species diffusion. Hence the deposition rate increases considerably over and above what is achieved by concave and flat substrates. The average deposition rate for a convex substrate was computed to be  $1.027 \mu\text{m}/\text{min}$ , compared to  $0.542 \mu\text{m}/\text{min}$  for a concave substrate, an improvement of a factor of two. The degree of uniformity of the deposition was also found to be superior for a convex geometry. Unfavourable edge effects endemic to flat and concave substrates were also mitigated.

4. If the incoming jets are arranged coaxially, the streams of reactants mix and react at their interface. The moving zinc sulphide front reaches the substrate surface in a manner that favours a uniform and a higher deposition rate. The presence of a large recirculatory flow around the jets brings zinc particles closer to the unmixed hydrogen sulphide particles, thus improving the reaction zone. An average deposition rate of  $0.527 \mu\text{m}/\text{min}$  was observed for the coaxial jet arrangement. Benefits seen here are in terms of the uniformity of deposition and a simplification of the technology itself.

## 5.2 Scope for future work

The present research has opened up new possibilities for depositing uniform zinc sulphide layers at a greater speed. These trends should be explored through a full scale simulation. Factors to be examined are:

1. Effect of higher Reynolds numbers.
2. Block position from the inflow plane.
3. Jet inclination

Growth of other infrared sensor material such as zinc selenide ( $\text{ZnSe}$ ) can also be explored using the model developed.

# Appendix A

## Evaluation of species properties

Calculations of the transport properties of the individual gases present in the reactor as a mixture have been presented below. The treatment is valid for diffusion of a particular species in argon, with the presence of other species neglected. This is the approximation of binary diffusion, valid at the limit of the dilute solution. All species are in the gaseous state and assumed to follow the ideal gas law. This approximation may not be strictly valid for zinc sulphide (ZnS) which is formed as a finely dispersed solid phase during the reaction.

### A.1 Binary diffusion coefficients

Values of binary diffusion coefficients at low pressure such as 0.03 atm and high temperature such as 1000 K are not readily available in the published literature. In the present study these coefficients have been calculated by Chapman-Enskog formula that is in turn derived from the kinetic theory of gases Hirschfelder *et al.* (1964) and Bird *et al.* (1960). The formula is given as:

$$\mathcal{D}_{AB} = 1.858 \cdot 10^{-3} \frac{T^{1.5} \left( \frac{1}{M_A} + \frac{1}{M_B} \right)^{0.5}}{P \sigma_{AB}^2 \Omega_{\mathcal{D},AB}}$$

where  $\mathcal{D}_{AB}$  is the diffusion coefficient of species  $A$  in  $B$  in units of  $\text{cm}^2 \text{sec}^{-1}$ ,  $T$  the local temperature is in Kelvin,  $P$  is the bulk pressure in atmospheres,  $\sigma_{AB}$  and  $\Omega_{\mathcal{D},AB}$  are the Lennard-Jones parameters which depend upon temperature and

the inter-molecular potential distribution between the two species. The collision integral  $\Omega_{\mathcal{D},AB}$ , has been tabulated against the values of  $\frac{kT}{\varepsilon}$  for different pairs of gases by Bird *et al.* (1960). The values required to calculate the binary diffusion coefficients between different pairs of gases has been given in Table A.1 for a mean reactor pressure  $P = 0.0296$  atm and a temperature  $T = 917$  K, typically seen at the mid-level of the reactor.

When Lennard-Jones force parameters are not available, they can be calculated from the critical property data Hirschfelder *et al.* (1964) as

$$\sigma = \frac{5}{6} V_c^{\frac{1}{3}} \text{ \AA}, \quad \frac{\varepsilon}{k} = 0.75 T_c \text{ K}$$

Here  $V_c$  and  $T_c$  are the critical volume ( $\frac{\text{cc}}{\text{gm mol}}$ ) and temperature (K) of the species for which these constants are to be calculated. The values of binary diffusion coefficients in the present study have been calculated as:

$$\mathcal{D}_{\text{H}_2\text{S}-\text{A}} = 3.848 \cdot 10^{-3} \text{ m}^2\text{s}^{-1}, \quad \mathcal{D}_{\text{Zn}-\text{A}} = 3.282 \cdot 10^{-3} \text{ m}^2\text{s}^{-1}$$

$$\mathcal{D}_{\text{ZnS}-\text{A}} = 2.457 \cdot 10^{-3} \text{ m}^2\text{s}^{-1}, \quad \mathcal{D}_{\text{H}_2-\text{A}} = 1.753 \cdot 10^{-2} \text{ m}^2\text{s}^{-1}$$

## A.2 Kinematic viscosity

Kinematic viscosity of argon given in Pa s has been calculated from the following temperature polynomial

$$\mu = 22.7 \times 10^{-6} + 7.92 \times 10^{-8} T + 2.93 \times 10^{-11} T^2 - 1.73 \times 10^{-13} T^3 - 1.42 \times 10^{-16} T^4$$

at the mean reactor temperature,  $T = 917$  K.

Table A.1: Leonard Jones force parameters for different species

species	molecular weight	$\sigma(\text{\AA})$	$\frac{\varepsilon}{k}(\text{K})$
A	39.94	3.418	124
H <sub>2</sub> S	34.08	3.733	221.1
Zn	65.38	2.673	2377.5
ZnS	97.38	3	4037.6
H <sub>2</sub>	2.016	2.915	38

# Appendix B

## Validation of Fluid Flow and Mass transfer Codes

### B.1 Fluid Flow

The fluid flow code used in the present study has been validated against the results of Seider and Churchill (1971). These authors have studied the mixing of confined jets in the entrance region of a tubular reactor. The equations for the conservation of momentum and mass were solved numerically. The physical region downstream of the exit of an axial jet mixing with an annular jet of the same fluid was considered. In the investigation uniform temperature and uniform fluid properties were assumed. Two mixed parabolic-elliptic equations for the stream function and vorticity were solved by an implicit finite-difference method. Results were obtained for different jet velocity ratios, jet diameter ratios and Reynolds numbers based on the average velocity at the inlet and the diameter of the reactor. Figures B.1 (b), (c) and (d) show the comparison between the computed results of the present work and those reported by Seider and Churchill (1971). Axial velocity profiles at three sections have been compared. The two sets of results are seen to match very well.

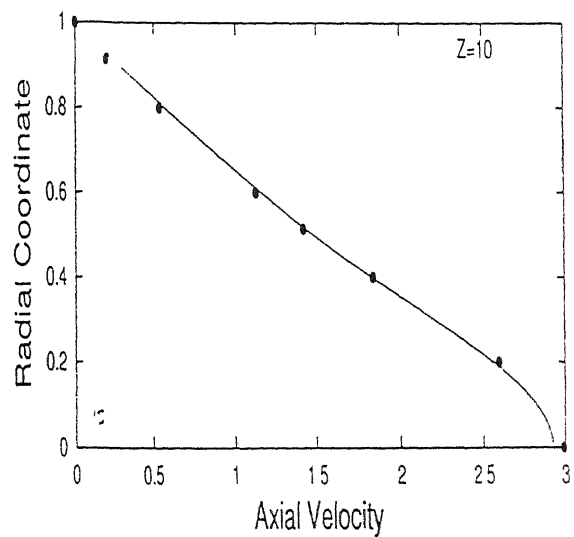
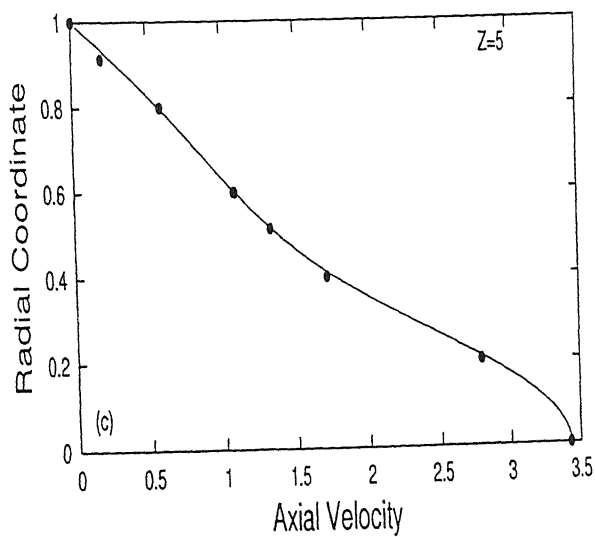
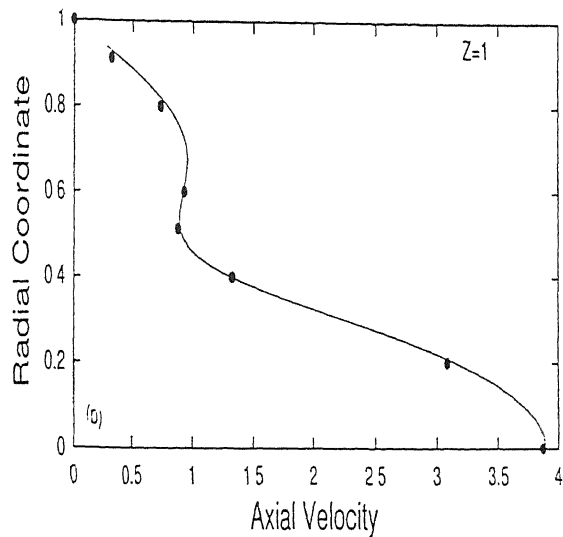
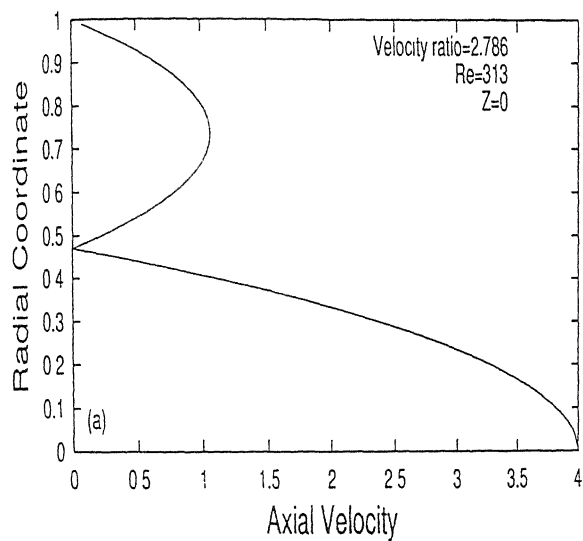


Figure B.1: (a) Inlet velocity profile with only half section of the pipe in shown, (b), (c) and (d) comparison of the computed axial velocity profile (full curve) with Sider and Churchill (1971) (shaded circle) at three axial locations



## B.2 Mass Transfer

Most of the previous numerical and experimental studies on the transport modeling inside a CVD reactor have been directed towards epitaxial growth of silicon with surface reactions. Thus benchmark results for mass transfer are not available. In the present study the mass transfer code has been validated by comparing the results obtained by using the operator splitting algorithm (OS) against the results obtained by solving the full transport equations. Time history for  $\text{H}_2\text{S}$  and  $\text{ZnS}$  mass fraction at three points inside the reactor have been shown. Point 1 is located on the reactor wall at an dimensionless axial distance of 0.6 from the inlet plane. Point 2 is located on the substrate surface at a dimensionless radial distance of 0.15 from the axis of the reactor. Point 3 is in the fluid flow region located at a radial and axial distances of 0.15 and 0.3 respectively, from the inlet plane.

Figures B.2(a-f) show the transient variation of  $\text{H}_2\text{S}$  and  $\text{ZnS}$  at points 1, 2 and 3 respectively. Results for  $\text{H}_2\text{S}$  match exactly at all the points for the two solution strategies. The transients of  $\text{ZnS}$  are slightly different at all the points. It can be seen that discrepancy in the  $\text{ZnS}$  solution from the two approaches occurs at higher times and is a maximum at steady state.

Both the numerical techniques utilize first-order accurate time discretization and so the numerical error incurred are expected to be comparable. Time step were kept equal for the two approaches. As the operator splitting algorithm uses a partial analytical solution it is expected that the associated solutions are more accurate. Hence, results obtained by the OS algorithm alone have been presented in Chapter 4.

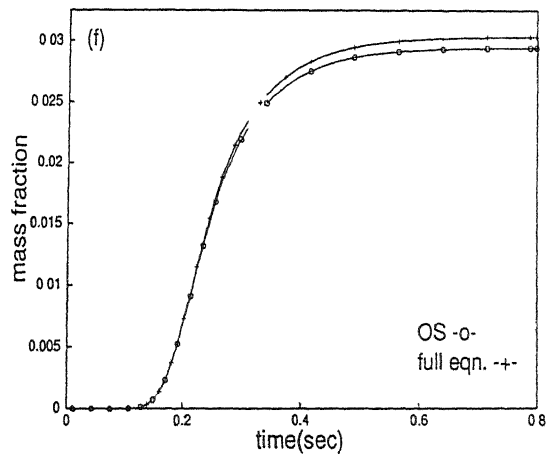
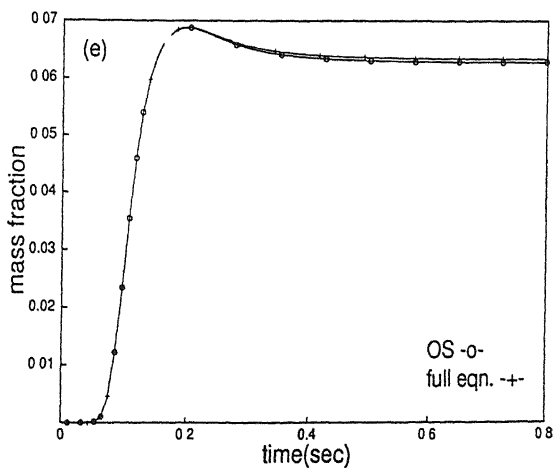
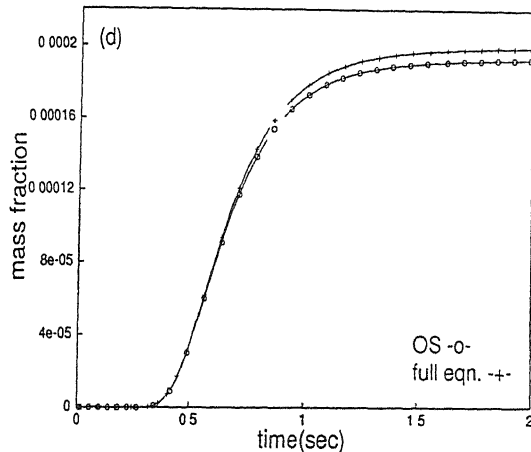
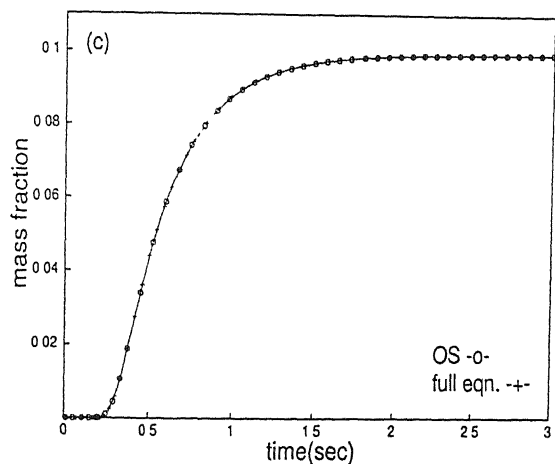
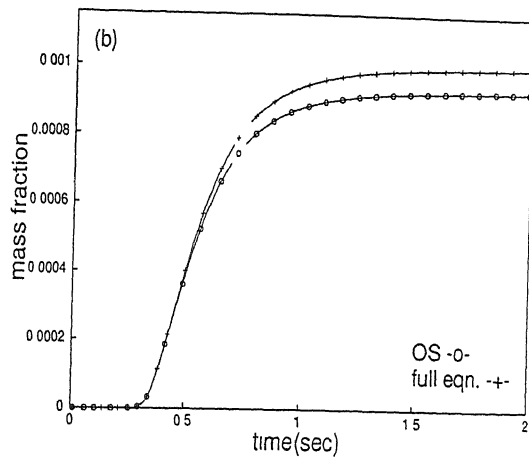
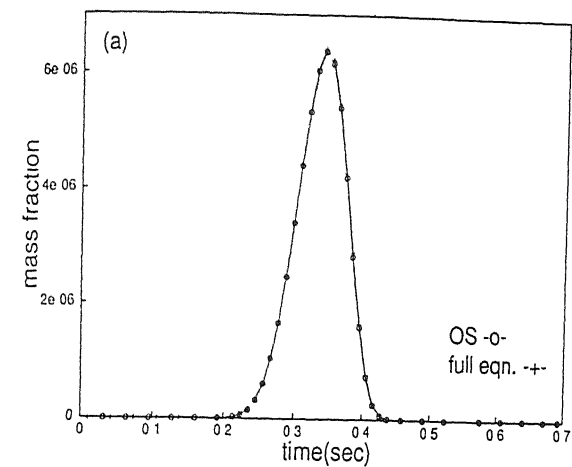


Figure B.2: Transient variation of species; hydrogen sulphide (a) point 1, (c) point 2, (e) point 3; zinc sulphide (b) point 1, (d) point 2, (f) point 3.

# Appendix C

## Derivation of Orthogonal grid generation equation

The equations for generating orthogonal curvilinear coordinates are written in Chapter 3. Derivation of these equations are outlined here.

### C.1 Definition

Definitions of important terms needed in the derivation of the orthogonal mapping equation are presented below Thompson *et al.* (1985).

#### A. Covariant base vectors and Covariant metric tensor

Tangent vectors to the three coordinate lines are the covariant base vectors of the curvilinear system. They are designated by

$$\mathbf{a}_i = \mathbf{r}_{\xi^i} \quad (i = 1, 2, 3) \quad (\text{C.1})$$

The covariant metric tensor finds its origin in the evaluation of an incremental arc length along a spatial curve given by

$$(ds)^2 = \mathbf{a}_i \cdot \mathbf{a}_j d\xi^i d\xi^j = g_{ij} d\xi^i d\xi^j \quad (\text{C.2})$$

The incremental arc length of an arbitrary space curve depends upon the three terms of the dot products  $\mathbf{a}_i \cdot \mathbf{a}_j$  ( $i, j = 1, 2, 3$ ), which forms a symmetric second order tensor. These quantities are the components of the covariant metric tensor, given by

$$g_{ij} = \mathbf{a}_i \cdot \mathbf{a}_j \quad (i, j = 1, 2, 3) \quad (\text{C.3})$$

## B. Contravariant base vectors and contravariant metric tensor

The normal vector to a coordinate surface on which the coordinate  $\xi$  is constant is given by

$$\mathbf{a}^i = \nabla \xi^i \quad (i = 1, 2, 3) \quad (\text{C.4})$$

The three normal vectors to three coordinate surfaces are the three contravariant base vectors of the curvilinear coordinate system. The components of the contravariant metric tensor are the dot products of the contravariant base vectors

$$g^{ij} = \mathbf{a}^i \cdot \mathbf{a}^j \quad (i, j = 1, 2, 3) \quad (\text{C.5})$$

The relation between the contravariant base vectors and covariant base vectors is given by Thompson *et al.* (1985):

$$\mathbf{a}^i = \frac{1}{\sqrt{g}} (\mathbf{a}_j \times \mathbf{a}_k) \quad (i = 1, 2, 3; i, j, k \text{ cyclic}) \quad (\text{C.6})$$

with  $g$  being the Jacobian of the transformation, namely

$$\sqrt{g} = \sqrt{g_{11}g_{22}g_{33}} \quad (\text{C.7})$$

## C. Derivative Operators

Expressions for the derivative operators, such as gradient, divergence, curl and Laplacian are obtained by applying the divergence theorem on a differential volume increment bounded by the coordinate surfaces Thompson *et al.* (1985). The

expression for divergence is given in conservative form as

$$\nabla.A = \frac{1}{\sqrt{g}} \sum_{i=1}^3 [(\mathbf{a}_j \times \mathbf{a}_k).A]_{\xi^i} \quad (i, j, k \text{ cyclic}) \quad (\text{C.8})$$

and in non conservative form,

$$\nabla.A = \frac{1}{\sqrt{g}} \sum_{i=1}^3 [(\mathbf{a}_j \times \mathbf{a}_k).A_{\xi^i}] \quad (i, j, k \text{ cyclic}) \quad (\text{C.9})$$

with  $A$  being a tensor of any order ( $\geq 1$ )

Using the relation (C.1)-(C.9) we can derive the Laplacian operator as :

$$\nabla^2 A = \sum_{i=1}^3 \sum_{j=1}^3 g^{ij} A_{\xi^i, \xi^j} + \sum_{j=1}^3 (\nabla^2 \xi^j) A_{\xi^j} \quad (\text{C.10})$$

## C.2 Elliptic generation system

The simplest elliptic system that satisfies the extremum principle and the smoothness property is the Laplace equation given by

$$\nabla^2 \xi^i = 0 \quad (i = 1, 2, 3) \quad (\text{C.11})$$

Equation (C.11) can be applied to each of the coordinate lines  $\xi^1$ ,  $\xi^2$  and  $\xi^3$  in three dimensions. As the coordinate system in the transformed region are made of contiguous rectangles its easy to treat the curvilinear coordinates ( $\xi^i$ ) as the independent variables and physical coordinates ( $x^i$ ) as the dependent variables in the numerical computation. The transformation of equation (C.11) is obtained using equation (C.10) leading to

$$\nabla^2 \mathbf{r} = \sum_{i=1}^3 \sum_{j=1}^3 g^{ij} \mathbf{r}_{\xi^i, \xi^j} + \sum_{j=1}^3 (\nabla^2 \xi^j) \mathbf{r}_{\xi^j} \quad (\text{C.12})$$

where  $\mathbf{r}$  is the position vector of a point in the physical domain, written as  $\mathbf{r} = (x^1, x^2, x^3)$ . Since  $\nabla^2 \mathbf{r} = 0$  by definition, we get the elliptic generation equation with the help of equation (C.11) as

$$\sum_{i=1}^3 \sum_{j=1}^3 g^{ij} \mathbf{r}_{\xi^i, \xi^j} = 0 \quad (\text{C.13})$$

### C.3 Orthogonal generation system

The characteristic criterion for orthogonality of the body-fitted coordinates is the vanishing of the off-diagonal elements of the covariant and contravariant metric tensor, namely

$$g_{ij} = g^{ij} = 0 \quad \text{for } i \neq j \quad (\text{C.14})$$

For brevity, we write the diagonal elements of the covariant metric tensor as

$$h_i = \sqrt{g_{ii}} \quad (i = 1, 2, 3) \quad (\text{C.15})$$

From equation (C.12) the Laplace equation for grid generation in terms of the physical coordinates as dependent variables is

$$\sum_{i=1}^3 \sum_{j=1}^3 g^{ij} \mathbf{r}_{\xi^i, \xi^j} + \sum_{j=1}^3 (\nabla^2 \xi^j) \mathbf{r}_{\xi^j} = 0 \quad (\text{C.16})$$

On applying orthogonality constraint, equation (C.16) becomes

$$\sum_{i=1}^3 g^{ii} \mathbf{r}_{\xi^i, \xi^i} + \sum_{i=1}^3 (\nabla^2 \xi^i) \mathbf{r}_{\xi^i} = 0 \quad (\text{C.17})$$

The first term of equation (C.17) can be written in terms of covariant metric tensor elements as follows,  $i, j, k$  being cyclic :

$$\begin{aligned}
g^{ii} &= \mathbf{a}^i \cdot \mathbf{a}^i \\
&= \frac{1}{g} [(\mathbf{a}_j \times \mathbf{a}_k) \cdot (\mathbf{a}_j \times \mathbf{a}_k)] \\
&= \frac{1}{g} [(\mathbf{a}_j \cdot \mathbf{a}_j)(\mathbf{a}_k \cdot \mathbf{a}_k) - (\mathbf{a}_j \cdot \mathbf{a}_k)(\mathbf{a}_j \cdot \mathbf{a}_k)] \\
&= \frac{1}{g} [(\mathbf{a}_j \cdot \mathbf{a}_j)(\mathbf{a}_k \cdot \mathbf{a}_k)] \\
&= \frac{1}{g} g_{jj} g_{kk} \\
&= \frac{1}{\sqrt{g}} \frac{g_{jj} g_{kk}}{\sqrt{g_{ii} g_{jj} g_{kk}}} \\
&= \frac{1}{\sqrt{g}} \frac{\sqrt{g_{jj} g_{kk}}}{\sqrt{g_{ii}}} \\
&= \frac{1}{\sqrt{g}} \frac{h_j h_k}{h_i}
\end{aligned}$$

Therefore

$$g^{ii} = \frac{1}{\sqrt{g}} \frac{h_j h_k}{h_i} \quad (i = 1, 2, 3)(i, j, k \text{ cyclic}) \quad (\text{C.18})$$

The second term of equation (C.17) can be shown to be

$$\frac{1}{\sqrt{g}} \left( \frac{h_j h_k}{h_i} \right)_{\xi^i} \mathbf{r}_{\xi^i} \quad (i, j, k \text{ cyclic}) \quad (\text{C.19})$$

Hence equation (C.17) becomes

$$\frac{1}{\sqrt{g}} \sum_{i=1}^3 \left[ \left( \frac{h_j h_k}{h_i} \right)_{\xi^i} \mathbf{r}_{\xi^i} + \left( \frac{h_j h_k}{h_i} \right)_{\xi^i} \mathbf{r}_{\xi^i} \right] = 0 \quad (\text{C.20})$$

Equation (C.20) can be written in compact form as

$$\sum_{i=1}^3 \left( \frac{h_j h_k}{h_i} \right)_{\xi^i} \mathbf{r}_{\xi^i} = 0 \quad (i, j, k \text{ cyclic}) \quad (\text{C.21})$$

Equation (C.21) is the generating equation for orthogonal mapping. The two dimensional form of this equation used in the present work is written as:

$$\frac{\partial}{\partial \xi} \left( f \frac{\partial x}{\partial \xi} \right) + \frac{\partial}{\partial \eta} \left( \frac{1}{f} \frac{\partial x}{\partial \eta} \right) = 0 \quad (\text{C.22})$$

$$\frac{\partial}{\partial \xi} \left( f \frac{\partial y}{\partial \xi} \right) + \frac{\partial}{\partial \eta} \left( \frac{1}{f} \frac{\partial y}{\partial \eta} \right) = 0 \quad (\text{C.23})$$

where  $f$  is the distortion function given by

$$f = \frac{\sqrt{g_{22}g_{33}}}{\sqrt{g_{11}}} = \frac{\sqrt{x_\eta^2 + y_\eta^2}}{\sqrt{x_\xi^2 + y_\xi^2}} \quad (\text{C.24})$$

with  $g_{33} = 1$  for two dimensional geometries.



# Bibliography

- [1] A. W. Date, Complete pressure correction algorithm for solution of a incompressible Navier-stokes equations on a non-staggered grid, Numerical Heat Transfer, Part B, Vol. 29, pp. 441-458 (1996).
- [2] C. E. Morosanu, Thin Films by Chemical Vapor Deposition, Elsevier, 1990.
- [3] C. H. Cooke, On Operator Splitting for unsteady Boundary Value Problems, J. Comput. Phys., Vol. 67, pp. 472-478 (1986).
- [4] C. M. Rhie and W. L. Chow, Numerical study of turbulent flow past an aerofoil trailing separation, AIAA Journal, Vol. 21, pp. 1325-1332 (1983).
- [5] C. R. Klejin, Th. H. van der Meer, and C. J. Hoogendoorn, A Mathematical Model for LPCVD in a Single wafer Reactor, J. Electrochem. Soc., Vol. 136, No. 11, pp. 3423-3433 (1989).
- [6] D. Ding, P. L. F. liu, An Operator-Splitting Algorithm for Two-dimensional Convection-Dispersion-Reaction Problems, Int. J. for Numer. Meth. Engg., Vol. 28, pp. 1023-1040 (1989).
- [7] E. D. Chikhliwala and Y. C. Yortsos, Application of Orthogonal Mapping to some Two-Dimensional Domains, Comput. Phys. , Vol. 57, pp. 391-402 (1985)
- [8] Erwin Kreyszig, Advanced Engineering Mathematics, John Wiley, 1993.
- [9] G. Shavit and Z. Lavan, Analytical and Experimental Investigations of Laminar Mixing of Confined Heterogeneous Jets, AIAA Journal, Vol. 11, No. 3, pp. 352-358 (1972).

- [10] G. Ryskin and L. G. Leal, Orthogonal Mapping, J. Comput. Phys. , Vol. 50, pp. 71-100 (1983).
- [11] H. K. Moffat and K. F. Jensen, Three-Dimensional Flow Effects in Silicon CVD in Horizontal Reactors, J. Electrochem. Soc., Vol. 135, No. 2, pp.459-471 (1988).
- [12] I. H. Oh, C. G. Takoudis and G. W. Neudeck, Mathematical Modeling of Epitaxial Silicon Growth in Pancake Chemical Vapor Deposition Reactor, J. Electrochem. Soc., Vol. 138, No. 2, pp. 554-567 (1991).
- [13] J. C. Tannehill, D. A. Anderson and R. H. Pletcher, Computational Fluid Mechanics and Heat Transfer, Taylor & Francis, 1997.
- [14] Joe F. Thompson, Z. U. A. Warsi, C. Wayne Mastin, Numerical Grid Generation, North-Holland, 1985.
- [15] J. O. Hirschfelder, C. F. Curtiss and R. B. Bird, Molecular Theory of Gases and Liquids, John Wiley, 1964.
- [16] K. Muralidhar and T. Sundararajan, Computational Fluid Flow and Heat Transfer, Narosa, 1995.
- [17] K. Muralidhar, M. Verghese and K. M. Pillai, Application of an Operator Splitting Algorithm for Advection-Diffusion Problems, Numerical Heat Transfer, Part A, Vol. 23, pp. 99-114 (1993).
- [18] K. N. Ghia, T. P. Torda and Z. Lavan, Laminar Mixing of Heterogeneous Axisymmetric Coaxial Confined Jets, Vol. 7, No. 11, pp. 2072-2078 (1969).
- [19] Luis Eca, 2D Orthogonal Grid Generation With Boundary Point Distribution Control, J. Comput. Phys. , Vol. 125, pp. 440-453 (1996).
- [20] M. C. Melaaen, Non-staggered calculation of laminar and turbulent flows using curvilinear nonorthogonal coordinates, Numerical Heat Transfer, Part A, Vol. 24, pp. 375-392 (1993).
- [21] M. L. Hitchman and K. F. Jensen, Chemical Vapor Deposition, Academic Press, 1993.

- [22] M. T. Nair and T. K. Sengupta, Orthogonal Grid Generation For Navier-Stokes Computations, *Int. J. for Numer. Meth. Fluids*, Vol. 28, pp. 215-224 (1998).
- [23] O. Levenspiel, *Chemical Reaction Engineering*, John Wiley, 1999.
- [24] Papageorgakopoulos, G. Arampatzis, D. Assimacopoulos and N. C. Markatos, Enhancement of the momentum interpolation method on non-staggered grids, *Int. J. for Numer. Meth. Fluids*, Vol. 33, pp. 1-22 (2000).
- [25] P. Duverneuil and J. P. Couderc, Two-Dimensional Modeling of LPCVD Hot Wall Reactors, *J. Electrochem. Soc.*, Vol. 139, No. 1, pp. 296-304, (1992).
- [26] R. Byron Bird, Warren E. Stewart and Edwin N. Lightfoot, *Transport Phenomena*, John Wiley, 1960.
- [27] R. Duraiswami, A. Prosperetti, Orthogonal Mapping in Two Dimensions, *J. Comput. Phys.* , Vol. 98, pp. 254-268 (1992).
- [28] Robert E. Treybal, *Mass-Transfer Operations*, McGRAW-HILL, ()
- [29] Roop L. Mahajan, *Transport Phenomena in Chemical Vapor-Deposition Systems*, *Advances in Heat Transfer*, Vol. 28, pp. 339-415 (1996).
- [30] Satya Prakash, V. Eswaran, G. Biswas, K. Muralidhar, S. G. Dhande, Numerical Simulation of Unsteady Three-Dimensional Flow Around an Elongated Body Moving in an Incompressible Fluid Using a Parallel Computer. Technical Report, DRDL Report, Hyderabad, July 1996.
- [31] S. B. Beale, A Finite Volume Method For Numerical Grid Generation, *Int. J. for Numer. Meth. Fluids*, Vol. 30, pp. 523-540 (1999).
- [32] S. K. Choi, H. Y. Nam and M. Cho, Use of the momentum interpolation method for numerical solution of incompressible flows in complex geometries: choosing cell face velocities, *Numerical Heat Transfer, Part B*, Vol. 23, pp. 21-41 (1993).

- [33] S. Majumdar, Role of under-relaxation in momentum interpolation for calculation of flow with non-staggered grids, Numerical Heat Transfer, Part B, Vol. 13, pp. 125-132 (1988).
- [34] S. V. Patankar, Numerical Heat transfer and fluid flow, Hemisphere, New York, 1980.
- [35] T. F. Miller and F. W. Schmidt, Use of a pressure-weighted interpolation method for the solution of the incompressible Navier-Stokes equations on a non-staggered grid systems, Numerical Heat Transfer, Part B, Vol. 14, pp. 213-233 (1988).
- [36] Thomas K. Sherwood, Robert L. Pigford and Charles R. Wilke, Mass Transfer, McGRAW-HILL kogakusha, 1952.
- [37] W. D. Seider and S. W. Churchill, Confined Jet Mixing in the Entrance of a Tubular Reactor, AIChE Journal, Vol. 17, No. 3, pp. 704-712 (1971).
- [38] W. Kordulla and M. Vinokur, Efficient Computation of Volume in Flow Predictions, AIAA Journal, VOL. 21, pp. 917-918, (1983).
- [39] Y. N. Jeng and C. T. Chen, Two-Dimensional Orthogonal Grid Generation With Floating Boundary Points, Numerical Heat Transfer, Part B, Vol. 36, pp. 207-232 (1999).

A

141937



A141937